NOVA-2 - A Digital Computer Program for Analyzing Nuclear Overpressure Effects on Aircraft. Part 1. Theory

Kaman AviDyne

August 1976

AFWL-TR-75-262, Pt. 1

AFWL-TR-
75-262
Pt. I

NOVA-2 — A DIGITAL COMPUTER PROGRAM FOR ANALYZING NUCLEAR OVERPRESSURE EFFECTS ON AIRCRAFT

Part 1

Theory

Kaman AviDyne
Burlington, MA 01803

August 1976

Final Report

AIR FORCE WEAPONS LABORATORY
Air Force Systems Command
Kirtland Air Force Base, NM 87117

This final report was prepared by Kaman AviDyne, Burlington, Massachusetts, under Contract F29601-75-C-0032, Job Order 88090339, with the Air Force Weapons Laboratory, Kirtland Air Force Base, New Mexico. Mr. Gerald M. Campbell (SAT) was the Laboratory Project Officer-in-Charge.

When US Government drawings, specifications, or other data are used for any purpose other than a definitely related Government procurement operation, the Government thereby incurs no responsibility nor any obligation whatsoever, and the fact that the Government may have formulated, furnished, or in any way supplied the said drawings, specifications, or other data, is not to be regarded by implication or otherwise, as in any manner licensing the holder or any other person or corporation, or conveying any rights or permission to manufacture, use, or sell any patented invention that may in any way be related thereto.

This report has been reviewed by the Information Office (OI) and is releasable to the National Technical Information Service (NTIS). At NTIS, it will be available to the general public, including foreign nations.

This technical report has been reviewed and is approved for publication.

Gerald M. Campbell

GERALD M. CAMPBELL
Project Officer

FOR THE COMMANDER

Terry N. Lauritsen

TERRY N. LAURITSEN
Lt Colonel, USAF
Chief, Technology and Analysis Branch

Paul J. Daily

PAUL J. DAILY
Colonel, USAF
Chief, Analysis Division

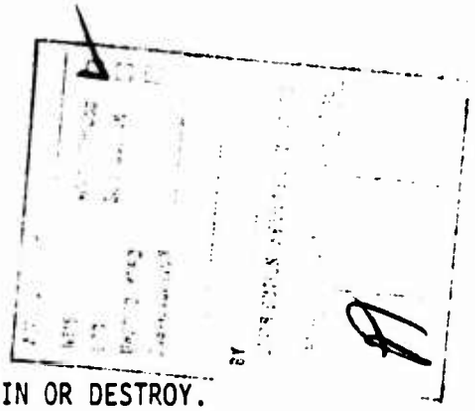

DO NOT RETURN THIS COPY. RETAIN OR DESTROY.

UNCLASSIFIED

SECURITY CLASSIFICATION OF THIS PAGE (When Data Entered)

REPORT DOCUMENTATION PAGE		READ INSTRUCTIONS BEFORE COMPLETING FORM
1. REPORT NUMBER AFWL-TR-75-262, Pt. 1	2. GOVT ACCESSION NO.	3. RECIPIENT'S CATALOG NUMBER
4. TITLE (and Subtitle) NOVA-2 -- A DIGITAL COMPUTER PROGRAM FOR ANALYZING NUCLEAR OVERPRESSURE EFFECTS ON AIRCRAFT, Part 1, Theory		5. TYPE OF REPORT & PERIOD COVERED Final Report 6. PERFORMING ORG. REPORT NUMBER KA TR-128
7. AUTHOR(s) William N. Lee Lawrence J. Mente		8. CONTRACT OR GRANT NUMBER(s) F29601-75-C-0032
9. PERFORMING ORGANIZATION NAME AND ADDRESS Kaman AviDyne A Division of Kaman Sciences Corporation Burlington, MA 01803		10. PROGRAM ELEMENT, PROJECT, TASK AREA & WORK UNIT NUMBERS 62601F 88090339
11. CONTROLLING OFFICE NAME AND ADDRESS Air Force Weapons Laboratory (SAT) Kirtland Air Force Base, NM 87117		12. REPORT DATE August 1976 13. NUMBER OF PAGES 212
14. MONITORING AGENCY NAME & ADDRESS(if different from Controlling Office)		15. SECURITY CLASS. (of this report) UNCLASSIFIED 15a. DECLASSIFICATION/DOWNGRADING SCHEDULE

16. DISTRIBUTION STATEMENT (of this Report)

Approved for public release; distribution unlimited.

17. DISTRIBUTION STATEMENT (of the abstract entered in Block 20, if different from Report)

18. SUPPLEMENTARY NOTES

This report consists of two parts. Part 1, Theory, includes the front matter, sections I through V, pages 1 to 196. Part 2, Computer Program, includes Section VI and the references, pages 197 to 348.

19. KEY WORDS (Continue on reverse side if necessary and identify by block number)

Aircraft aerodynamic loading
Aircraft vulnerability
Digital computer program
Elastic-plastic material behavior
Ground reflection effect
Nuclear blast
Overpressure effects
Structural response of beam and panel elements

20. ABSTRACT (Continue on reverse side if necessary and identify by block number)

NOVA-2 (Nuclear Overpressure Vulnerability Analysis, Version 2) is an updated version of NOVA, a FORTRAN-IV digital computer program for calculating the response of individual structural elements of aircraft, such as stringers, frames and panels, exposed to the transient pressure loading associated with the blast wave from a nuclear explosion. The updated version extends the capability of NOVA to analyze rib elements, frames with variable cross section, and offers a choice of clamped, simply supported or free edge boundary (over)

DD FORM 1 JAN 73 1473 EDITION OF 1 NOV 65 IS OBSOLETE

UNCLASSIFIED

SECURITY CLASSIFICATION OF THIS PAGE (When Data Entered)

ABSTRACT (cont'd)

conditions. For inelastic structural response, a much improved elastic-plastic model for material behavior is provided. Also added to NOVA is the REFRA near-ground reflections model for blast waves. The program still provides the overall capability to analyze multilayered beam and panel elements exposed to a steady-state subsonic or supersonic aerodynamic preload, followed by a dynamic blast wave. A critical slant range is automatically determined in an iteration where damage criteria (specified on a probabilistic basis) are compared with the structural response.

PREFACE

This report represents continuation of work performed by Kaman AviDyne, Burlington, Massachusetts, and previously documented in AFWL-TR-72-115, Volume 1. The current report contains a complete description of new extensions and modifications of NOVA and also retains applicable sections from the previous volume.

Mr. William N. Lee and Mr. Lawrence J. Mente were principal investigators and project leaders for the current effort. Other technical contributors for the current effort were as follows: Dr. Norman P. Hobbs, Mr. Garabed Zartarian; Mr. John H. Thompson; and Mr. Michael Tomayko. This work was performed under the Structural Mechanics Group of Kaman AviDyne headed by Mr. Emanuel S. Criscione.

The contractor's report number is KA TR-128.

CONTENTS

CONTENTS (Continued)

CONTENTS (Concluded)

ILLUSTRATIONS

ILLUSTRATIONS (Continued)

ILLUSTRATIONS (Continued)

ILLUSTRATIONS (Continued)

ILLUSTRATIONS (Concluded)

TABLES

TABLES (Concluded)

SECTION I
INTRODUCTION

NOVA-2 (Nuclear Overpressure Vulnerability Analysis, Version 2) is a digital computer program representing a complex analysis of aircraft structural elements subjected to nuclear overpressure effects. This version contains extensive modifications of NOVA (ref. 1, now also referred to as NOVA-1) with expanded analytical capabilities, improved accuracy, and more efficient computer utilization. This document presents a complete description of the analytical methods used and of the computer program, including guidelines for running the program and example problems.

The NOVA-2 program provides a technique for predicting the elastic and inelastic response of aircraft structural elements to the transient pressure loads associated with the blast wave from a nuclear explosion. These high intensity pressure loads are treated separately from the gust loads due to the blast wave and are associated with the initial reflected pressure which occurs during diffraction of the blast wave around the structure. Because the pressures exist for such a short time, they excite high frequency, secondary structure such as skin panels, stringers, longerons, frames, ribs, canopies and radomes. The gust, or post diffraction, loads tend to excite low frequency, primary structural surfaces such as the wings, fuselage, and horizontal and vertical tails. Therefore, the separation between pressure (often referred to as overpressure) and gust effects on aircraft structure is generally based on secondary high frequency structure and primary low frequency structure.

The program determines the slant range between the aircraft and point of burst for specified levels of structural damage as a function of structural element; weapon yield, orientation and height of burst; aircraft speed and altitude; and degree of probability that the level of damage is incurred or exceeded. Likewise, it determines the response of structural elements for a specified slant range.

A single element dynamic analysis technique, which considers both linear elastic and inelastic deformations and assumes that the element does not interact with adjacent elements, reduces the complexity of the modeling and analysis, and thus provides a solution more rapidly than a finite element analysis. The errors introduced by considering isolated structural elements rather than multi elements appear to be reasonable for most components when compared with those introduced by other uncertainties associated with the analysis. However, for structures with rapidly changing cross section, such as a nose radome, the errors may be unacceptable.

The program uses a quasi-strip method for predicting the pressure loading on the lifting surfaces of the aircraft prior to the arrival of the blast wave. The pressure induced by the thickness of the airfoil is neglected and the pressure loading is assumed to be a function of and directly proportional to the angle of attack. The pressure loadings induced on the wing and tail surfaces by the blast wave are predicted using linear acoustic theory and the assumption that the airfoil sections can be represented by their mean-camber lines.

The program predicts, prior to and during diffraction of the blast wave, the pressure loading on the surface of the fuselage by relating the fuselage to an equivalent body of revolution with the same distribution of cross-sectional area along its length and by applying the reflection theory for the interaction of a shock wave with a flat surface.

A 1-KT nuclear standard, based on data obtained from the AFWL SPUTTER and SAP fluid dynamics programs, provides the time-dependent free-air blast characteristics for the BLAST routines. For near-ground bursts where the blast wave strikes the ground and is reflected, two models are now optional in NOVA-2: 1) an empirical model, which describes the wave forms associated with regular reflection and the transition to Mach reflection, and 2) a comprehensive data tape, based on the REFLECT code, which provides a time history of the ground-reflected blast characteristics.

The program consists of three distinct routines, NOVA, DEPROB (Dynamic Elastic Plastic Response of Beams), and DEPROP (Dynamic Elastic Plastic Response of Panels), written in FORTRAN IV.

The NOVA routine is the master routine which controls the logic of the overall program. It contains the subroutines for predicting the aerodynamic flight loads and the blast pressure loads that are applied to the lifting surfaces and fuselage during subsonic and supersonic flight, and for determining the slant range at which a structural element incurs damage which has been specified on a probabilistic basis.

The DEPROB routine provides the response of aircraft structure such as stringers, longerons, frames, ribs, and conical or cylindrical radomes which can be represented by an annular cross section. The method of analysis used in this routine applies to beams which can be modeled in one dimension by a series of discrete masses interconnected by weightless bars. Major additions to DEPROB in NOVA-2 are the ability to analyze elements with variable cross section, the addition of simply supported and free edge conditions, an improved elastic-plastic stress-strain model, and the inclusion of rib buckling as a failure mechanism.

The DEPROP routine provides the response of aircraft skin panels, canopies, and radomes that can be approximated by a cylindrical panel. The linear elastic option applies to single and multilayered panels of isotropic or orthotropic material, and the elastic-plastic option applies to single layer panels of isotropic material. DEPROP has been modified to include the following: symmetric or nonsymmetric combinations of clamped or simply supported edge constraints, a much improved elastic-plastic stress-strain model, and improved overall accuracy.

The NOVA-2 program as a whole represents a much more efficient code than NOVA-1, requiring less computer core and time. This is accomplished by making more extensive use of overlaying techniques and through improved computational techniques.

SECTION II
BLAST MODELS

In order to simulate the overpressure effects of a blast wave emanating from a nuclear explosion, NOVA-2 provides the analyst with a choice of ground reflection models when ground reflection is important. A one-dimensional free-air blast model is the basis of both models, and is used when ground reflection is not important. One ground reflection model is a semiempirical functional curve fit (that used in NOVA-1); the second is a two-dimensional data tape generated by a hydrodynamic computer code. These two models are described in subsections 2.1 and 2.2, respectively.

The free-air blast model in NOVA-2 is the most recent AFWL 1-KT curve fit model available (refs. 2 and 3), which is based on the AFWL 1-KT nuclear standard data tape (ref. 4). Figure 1 compares overpressure versus range for both free-air models. For historical completeness, the IBM Problem-M curve contained in reference 5 is also shown. By coincidence this curve nearly coincides with that of the current curve fit model, and the differences are indistinguishable in figure 1.

2.1 ANALYTICAL GROUND-REFLECTED BLAST MODEL

The first ground-reflected blast model is a semiempirical, two-dimensional model, identical in form to that used in NOVA-1. The only differences are minor changes in curve fit coefficients. The basic mathematical model is documented in reference 6.

2.2 REFRA GROUND-REFLECTED BLAST MODEL

The second ground reflected blast model available in NOVA-2 is in the form of a two-dimensional blast tape (logical file TAPE10), read and interpreted by the REFRA routine (ref. 7). The original data base is generated by the REFLECT code (ref. 8) and subsequently processed for more efficient use by REFRA.

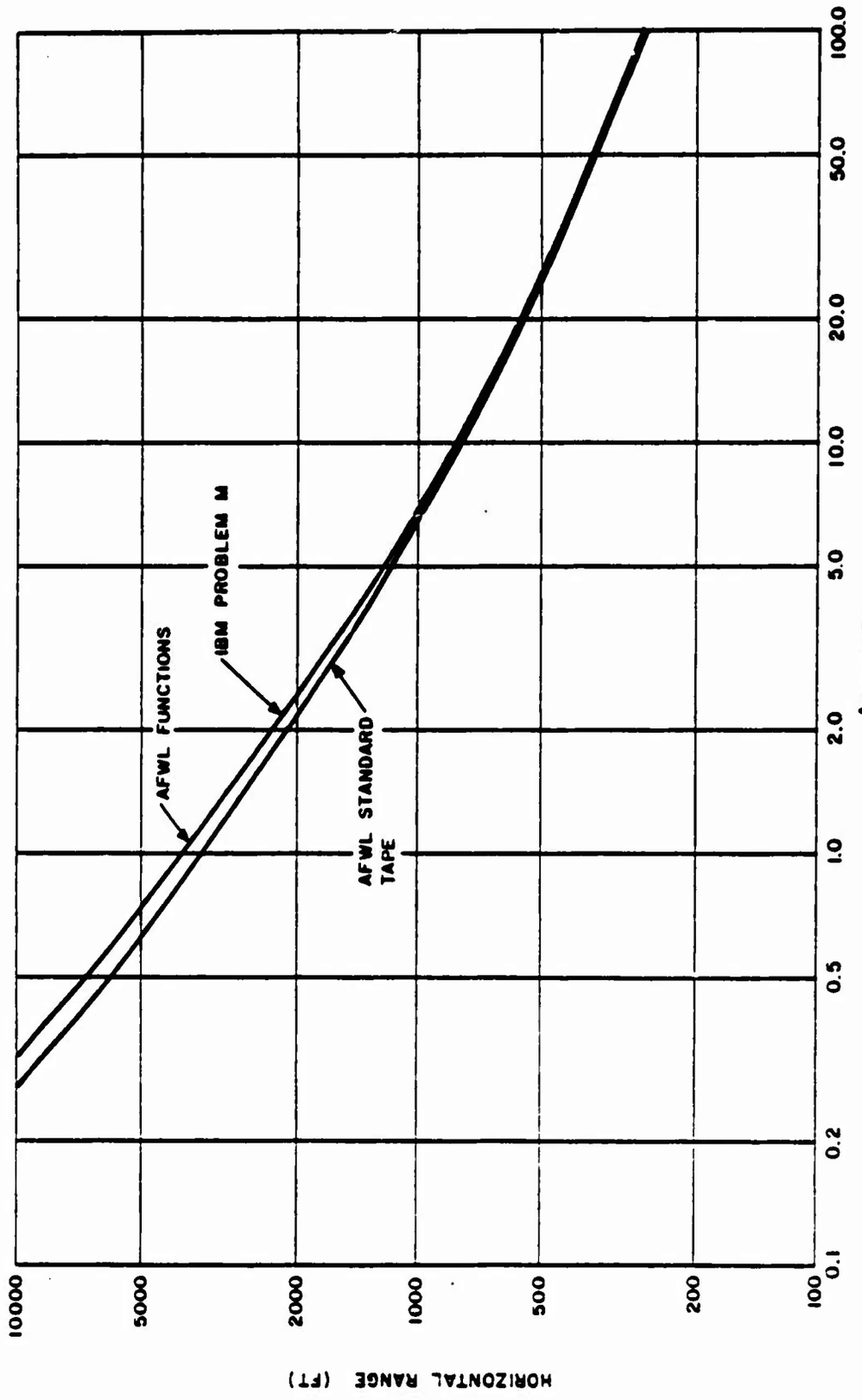

Figure 1 - Overpressure vs. Distance for 1-KT Explosion at Sea Level

Only data pertaining to region III of figure 2 are provided on tape, as the undisturbed region, region I, merely represents ambient conditions, and data for region II are provided by the free-air model. A moving mesh model in the REFLECT code provides data behind the shock fronts which are precisely defined and free of the complications associated with various artificial smoothing processes. The REFRA routine searches the data tape to determine which region is appropriate and returns the corresponding blast data. It should be readily apparent that because the data tape is limited to regions behind the Mach and reflected shocks, great savings in tape length and computer search time are realized. Accordingly, a very comprehensive time history of the reflected wave, and the region behind it, is made available on tape.

Each REFLECT run, and hence each corresponding data tape, is characterized by a unique scaled height of burst (above ground level), scaled to 1-KT at sea level. To select the appropriate tape for the problem of interest, figure 3 shows the relationship of relevant geometrical parameters.

Once the ground altitude (H_g), the aircraft altitude (H) and the vertical separation between the aircraft and the burst (z) are selected, the height of burst is uniquely specified (HOB = $H - H_g - z$). The scaled height of burst (SHOB) is then determined from the following relationship, making use of modified Sachs scaling:

$$SHOB = \left[\frac{p_a/p_o}{W}\right]^{1/3} HOB$$

where W is the yield in kilotons, p_a is the ambient pressure at the aircraft altitude, and p_o is the ambient pressure at sea level, taken to be 14.696 psi.

It can be seen that the altitude of the aircraft relative to the burst must remain constant for problems using a single data tape. Hence, when the program iterates to find a critical slant range, the iteration is restricted to constant aircraft and burst altitudes for

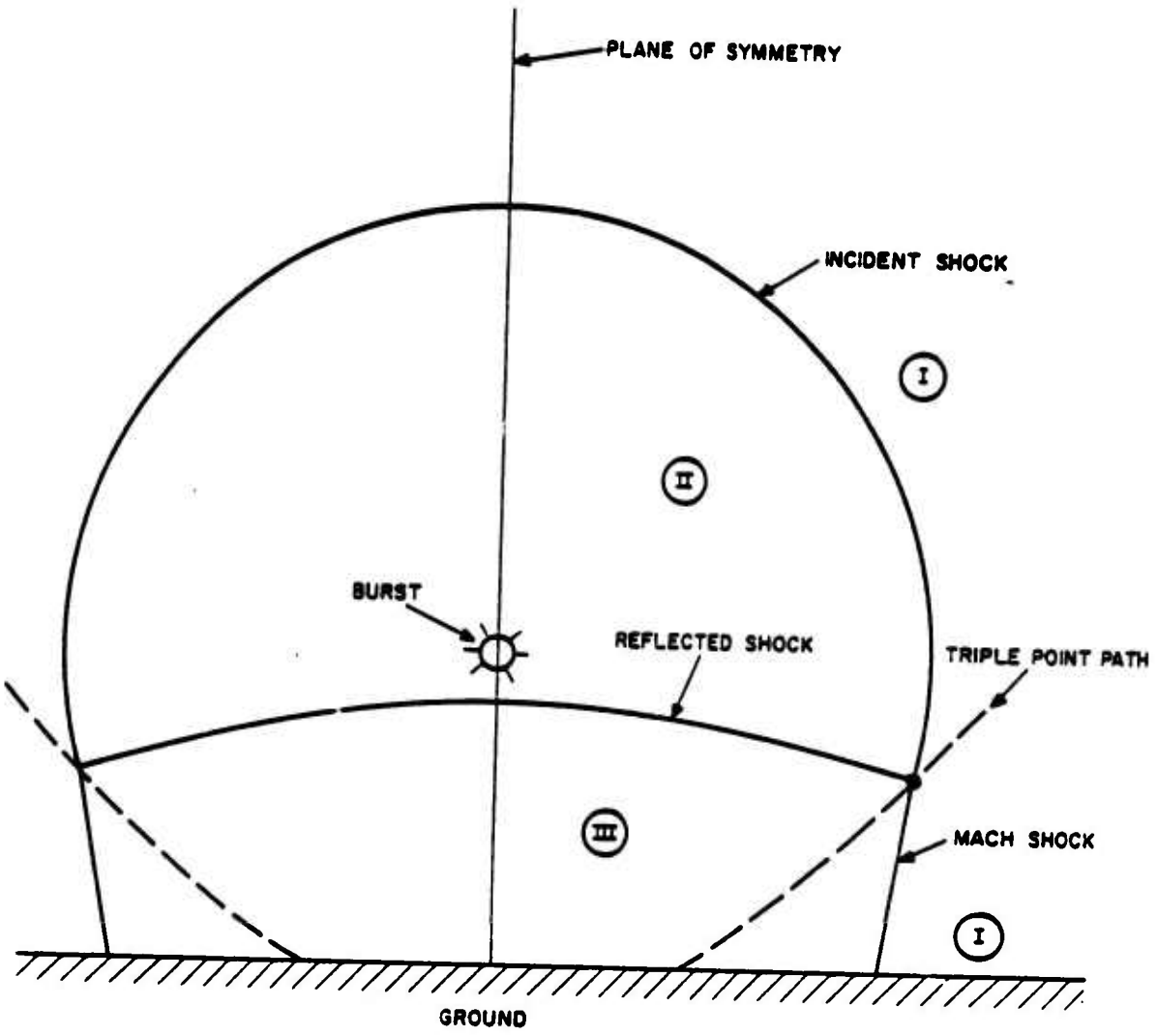

Figure 2. Geometry of Blast Field Involving Ground Reflection

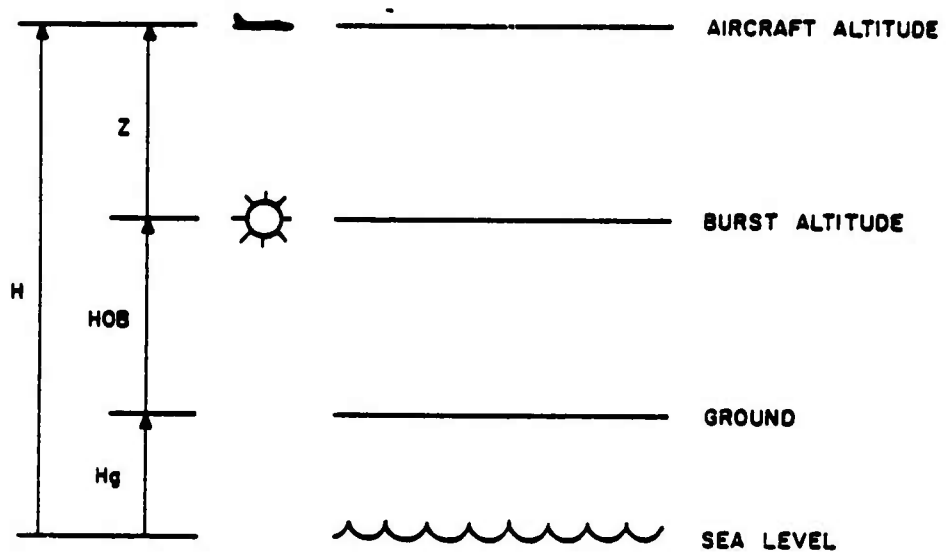

Figure 3. Geometrical Relationship of Aircraft, Burst Center, and Ground

this ground reflection model, whereas the method described in subsection 2.1 does not have this limitation since the empirical model will handle any height of burst. The REFRA model will, in general, also take slightly more computer time for problems involving ground reflection. It should be noted, however, that the REFRA model offers a much more sophisticated, complete description of the phenomena of ground reflection.

SECTION III
PREBLAST AND BLAST-INDUCED LOADING

3.1 LOADING ON LIFTING SURFACES

The pressure loading at a point on a lifting surface of an aircraft engulfed by a blast field may be approximated in terms of two pressure distributions; the first associated with the flow prior to blast arrival and the second induced by the blast wave. The form used is as follows:

$$p_\ell - p_u = (\Delta C_p w_{ss} + \Delta c_p w_g) \frac{1}{2} \rho V_r \qquad (1)$$

where

- p_ℓ and p_u are the pressures at a point on the lower and upper surfaces, respectively
- ΔC_p and Δc_p are the steady-state and transient pressure coefficients, respectively, at the point on the lifting surface
- w_{ss} and w_g are the steady-state and blast-induced flow velocities normal to the lifting surface, respectively, at the point on the surface
- ρ is the instantaneous density at the point on the surface
- V_r is the resultant velocity of the steady-state flow plus the blast-induced flow at the point on the surface

The procedures by which ΔC_p and Δc_p are calculated for lifting surfaces in the analysis are presented in the remainder of this subsection.

The pressure increase on the lower surface, $p_\ell - p_\infty$, is taken equal in magnitude and opposite in sign to the pressure decrease on the upper surface, $p_u - p_\infty$, where p_∞ is the pressure at the point in the absence of the lifting surface.

$$p_\ell = p_\infty + \frac{1}{2}(p_\ell - p_u) \tag{2}$$

$$p_u = p_\infty - \frac{1}{2}(p_\ell - p_u) \tag{3}$$

Since p_ℓ and p_u cannot physically achieve negative values, these quantities are set equal to zero within the computer analysis whenever either becomes negative according to equation (2) or equation (3); however, the correct value of $p_\ell - p_u$, as given by equation (1), is retained in the analysis.

3.1.1 Preblast Loading

This section provides formulations for predicting the pressure loading coefficient ΔC_p on lifting surfaces before exposure to blast environment. Although more elaborate techniques are available, i.e., surface methods, the emphasis here is on practical and simplified techniques which are more appropriate for a vulnerability code. The formulations presented here are for subsonic, transonic, and "low to medium" supersonic flight ranges and consider typical classes of wing or tail planforms during a symmetric flight maneuver. The derived equations form the basis for the program in the vulnerability code.

A rigorous approach cannot be offered for calculating the pressure coefficient at arbitrary points on all possible planforms over a broad range of Mach numbers. From the practical point, it is necessary to introduce many simplifications. These are covered in the discussions to follow.

The surfaces are assumed to be flat plates. This means that the incremental pressure at any point on the planform is due to angle of attack only, and thickness-induced pressures are neglected. This assumption is a reasonable one, except possibly at points near the leading edge. Furthermore, the angle of attack, α, is assumed to be small, so that the pressure distributions are directly proportional to the angle of attack.

The general planform to be considered is depicted in figure 4. The planform is assumed to have a line of symmetry which is parallel to the free-stream direction. The tip chord is approximated by a line parallel to the centerline of the planform.

$$s = \frac{s_L + s_T}{2} \tag{4}$$

For purposes of calculating the pressure coefficient, ΔC_p, the actual planform is replaced by a swept wing which has <u>at station y</u> the same coordinates and slopes of the leading and trailing edges $\left[x_L, \left[\frac{dx_L}{d\eta}\right], x_T, \left[\frac{dx_T}{d\eta}\right]\right]$ as the actual planform. Consider the specific planform in figure 5. The actual (semispan) planform is that described by the straight line segments 0abcde0. In calculating the pressure at point 1, the equivalent planform will be 0agf0. On the other hand, for point 2, the equivalent swept wing will be idchi. Thus, the equivalent swept wing is one with leading and trailing edge sweeps equal to the leading and trailing edge sweeps of the actual wing at station y. This method may be considered as a "quasi-strip" method in that the strip at the pressure spanwise station determines the planform. Yet it is not a strip method per se because finite span effects are accounted for approximately. In fact, if the slopes of the leading and trailing edges of the <u>actual</u> planform are constant, the equivalent planform is the actual planform regardless of where the pressure is to be determined.

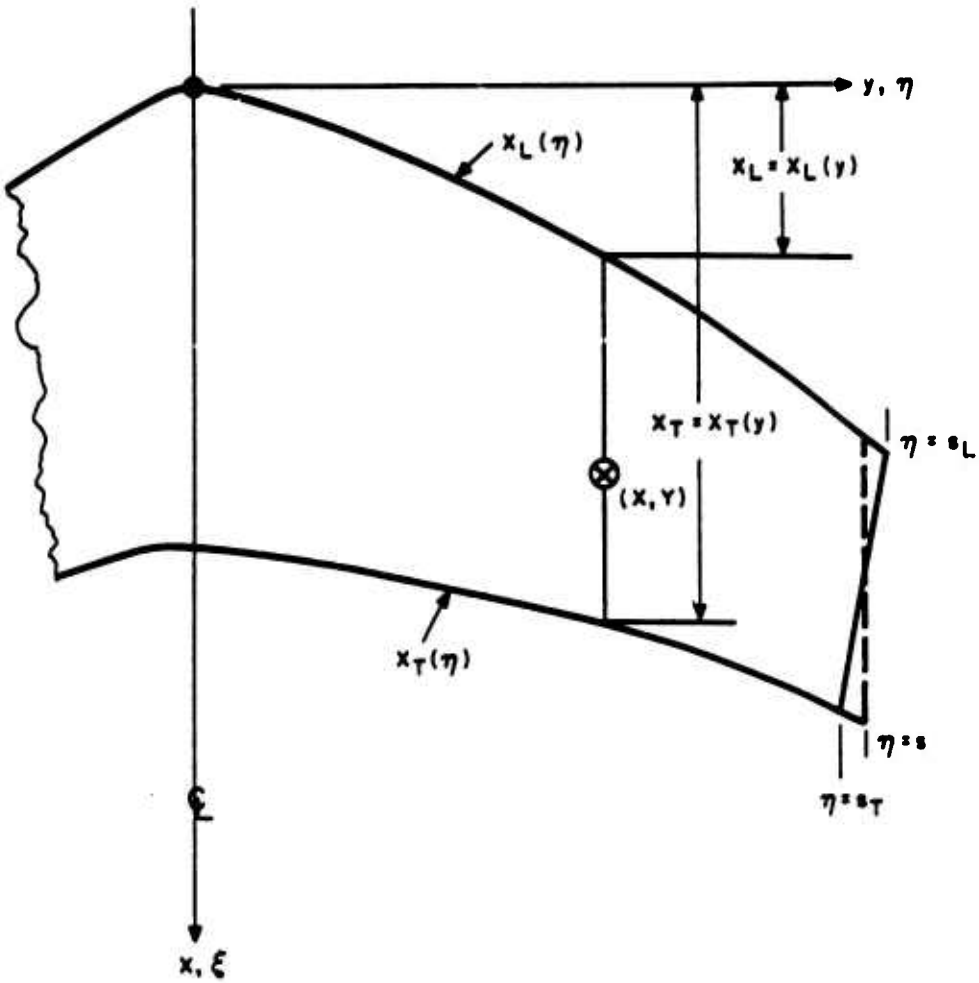

Figure 4. Actual Planform Geometry

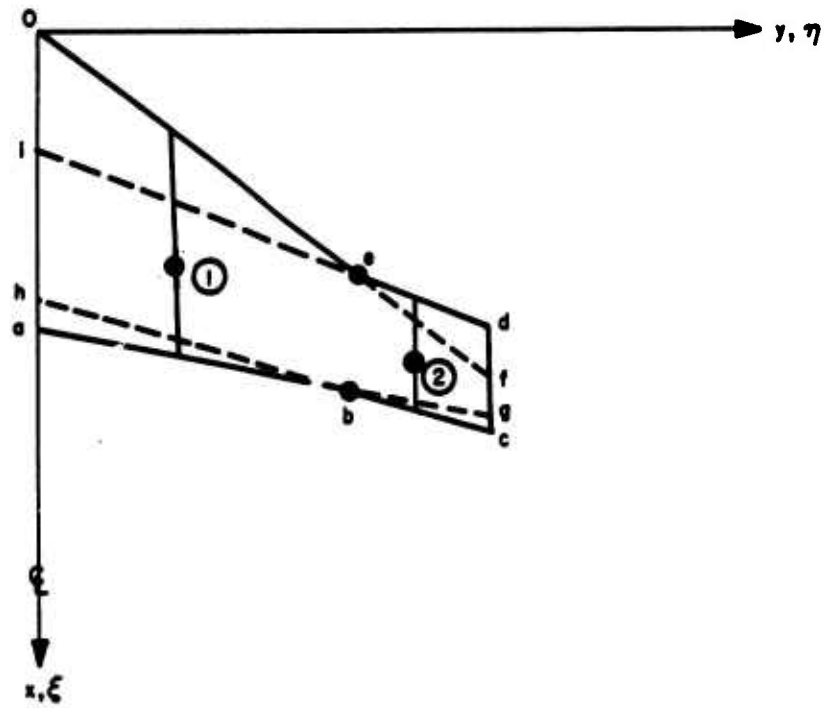

Figure 5. Method of Developing Equivalent Planform

Two possibilities for the semispan, s, can arise: Referring to figure 6, the semi-span of the equivalent wing can be s with the tip chord greater than zero or s_1 with no tip chord. The situation in (b) will not occur too often for actual wings. An example when this occurs is given by (c), where the pressure is to be computed for a point $y < \tilde{y}$. Provisions are made in the formulation and in the computer program to handle cases of types (b) and (c), although they are not expected to be used very often. These cases are numbered 2, 7, 8 and 9 among the possibilities listed in table 1.

The equivalent planform geometry is presented in figure 6. The coordinate systems (x, y) or (ξ,η) of the original planform are retained for convenience, so that the coordinate of the pressure point (x,y) on the actual planform is also the (x,y) on the equivalent planform. It should be noted that the leading and trailing edges intersect the centerline at

$$x_L(0) = x_L - y \tan\Lambda_L \tag{5}$$

$$x_T(0) = x_T - y \tan\Lambda_T \tag{6}$$

When the leading or trailing edge is curved or is composed of segments of straight lines, several equivalent planforms are possible. Each such planform will have its leading and trailing edges described by

$$x_L(\eta) = x_L + (\eta - y) \tan\Lambda_L \tag{7}$$

$$x_T(\eta) = x_T + (\eta - y) \tan\Lambda_T \tag{8}$$

and, in general, the planform apex will not be at $(\xi,\eta) = (0,0)$. The chord at η is defined by the expression

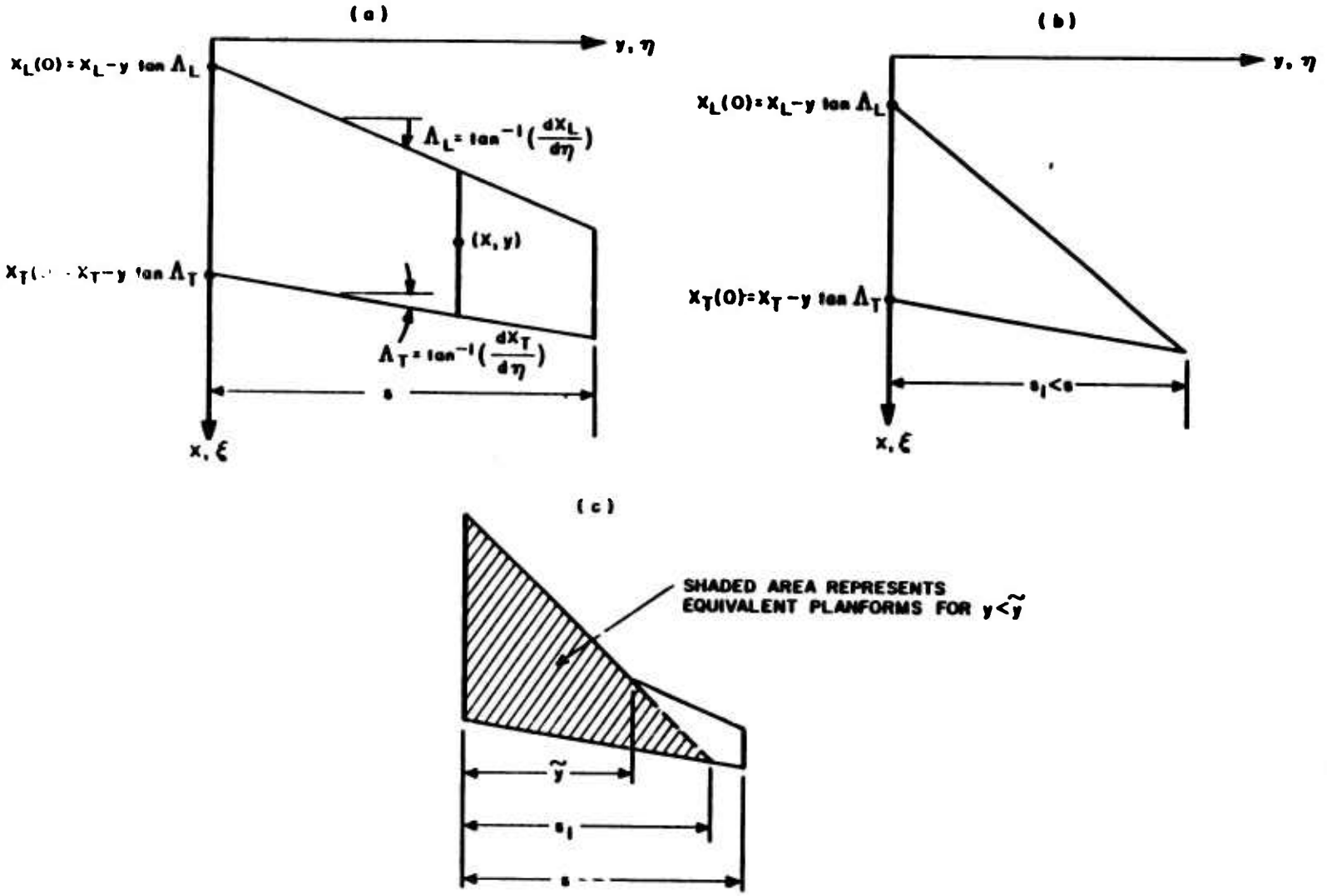

Figure 6. Equivalent Planforms

Table 1

SUMMARY OF CASES INCLUDED IN NOVA

Case No.	Mach Number M	Leading Edge (LE) Condition	Trailing Edge (TE) Condition	Span	Comments
1	<0.8	-	-	s	-
2	<0.8	-	-	s_1	-
3	>1.2	$\beta \cot \Lambda_L > 1$	$\beta \cot \Lambda_T > 1$	s	LE and TE Supersonic
4	>1.2	$\beta \cot \Lambda_L < 1$	$\beta \cot \Lambda_T > 1$	s	LE Subsonic, TE Supersonic
5	>1.2	$\beta \cot \Lambda_L < 1$	$\beta \cot \Lambda_T < 1$	s	LE and TE Subsonic $x_T - y\tan\Lambda_T + s\beta > x_L + (s-y)\tan\Lambda_L$ (Possibility 1)
6	>1.2	$\beta \cot \Lambda_L < 1$	$\beta \cot \Lambda_T < 1$	s	LE and TE Subsonic $x_T - y\tan\Lambda_T + s\beta < x_L + (s-y)\tan\Lambda_L$ (Possibility 2)
7	>1.2	$\beta \cot \Lambda_L > 1$	$\beta \cot \Lambda_T > 1$	s_1	LE and TE Supersonic
8	>1.2	$\beta \cot \Lambda_L < 1$	$\beta \cot \Lambda_T > 1$	s_1	LE Subsonic, TE Supersonic
9	>1.2	$\beta \cot \Lambda_L < 1$	$\beta \cot \Lambda_T < 1$	s_1	LE and TE Subsonic
10	0.8 < M < 1.2	-	-	-	-

β is the Mach number parameter $\sqrt{|M^2-1|}$

$$c(\eta) = x_T(\eta) - x_L(\eta) = (x_T - x_L) + (\eta - y)(\tan\Lambda_T - \tan\Lambda_L) \quad (9)$$

The chord becomes zero when

$$\eta = y + \frac{x_T - x_L}{\tan\Lambda_L - \tan\Lambda_T} \equiv s_1 \quad (10)$$

If $s_1 > s$, the equivalent planform is terminated at $\eta = s$, and corresponds to (a), figure 6.

If $s_1 < s$, the equivalent planform is terminated at $\eta = s_1$ and the taper ratio will be zero. This corresponds to (b), figure 6.

Referring to table 1, Cases 1 and 2 are subsonic situations, Cases 3-9 are supersonic, while Case 10 is transonic. For supersonic flight, distinctions have to be made to reflect leading and trailing edge conditions. Let $\beta = \sqrt{|M^2-1|}$. If $\beta \cot \Lambda > 1$, the edge is supersonic; if $\beta \cot \Lambda < 1$, the edge is subsonic.

In the absence of a better way of determining transonic pressures, Case 10 is programmed to proceed as follows: If $0.8 < M < 1.2$, the pressure is computed for $M = 0.8$ and $M = 1.2$ according to appropriate Cases 1-9. The pressure is then interpolated linearly for the pressure coefficient at the desired Mach number according to

$$(\Delta C_p)_{0.8<M<1.2} = \left(\frac{1.2 - M}{0.4}\right)(\Delta C_p)_{M=0.8} + \left(\frac{M - 0.8}{0.4}\right)(\Delta C_p)_{M=1.2} \quad (11)$$

Table 2 presents a list of certain planform parameters which are useful in the development of the pressure coefficients.

Different approaches are followed for the subsonic and supersonic cases. For supersonic cases, the pressures may be obtained directly from linearized steady supersonic flow, with additional

Table 2

PERTINENT PLANFORM PARAMETERS

PARAMETER	CASES 1, 3-6 inclusive	CASES 2, 7-9 inclusive
Chord at root	$x_T(y) - x_L(y) + y(\tan\Lambda_L - \tan\Lambda_T)$	$x_T(y) - x_L(y) + y(\tan\Lambda_L - \tan\Lambda_T)$
Chord at tip	$x_T(y) - x_L(y) + (y - s)(\tan\Lambda_L - \tan\Lambda_T)$	0
Sweep of LE (Λ_L)	$\Lambda_L = \tan^{-1}\left(\frac{dx_L}{d\eta}\right)_y$	$\Lambda_L = \tan^{-1}\left(\frac{dx_L}{d\eta}\right)_y$
Sweep of TE (Λ_T)	$\Lambda_T = \tan^{-1}\left(\frac{dx_T}{d\eta}\right)_y$	$\Lambda_T = \tan^{-1}\left(\frac{dx_T}{d\eta}\right)_y$
Sweep of C/4 ($\Lambda_{1/4}$)	$\Lambda_{1/4} = \tan^{-1}\left(\frac{3}{4}\tan\Lambda_L + \frac{1}{4}\tan\Lambda_T\right)$	$\Lambda_{1/4} = \tan^{-1}\left(\frac{3}{4}\tan\Lambda_L + \frac{1}{4}\tan\Lambda_T\right)$
Area of both sides (S)	$s[2x_T - 2x_L + (2y - s)(\tan\Lambda_L - \tan\Lambda_T)]$	$s_1[x_T - x_L + y(\tan\Lambda_L - \tan\Lambda_T)]$
Aspect Ratio (A)	$4s^2/S$	$4s_1^2/S$
Taper Ratio (λ)	$\left\{\frac{x_T - x_L + (y - s)(\tan\Lambda_L - \tan\Lambda_T)}{x_T - x_L + y(\tan\Lambda_L - \tan\Lambda_T)}\right\}$	0
$^*\kappa = \left(\frac{C_{\ell_\alpha}}{2\pi/\beta}\right)$	1	1
Modified Aspect Ratio	βA	βA
Modified Sweep	$\Lambda_\beta = \tan^{-1}\left(\frac{\tan\Lambda_{1/4}}{\beta}\right)$	$\Lambda_\beta = \tan^{-1}\left(\frac{\tan\Lambda_{1/4}}{\beta}\right)$

$^*\kappa$ of reference 9 is assumed to be equal to 1.0 and $\beta = \sqrt{|M^2 - 1|}$

approximations for certain regions of the planform. In contrast, for the subsonic cases, the spanwise loadings (lift per unit span) are first determined. The pressures are then determined by assuming a chordwise pressure distribution and determining an "amplitude" for this distribution such that the pressures integrated over the chord give the correct lift per unit span at that station. The distribution used for all subsonic Mach numbers is a modification of the chordwise distribution from thin airfoil theory, and is illustrated in figure 7. Each of the cases will now be discussed individually.

a. Subsonic Cases ($M \leq 0.8$)

Given the location (x,y) on the planform, the quantities x_L, x_T, $\tan\Lambda_L$, $\tan\Lambda_T$ can be determined from the planform geometry. If $s_1 = y + \frac{x_T - x_L}{\tan\Lambda_L - \tan\Lambda_T} > s$, Case 1 is considered; if $s_1 < s$, Case 2 is appropriate. Only Case 1 will be discussed because Case 2 is identical with Case 1, except s is replaced by s_1 and the taper ratio λ is set equal to zero. The parameters

$$\frac{y}{s}\ ,\ \beta,\ \Lambda_\beta,\ \lambda,\ \beta A \left(= \frac{\beta A}{\kappa}\right)^*$$

may be computed according to the expressions given in table 2. Using these parameters, the spanwise loading at y

$$Q\left(\frac{y}{s}\right) = \left(\frac{c\ c_{\ell_a}}{C_L c_{av}}\right) \qquad (12)$$

*κ of reference 9 is taken equal to 1.0.

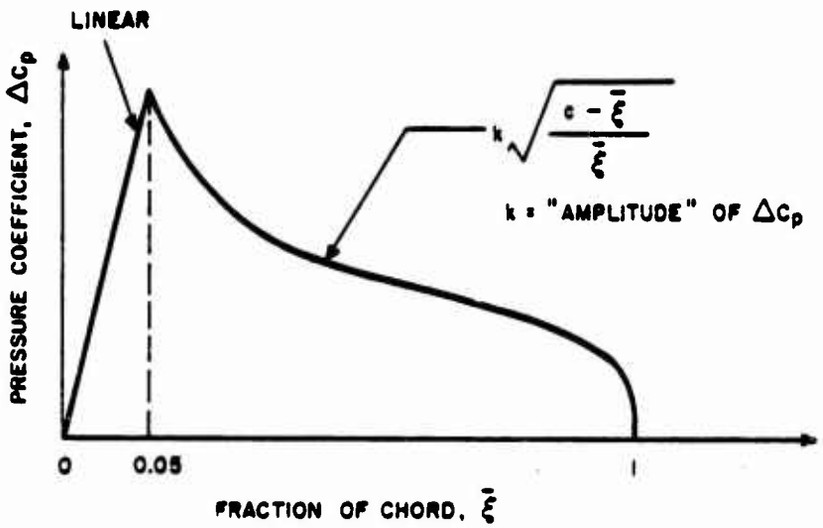

Figure 7. Subsonic Chordwise Pressure Distribution

and

$$\beta C_{L_\alpha} = \frac{\beta C_{L_\alpha}}{\kappa} \quad , \text{ since } \kappa = 1 \tag{13}$$

may be obtained by interpolation from the prepared curves of reference 9. Since these interpolations are over multiple variables, expressions were derived for approximating the curves of figures 3 and 4 of reference 9 to facilitate the interpolation process. The pressure difference coefficients are then computed according to

$$\Delta C_p = C_{L_\alpha} \pi Q \left(\frac{y}{s}\right) f(x) \left(2 + \frac{2y - s}{x_T - x_L} [\tan \Lambda_L - \tan \Lambda_T]\right) \tag{14}$$

where

$$f(x) = \begin{cases} 11.22 \left(\dfrac{x - x_L}{x_T - x_L}\right) , & x_L \leq x < 0.05\, x_T + 0.95\, x_L \\ 0.1287 \sqrt{\dfrac{x_T - x}{x - x_L}} , & 0.05x_T + 0.95x_L \leq x \leq x_T \end{cases} \tag{15}$$

b. Supersonic Cases (M > 1.2)

For supersonic flow, the planform is divided into distinct regions by Mach lines emanating from leading edges of the root chord and the tip chord and by "reflected" Mach lines from other edges as shown in figure 8. For each of these regions, different pressure expressions apply. The particular region in which the point of interest (x,y) lies must be identified as to type of region so that an appropriate pressure formula may be used. To illustrate this brief description, consider Case 3. Depending on the sweep of the Mach line, $\Lambda_{ML} = \tan^{-1}\beta$, three possible situations may arise. These situations are depicted in

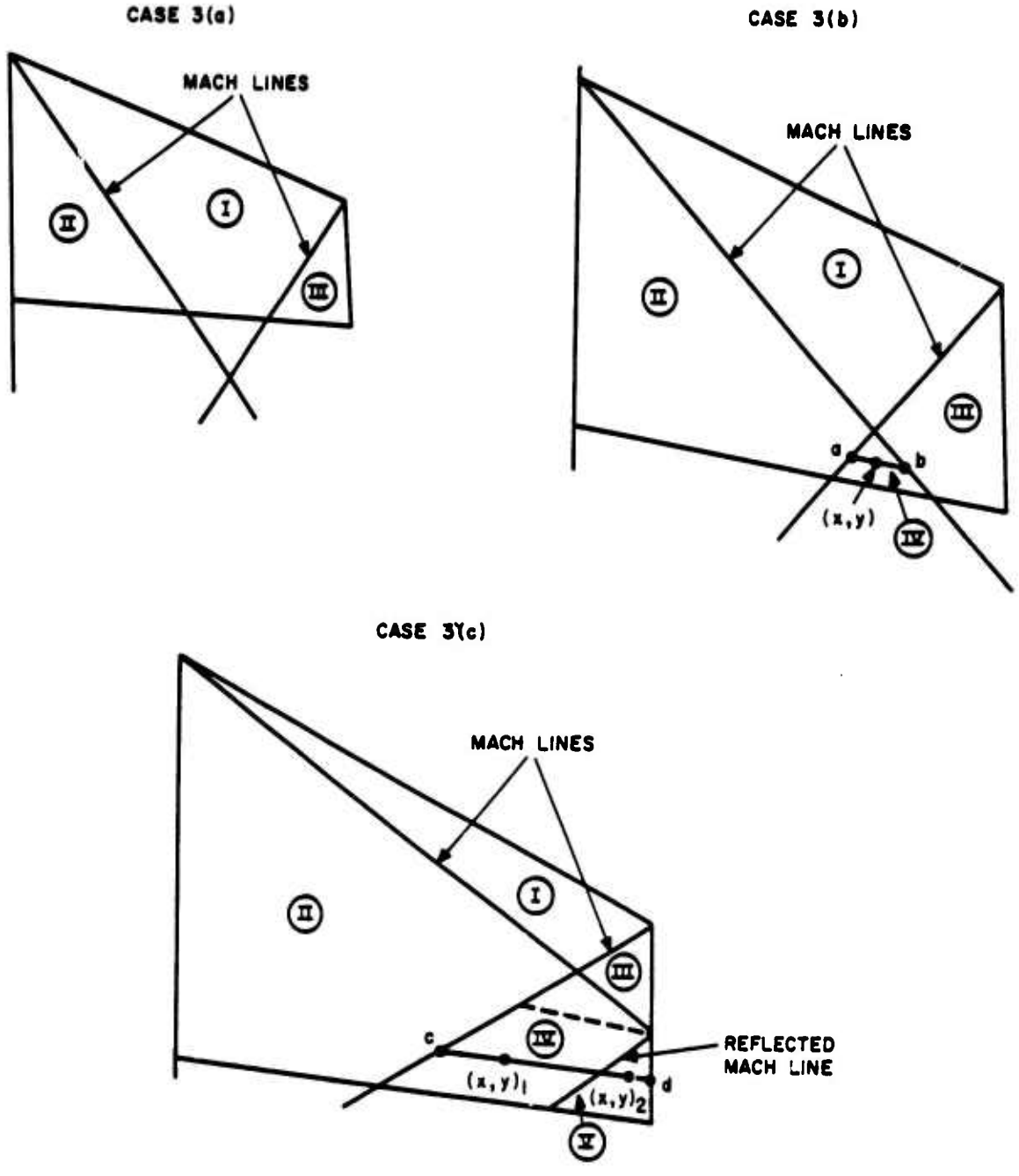

Figure 8. Various Pressure Regions on Planform for Case (3)

figure 8 and are described in references 10 and 11. For points in Region I, the ΔC_p would be the same as on an infinite wing with the same sweep as the leading edge, and is

$$(\Delta C_p)_I = \frac{4 \cot \Lambda_L}{\sqrt{\beta^2 \cot^2 \Lambda_L - 1}} \tag{16}$$

For Region II, the ΔC_p may be obtained from the results for the corresponding region on a delta wing with supersonic leading edges.

$$(\Delta C_p)_{II} = \frac{4 \cot \Lambda_L}{\sqrt{\beta^2 \cot^2 \Lambda_L - 1}} \left[1 - \frac{2}{\pi} \sin^{-1} \sqrt{\frac{1 - \beta^2 \tan^2 \nu}{\beta^2 (\cot^2 \Lambda_L - \tan^2 \nu)}} \right] \tag{17}$$

where

$$\tan^2 \nu = \left(\frac{y}{x - (x_L - y_L \tan \Lambda_L)} \right)^2$$

For Region III, the ΔC_p may be defined by:

$$(\Delta C_p)_{III} = \frac{8 \cot \Lambda_L}{\pi \sqrt{\beta^2 \cot^2 \Lambda_L - 1}} \tan^{-1} \sqrt{\frac{(1 + \beta \cot \Lambda_L)(s-y)}{\cot \Lambda_L [x-(x_L - y \tan \Lambda_L) - s(\tan \Lambda_L) - \beta(s-y)]}} \tag{18}$$

Simple expressions cannot be found for Regions IV and V. For a point (x,y) in Region IV of figure 8(b), the ΔC_p is interpolated linearly between the pressures at points a and b where $(\Delta C_p)_{II}$ and $(\Delta C_p)_{III}$ apply. If $(x,y)_1$ lies in IV, but ahead of the dashed line in figure 8(c), the same procedure may be applied. For $(x,y)_1$ in IV but behind the dashed line, the ΔC_p is interpolated linearly between points c and d; point c has $(\Delta C_p)_{II}$ and ΔC_p for point d is exactly 0. For points in Region V, such as $(x,y)_2$, ΔC_p is also interpolated linearly between points c and d. In all cases, the line along which interpolation takes place is parallel to the trailing edge.

The Mach line patterns for Cases 4, 5, and 6 are as shown in figure 9. For the above cases, only $(\Delta C_p)_{VI}$ can be obtained from known solutions. Using the solution for a delta wing with subsonic edges (refs. 10 and 11), $(\Delta C_p)_{VI}$ is defined in terms of the present coordinate system by

$$(\Delta C_p)_{VI} = \frac{4 \cot \Lambda_L}{\sqrt{1 - \tan^2 \Lambda_L \tan^2 \nu}\, E(k)} \tag{19}$$

where

$$\tan^2 \nu = \left(\frac{y}{x - (x_L - y \tan \Lambda_L)} \right)^2$$

and

$$E(k) = \text{complete elliptical integral}$$

$$= \int_0^{\pi/2} \sqrt{1 - k^2 \sin^2 z}\, dz; \quad k = \sqrt{1 - \beta^2 \cot^2 \Lambda_L} \tag{20}$$

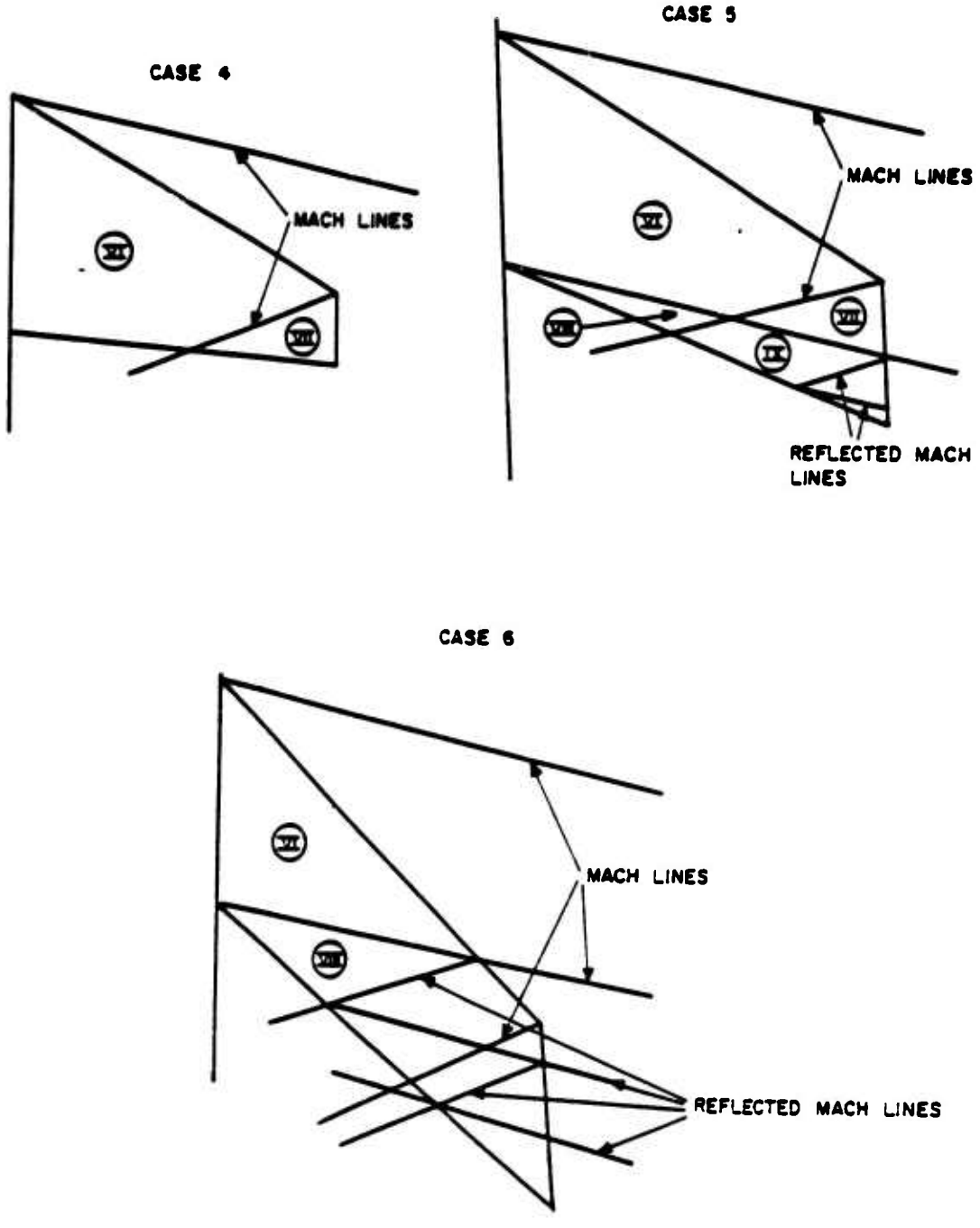

Figure 9. Various Pressure Regions on Planforms for Cases (4), (5) and (6)

For Regions VII and VIII, etc., approximate pressures may be obtained through interpolation, using the pressures along the boundaries of Region VI, and the fact that the pressure must go to zero at the subsonic trailing edge and the tip edge.

Cases 7, 8 and 9, which are shown in figure 10, can be considered as subcases of the previous Case 3, and exhibit the same type of regions. Therefore, the ΔC_p's obtained previously also apply here.

c. Transonic Cases ($0.8 < M < 1.2$)

The pressure coefficient (ΔC_p) for $0.8 < M < 1.2$ may be estimated by linear interpolation over M utilizing the ΔC_p's for $M = 0.8$ and $M = 1.2$, as shown by equation (11).

3.1.2 Blast Airloads on Lifting Surfaces

a. General Discussion of Method

The equations for the aerodynamic loads coefficient, Δc_p due to a blast wave are presented in this section. These coefficients are used in equation (1) for determining the local pressures. The problem to be addressed is the determination of Δc_p as a function of position and time for arbitrary aircraft speed, blast orientation, and blast strength.

Equations for predicting the blast-induced airloads on lifting surfaces for arbitrary strength of the blast shock are not available. References 12 through 18 have however demonstrated that predictions of the difference in loading between opposite surfaces of a wing or tail surface exhibit extensive areas of good agreement with measured loadings where the prediction is based on acoustic theory.

Acoustic theory as applied to thin airfoils is based on the assumption that the airfoil section of a wing or tail, for example,

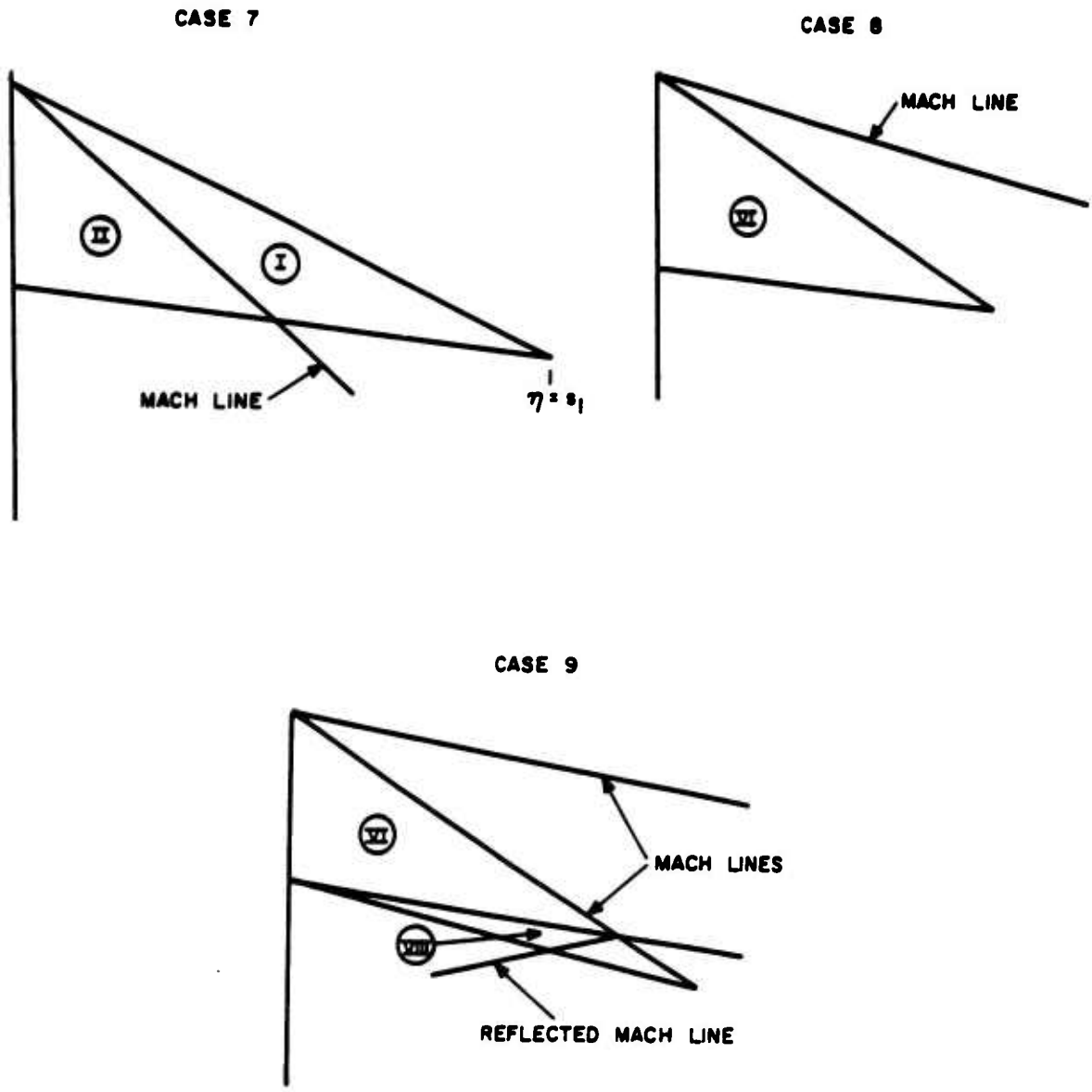

Figure 10. Pressure Regions on Planforms for Cases (7), (8) and (9)

is thin enough relative to the chord and span that the section can be replaced by a line, in this case the camber line. The flow is assumed to be attached to the surface. Acoustic theory has been demonstrated by references 12 through 18 to provide fairly good agreement with measured airloads due to blast and shock waves when the comparison was made in terms of Δc_p. There are a few exceptions to this which must be discussed.

One particular region of the shock loading that has been found to differ from acoustic predictions is in the vicinity of the shock front of a blast-type wave. The measured distribution of Δc_p is found to have a flat-top peak here, in contrast to the singularity predicted by acoustic theory, e.g., reference 17, figure 5. However, it is important to note that the integral over the airfoil of the measured loading coefficient Δc_p is found to agree quite well with the theoretical prediction of acoustic theory, even to blast-induced angles of attack as high as 30 degrees, e.g., reference 17, figure 6a. This result is similar to the well-known leading-edge singularity for subsonic airfoils predicted by linearized theory, where in practice, Δc_p is found to rise to large values near the leading edge. Higher observed values of Δc_p further rearward of the leading edge are found to compensate for the absence of any singularity, however, tending to make the integral over the airfoil of measured Δc_p agree better with theoretical predictions.

At large blast-induced angles of attack, the flow eventually separates from the upper surface, causing Δc_p to drop below the predictions of thin-airfoil theory. Experiments which demonstrate the development of this separation with time are described in references 12 and 17. Because the separation affects the loading at long times relative to the time expected for a typical aircraft surface to respond structurally to the blast overpressure, no attempt is made here to include the complicated variations in loading history at the late times associated with flow separation. It should also be noted that the separation occurs on the low-pressure side of a wing or tail which would generally not be critical to the overpressure effects.

It should also be noted that the nonlinearities in the pressure on the two surfaces tend to compensate each other; the nonlinear increase in $p_\ell - p_\infty$ with angle of attack is accompanied by a nonlinear increase in $p_u - p_\infty$, although the latter tends to be smaller. Therefore, Δc_p tends to show less nonlinearity with angle of attack than do either of the other quantities. No general technique is available at present for predicting nonlinear loadings for the general cases of interest, including effects of shock orientation, airfoil speed, etc. The linear acoustic theory has been developed for a wide variety of cases, so it is employed in the present work.

After a blast wave impinges on a rectangular wing or tail, the pressures generally tend to return to equilibrium much more rapidly from waves moving in a chordwise direction than moving spanwise. Therefore, the analysis will be based on strip theory, considering strips in a chordwise direction. Spanwise effects are expected to take place over times which are long compared to the structural response of interest for overpressure.

Table 3 contains seven blast loading cases of interest as functions of the airfoil Mach number, M, and the gust Mach number, M_g, of the blast shock. For these cases, there are seven forms of the equation for Δc_p.

In the application of the equations, both Mach numbers are taken relative to the flow behind the blast shock, which was demonstrated in reference 14 to provide the best correlation of the airloads with experimental data. The blast radius is assumed to be very large relative to the dimensions of a wing or tail chord, so the blast properties could be taken at any convenient point relative to the chord; the blast properties will be taken at the first point of blast intercept, either the leading or the trailing edge of the airfoil, for determining the blast Δc_p.

Table 3

BLAST LOADING CASES OF INTEREST

Airfoil Mach No. M	Gust Mach No., M_g, of the Blast Shock			
	$M_g < -1$	$-1 < M_g < -M$	$0 < M_g < 1$	$M_g > 1$
$M < 1$	Case 4 Source: WADC TR 57-594 (Ref. 19)	Case 3 Source: Derived	Case 2 Source: WADD TR 60-279 (Ref. 14)	Case 1 Source: WADC TR 57-594 (Ref. 19)
	$M_g < -M$		$0 < M_g < 1$	$M_g > 1$
$M > 1$	Case 7		Case 6	Case 5
	Source: NACA TN 3956 (Ref. 20)			

The Mach number of the airfoil relative to the flow behind the shock is $M = V_r/a_2$, where V_r is the velocity of the fluid behind the shock relative to the airfoil and a_2 is the speed of sound behind the shock. The velocity diagram is shown in figure 11, where V is the airfoil velocity relative to the undisturbed fluid ahead of the shock, and v_b is the fluid velocity of the blast wave.

Relative to the fluid behind the shock, the shock velocity is $V_s - v_b$, where V_s is the shock velocity relative to the undisturbed fluid ahead of the shock.

The shock correlations carried out in references 14 and 17 indicate that the envelopment rate of the shock wave is to be considered relative to the "equivalent" airfoil sketched in figure 11, where the equivalent airfoil is aligned with the total flow, V_r, behind the blast shock. Then, the time Δt for the undisturbed shock to pass over the airfoil is given by

$$V_r + \frac{V_s - v_b}{\cos(\phi - \alpha_2)} = \pm \frac{c}{\Delta t} \tag{21}$$

where ϕ is the angle between the shock outward normal and the plane of the actual airfoil. The positive sign applies for shocks impinging at the leading edge first and the minus sign for shocks impinging at the trailing edge first. Defining the gust Mach number, M_g, of the shock by

$$M_g = \frac{V_s - v_b}{a_2 \cos(\phi - \alpha_2)} \tag{22}$$

and then combining the equations gives

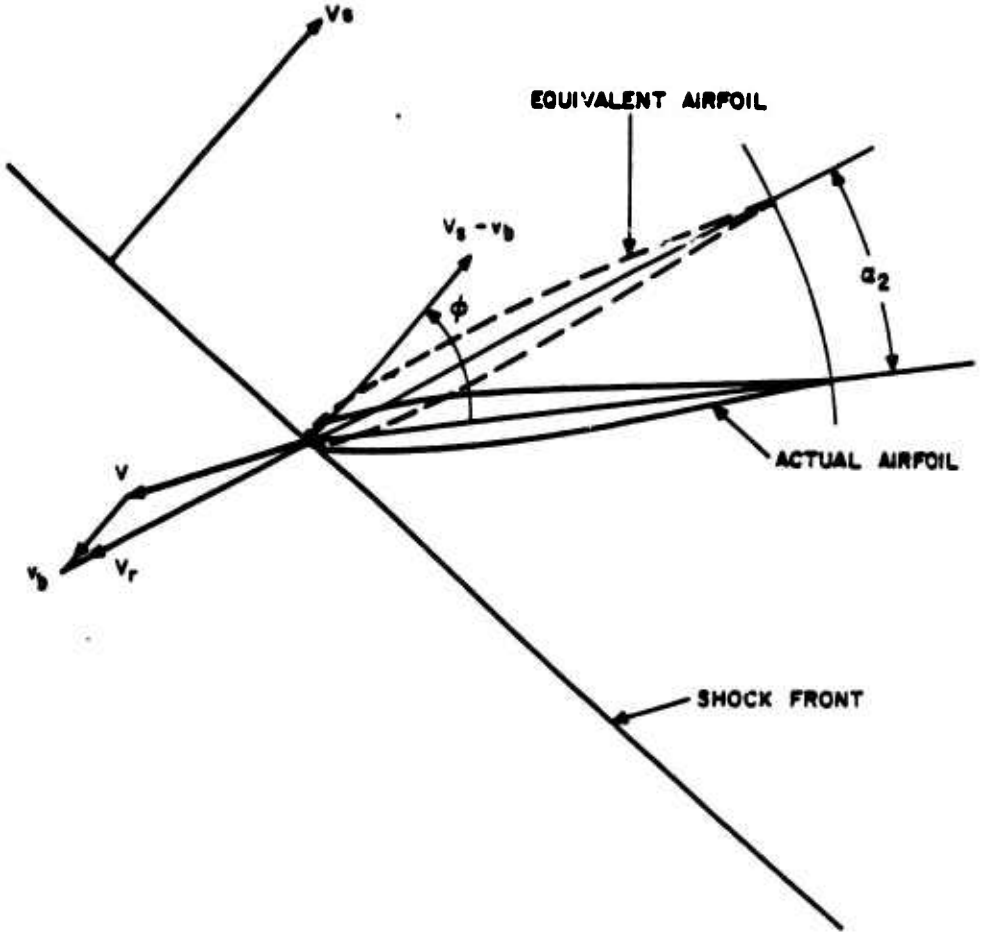

Figure 11. Velocity Diagram Relative to Flow Behind Shock

$$M + M_g = \pm \frac{c}{a_2 \Delta t} \tag{23}$$

Note that M_g can be positive or negative, depending upon the shock orientation relative to the equivalent airfoil; positive for shocks arriving from the front and negative for shocks arriving from the rear. Also, because a shock wave is subsonic relative to the fluid behind it, the absolute value of M_g can be less than unity, thus explaining the presence of such cases in table 3.

b. Discussion of Methods for Various Cases of Airfoil and Shock Mach Numbers

The wave diagrams used here for the seven cases are drawn with the coordinates fixed on the undisturbed fluid at rest ahead of the blast wave in the absence of the airfoil. The airload equations which correspond to figures 12 through 18 are listed in tables 4 through 10. Acoustic theory for thin airfoils assumes that all perturbations to the fluid due to the airfoil and the shock wave are weak. Therefore, acoustic theory is based on the assumption that the angle of attack at all times is small relative to a radian.

The X axis is directed forward with the origin at the point of shock intercept with the leading edge (or with the trailing edge, if the trailing edge is intercepted first) of the airfoil. The trace of the leading edge is represented by Line I in figures 12 through 18. The X coordinate is scaled with the chord, c, so X = -1 at the trailing edge at the time of intercept. The other coordinate in the figures is reduced time T, where T is equal to real time t scaled with the ambient speed of sound, a, and the chord, c. The trace of the trailing edge of the airfoil is represented by Line II.

The equations for Δc_p are given in terms of the actual distance x and the real time, with x = c at the trailing edge. Actual distances and times are related to the scaled distances and time by

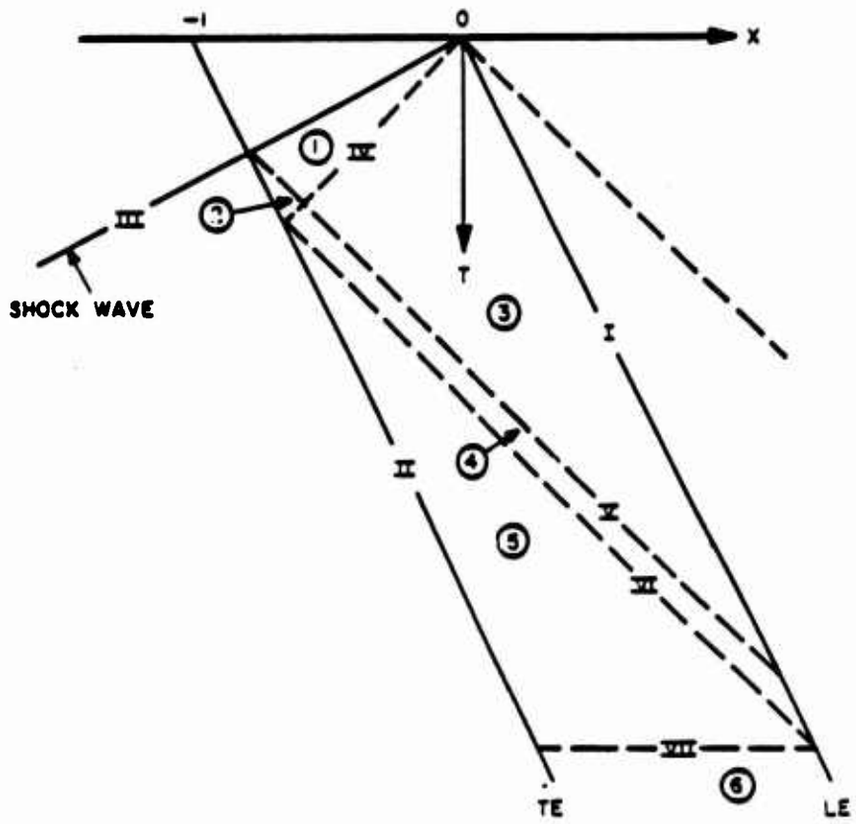

Figure 12. Airload Regions on Airfoil for Case 1 ($M < 1$, $M_g > 1$)

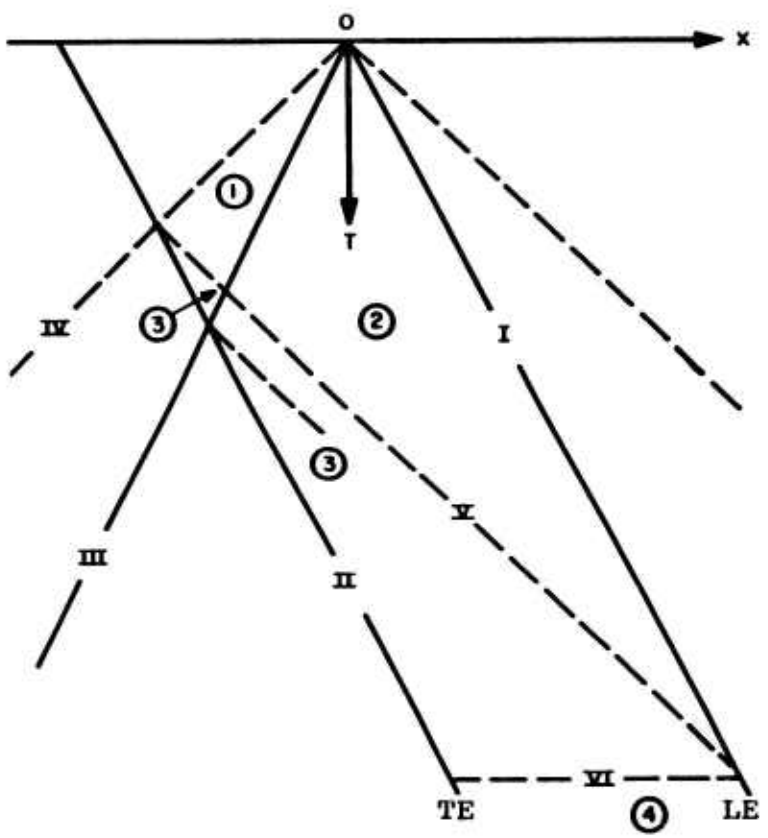

Figure 13. Airload Regions on Airfoil for Case 2 (M < 1, 0 < Mg < 1)

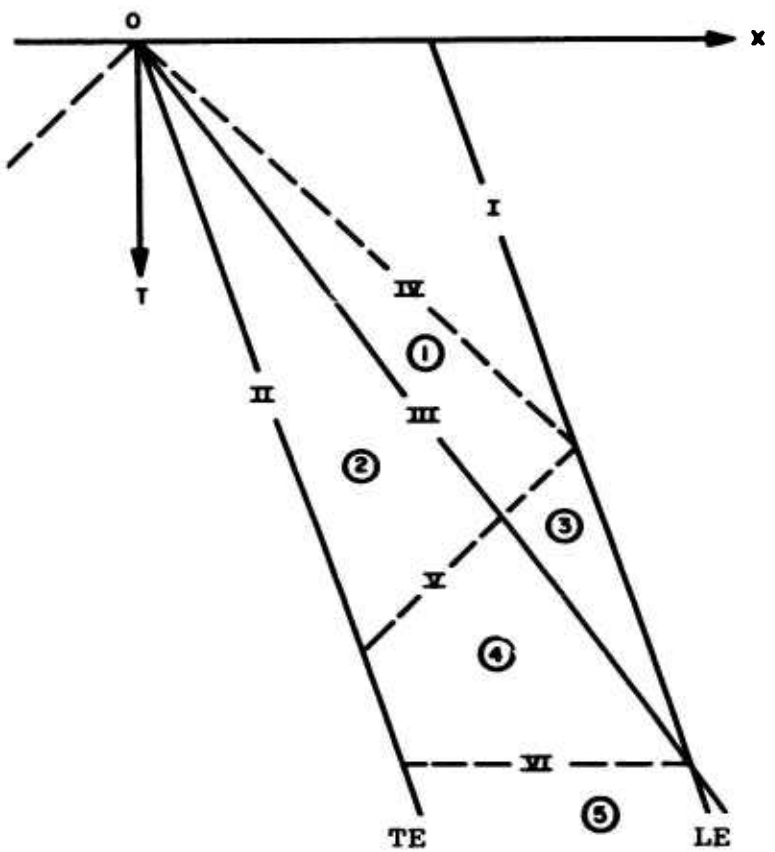

Figure 14. Airload Regions on Airfoil for Case 3 (M < 1, -1 < Mg < -M)

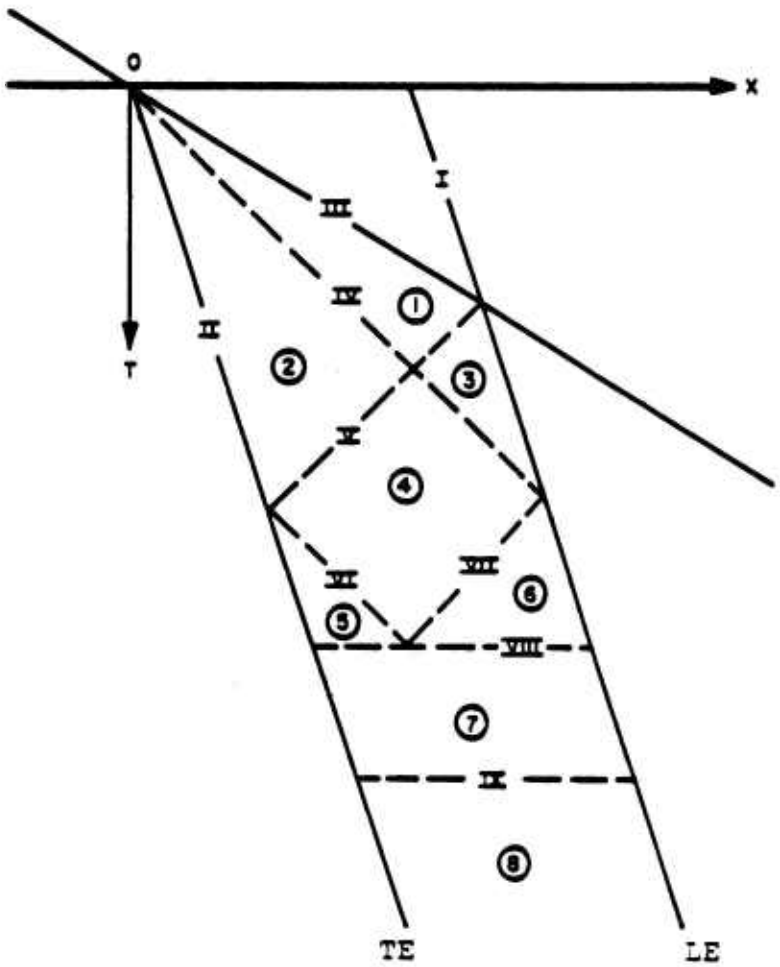

Figure 15. Airload Regions on Airfoil for Case 4 ($M < 1$, $M_g < -1$)

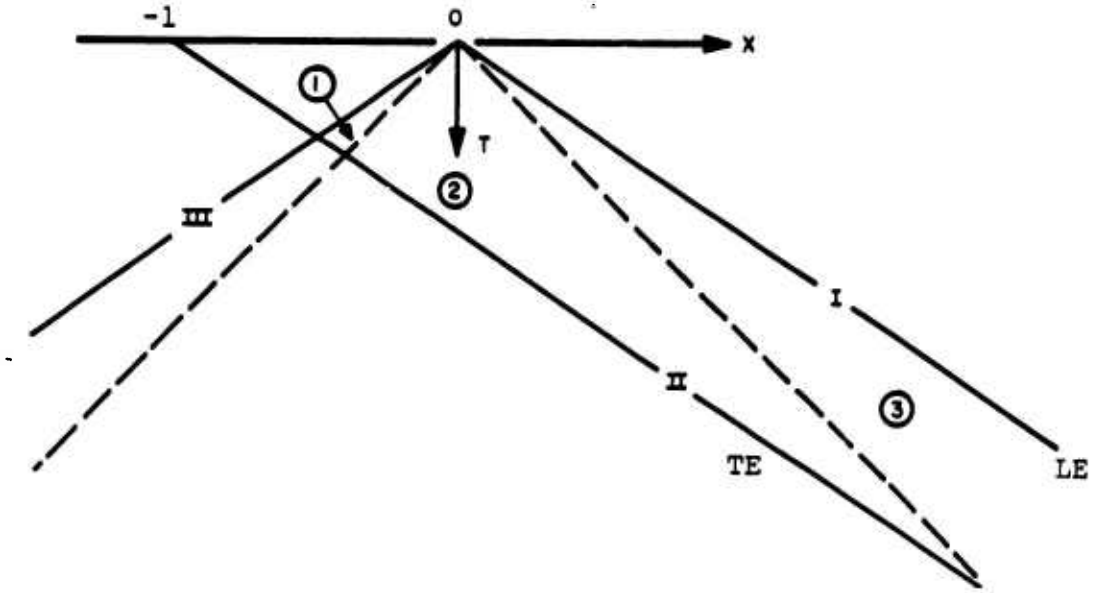

Figure 16. Airload Regions on Airfoil for Case 5 ($M > 1$, $M_g > 1$)

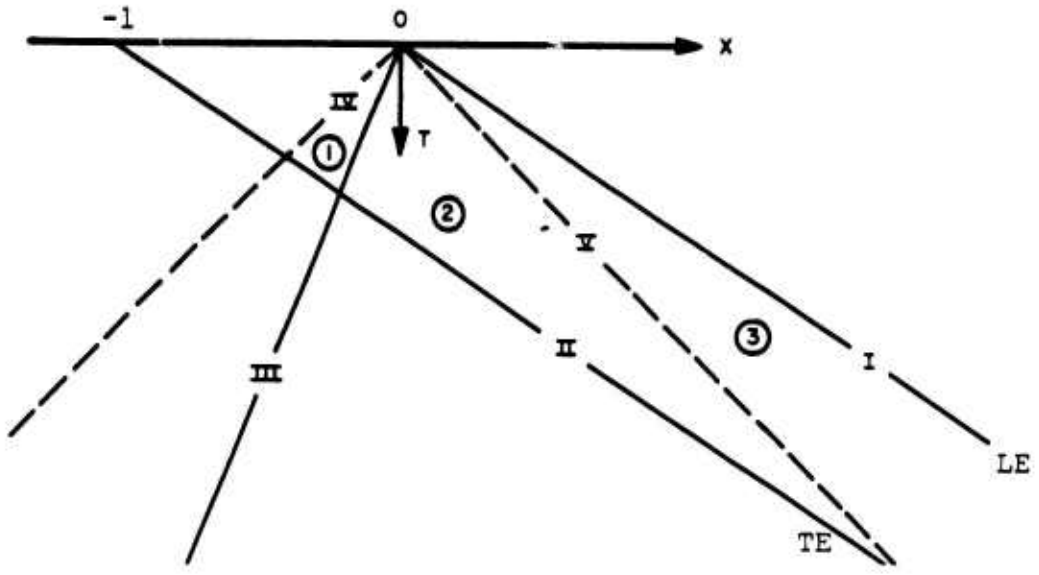

Figure 17. Airload Regions on Airfoil for Case 6 ($M > 1$, $0 < M_g < 1$)

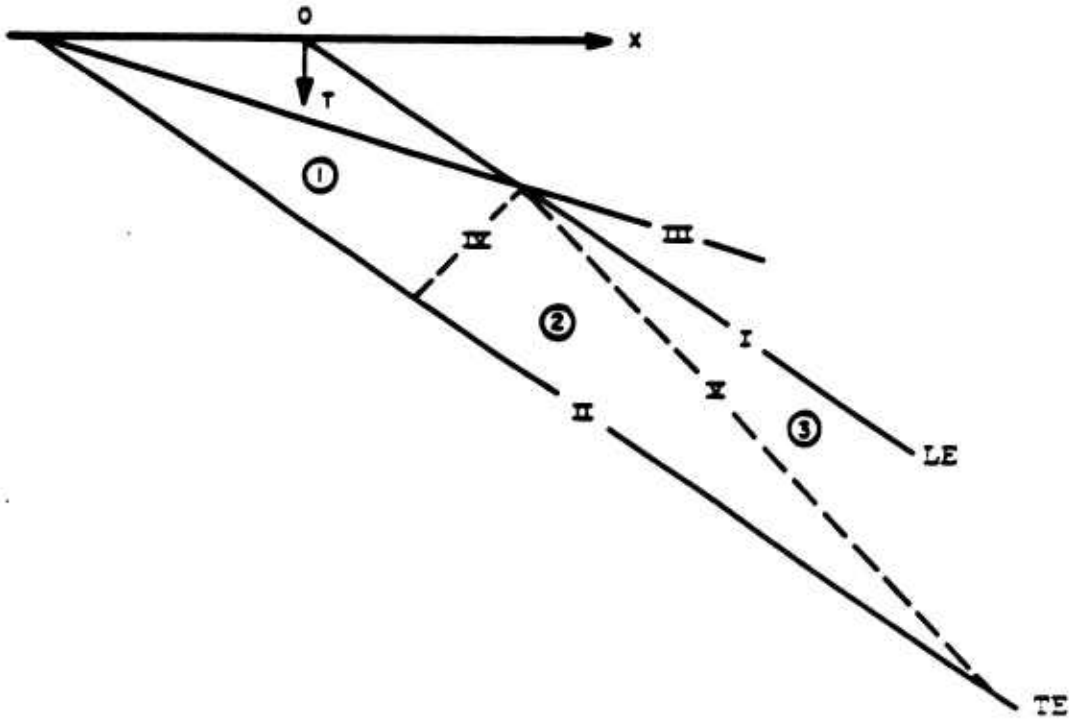

Figure 18. Airload Regions on Airfoil for Case 7 ($M > 1$, $M_g < -M$)

Table 4

AIRLOAD EQUATIONS FOR CASE 1 ($M < 1$, $M_g > 1$)

Line	Equation
I	$x = 0$
II	$x = c$
III	$x = (M + M_g)at$
IV	$x = (M + 1)at$
V	$x = \frac{1 + M_g}{M + M_g} c + (M - 1)at$
VI	$x = \frac{2}{1 + M} c + (M - 1)at$
VII	$t = \frac{2c}{(1+M)(1-M)a}$

Region 1

$$\Delta c_{p_1}(t) = \frac{4}{[M_g^2 - 1]^{1/2}} \frac{|M_g|}{M}$$

Region 2

$$\Delta c_{p_2}(x,t) = \Delta c_{p_1} \left\{ 1 - \frac{2}{\pi} \tan^{-1} \left[\frac{(M+M_g)[(1-M)at + x] - (1+M_g)c}{(1 + M_g)(c - x)} \right]^{1/2} \right\}$$

Region 3

$$\Delta c_{p_3}(x,t) = \Delta c_{p_1} \left\{ 1 - \frac{2}{\pi} \tan^{-1} \left[\frac{M + M_g}{M_g - 1} \frac{(M + 1)at - x}{x} \right]^{1/2} \right.$$

$$\left. + \frac{2}{\pi} \frac{M}{M_g(1 + M)} \left[\frac{(M_g-1)(M_g+M)[(M+1)at - x]}{x} \right]^{1/2} \right\}$$

Table 4 (Cont'd)

AIRLOAD EQUATIONS FOR CASE 1 ($M < 1$, $M_g > 1$)

Region 4

$$\Delta c_{p_4}(x,t) = \Delta c_{p_2}(x,t) + \Delta c_{p_3}(x,t) - \Delta c_{p_1}(t)$$

Region 5

$$\Delta c_{p_5}(x,t) = \left[\frac{c-x}{x}\right]^{1/2} \phi(t)$$

where

$$\phi(t) = \Delta c_{p_4}(x_{VI},t) \left[\frac{x_{VI}}{c - x_{VI}}\right]^{1/2}$$

$$x_{VI} = \frac{2}{1 + M} c + (M - 1)at$$

Region 6

$$\Delta c_{p_6}(x) = \frac{4}{[1-M^2]^{1/2}} \left[\frac{c-x}{x}\right]^{1/2}$$

Table 5

AIRLOAD EQUATIONS FOR CASE 2 ($M < 1$, $0 < M_g < 1$)

Line	Equation
I	$x = 0$
II	$x = c$
III	$x = (M + M_g)at$
IV	$x = (M + 1)at$
V	$x = \frac{2}{M + 1} c + (M - 1)at$
VI	$t = \frac{2c}{(1+M)(1-M)a}$

Region 1

$$\Delta c_{p_1}(x,t) = \frac{8}{\pi} \left\{ \frac{1}{1+M} \left[\frac{(M+M_g)\,[(1+M)at - x]}{(1+M_g)x} \right]^{1/2} + \frac{M_g}{M[1-M_g^{\,2}]^{1/2}} \ln \frac{[(1-M_g)x]^{1/2} + \{(M+M_g)[(1+M)at-x]\}^{1/2}}{[(1+M)\{x-(M+M_g)at\}]^{1/2}} \right\}$$

Region 2

$$\Delta c_{p_2}(x,t) = \frac{8}{\pi} \left\{ \frac{1}{1+M} \left[\frac{(M+M_g)\,[(1+M)at-x]}{(1+M_g)x} \right]^{1/2} + \frac{M_g}{M[1-M_g^{\,2}]^{1/2}} \ln \frac{[(1-M_g)x]^{1/2} + \{(M+M_g)[(1+M)at - x]\}^{1/2}}{[(1+M)\{(M+M_g)at - x\}]^{1/2}} \right\}$$

Table 5 (Cont'd)

AIRLOAD EQUATIONS FOR CASE 2 ($M < 1$, $0 < M_g < 1$)

Region 3

$$\Delta c_{p_3}(x,t) = \frac{4}{\sqrt{1-M^2}} \sqrt{\frac{c-\bar{\bar{x}}}{\bar{\bar{x}}}}$$

$$\bar{\bar{x}}(x,t) = c - \frac{c-\bar{x}(t)}{c-x_v(t)} (c-x)$$

$$\bar{x}(t) = \frac{c}{1+A^2}$$

$$A = \frac{\sqrt{1-M^2}\ \Delta c_{p_{1,2}}(x_v,t)}{4}$$

$$\Delta c_{p_{1,2}} \begin{cases} \Delta c_{p_1}, & \frac{1}{1+M} \leq \frac{at}{c} < \frac{2}{(1+M)(1+M_g)} \\ \Delta c_{p_2}, & \frac{2}{(1+M)(1+M_g)} < \frac{at}{c} \leq \frac{2}{(1-M)(1+M)} \end{cases}$$

$$x_v = at\,(M-1) + 2c/1+M$$

Region4

$$\Delta c_{p_4}(x) = \frac{4}{\sqrt{1-M^2}} \sqrt{\frac{c-x}{x}}$$

Table 6

AIRLOAD EQUATIONS FOR CASE 3 ($M < 1$, $-1 < M_g < -M$)

Line	Equation
I	$x = 0$
II	$x = c$
III	$x = c + (M+M_g)at$
IV	$x = c + (M-1)at$
V	$x = \frac{M+1}{M-1} c + (M+1)at$
VI	$t = - \frac{c}{(M+M_g)a}$

Region 1

$$\Delta c_{p_1}(x,t) = - \frac{4M_g}{\pi M[1-M_g^2]^{1/2}} \cosh^{-1} \left\{ \frac{(1+M_g)(c-x)}{(1-M)[(M+M_g)at+c-x]} \right\}^{1/2}$$

Region 2

$$\Delta c_{p_2}(x,t) = - \frac{4M_g}{\pi M[1-M_g^2]^{1/2}} \cosh^{-1} \left\{ 1 - \frac{(1+M_g)(c-x)}{(1-M)[(M+M_g)at+c-x]} \right\}^{1/2}$$

Region 3

$$\Delta c_{p_3}(x,t) = - \frac{4M_g}{\pi M[1-M_g^2]^{1/2}} \cosh^{-1} \left[\frac{(M+M_g)at + c}{(M+M_g)at+c-x} \right]^{1/2}$$

Table 6 (Cont'd)

AIRLOAD EQUATIONS FOR CASE 3 ($M < 1$, $-1 < M_g < -M$)

Region 4

$$\Delta c_{p_4}(x,t) = \Delta c_{p_2}(x,t)$$

Region 5

$$\Delta c_{p_5}(x,t) = 4 \left[\frac{c-x}{(1-M^2)x}\right]^{1/2} \Phi(t)$$

where

$$\Phi(t) = \frac{1 + \tau}{2 + \tau}$$

$$\tau = \frac{at}{c} + \frac{1}{M+M_g}$$

Table 7

AIRLOAD EQUATIONS FOR CASE 4 ($M < 1$, $M_g < -1$)

Line	Equation
I	$x = 0$
II	$x = c$
III	$x = c + (M+M_g)at$
IV	$x = c + (M-1)at$
V	$x = \frac{M+1}{M+M_g} c + (M+1)at$
VI	$x = \frac{M^2+2(M+M_g)-1}{(M+M_g)(M+1)} c + (M-1)at$
VII	$x = \frac{M+1}{M-1} c + (M+1)at$
VIII	$t = \left\{ \frac{1}{1-M} + \frac{(M_g-1)(1-M)}{2(M_g+M)(1+M)} \right\} \frac{c}{a}$
IX	$t = \left\{ \frac{2-M}{1-M} + \frac{(M_g-1)(1-M)}{2(M_g+M)(1+M)} \right\} \frac{c}{a}$

Region 1

$$\Delta c_{p_1}(t) = \frac{4|M_g|}{M[M_g^2 - 1]^{1/2}}$$

Region 2

$$\Delta c_{p_2}(x,t) = \Delta c_{p_1}(x,t) \left\{ 1 - \frac{2}{\pi} \tan^{-1} \left[\frac{(M_g+M)(x-at(M-1)-c)}{(M_g+1)(c-x)} \right]^{1/2} \right\}$$

Table 7 (Cont'd)

AIRLOAD EQUATIONS FOR CASE 4 ($M < 1$, $M_g < -1$)

Region 3

$$\Delta c_{p_3}(x,t) = \Delta c_{p_1}(x,t)\left\{1 - \frac{2}{\pi}\tan^{-1}\left[\frac{(M+M_g)[at(1+M)-x] + c(M+1)}{(M_g - 1)x}\right]^{1/2}\right.$$

$$\left. - \frac{2}{\pi}\frac{M}{M_g(1+M)}\left[\frac{(M_g-1)}{x}\left[(M+M_g)[at(1+M)-x] + c(M+1)\right]\right]^{1/2}\right\}$$

Region 4

$$\Delta c_{p_4}(x,t) = \Delta c_{p_2}(x,t) + \Delta c_{p_3}(x,t) - \Delta c_{p_1}(x,t)$$

Region 5

$$\Delta c_{p_5}(x,t) = \left[\frac{c - x}{-x}\right]^{1/2} \Phi(t)$$

where

$$\Phi(t) = \Delta c_{p_4}(x_{VI},t)\left[\frac{x_{VI}}{c - x_{VI}}\right]^{1/2}$$

$$x_{VI} = \frac{2}{1 + M}c + (M-1)at$$

Table 7 (Cont'd)

AIRLOAD EQUATIONS FOR CASE 4 ($M < 1$, $M_g < -1$)

Region 6

$$\Delta c_{p_6}(x,t) = \left[\frac{c - x}{x}\right]^{1/2} \Psi(t)$$

where

$$\Psi(t) = \Delta c_{p_4}(x_{VII},t) \left[\frac{x_{VII}}{c - x_{VII}}\right]^{1/2}$$

$$x_{VII} = (M+1)at - \frac{M}{1 - M} c$$

Region 7

$$\Delta c_{p_7}(x,t) = \Delta c_{p_6}(x,t_{VIII}) + \frac{k(x)a}{c} (t-t_{VIII})$$

$$t_{VIII} = \left(\frac{1}{1-M} + \frac{(M_g-1)(1-M)}{2(M_g+M)(1+M)}\right) \frac{c}{a}$$

$$k(x) = \Delta c_{p_8}(x) - \Delta c_{p_6}(x,t_{VIII})$$

Region 8

$$\Delta c_{p_8}(x) = 4 \left[\frac{c-x}{(1-M^2)x}\right]^{1/2}$$

Table 8

AIRLOAD EQUATIONS FOR CASE 5 ($M > 1$, $M_g > 1$)

Line	Equation
I	$x = 0$
II	$x = c$
III	$x = (M+M_g)at$
IV	$x = (M+1)at$
V	$x = (M-1)at$

Region 1

$$\Delta c_{p_1} = \frac{4M_g}{M[M_g^2 - 1]^{1/2}}$$

Region 2

$$\Delta c_{p_2}(x,t) = \frac{4}{\pi M}\left\{\frac{M}{(M^2-1)^{1/2}}\cos^{-1}\left[\frac{Mx-at(M^2-1)}{x}\right]\right.$$

$$\left. + \frac{M_g}{(M_g^2-1)^{1/2}}\cos^{-1}\left[\frac{at(M_gM+1) - M_gx}{|at(M_g+M)-x|}\right]\right\}$$

Region 3

$$\Delta c_{p_3}(t) = \frac{4}{(M^2-1)^{1/2}}$$

Table 9

AIRLOAD EQUATIONS FOR CASE 6 ($M > 1$, $0 < M_g < 1$)

Line	Equation
I	$x = 0$
II	$x = c$
III	$x = (M+M_g)at$
IV	$x = (M+1)at$
V	$x = (M-1)at$

Region 1

$$\Delta c_{p_1}(x,t) = \frac{4}{\pi M}\left\{\frac{M}{(M^2-1)^{1/2}}\cos^{-1}\left[\frac{Mx-at(M^2-1)}{x}\right]\right.$$

$$\left. + \frac{M_g}{(1-M_g^2)^{1/2}}\cosh^{-1}\left[\frac{at(M_gM+1) - M_gx}{|(M_g+M)at-x|}\right]\right\}$$

Region 2

$$\Delta c_{p_2}(x,t) = \Delta c_{p_1}(x,t)$$

Region 3

$$\Delta c_{p_3}(x,t) = \frac{4M_g}{M(1-M_g^2)^{1/2}}$$

Table 10

AIRLOAD EQUATIONS FOR CASE 7 ($M > 1$, $M_g < -M$)

Line	Equation
I	$x = 0$
II	$x = c$
III	$x = c + (M+M_g)at$
IV	$x = \frac{M+1}{M+M_g} c + (M+1)at$
V	$x = \frac{M-1}{M+M_g} c + (M-1)at$

Region 1

$$\Delta c_{p_1}(t) = -\frac{4M_g}{M(M_g^2-1)^{1/2}}$$

Region 2

$$\Delta c_{p_2}(x,t) = \frac{4}{\pi M}\left\{\frac{M}{(M^2-1)^{1/2}}\cos^{-1}\left[\frac{(M+M_g)\,[Mx-at(M^2-1)]-(M^2-1)c}{(M+M_g)x}\right]\right.$$

$$\left. - \frac{M_g}{(M_g^2-1)^{1/2}}\cos^{-1}\left[\frac{(M+M_g)\{(1+MM_g)at-M_gx\}+(1+MM_g)c}{(M+M_g)\{c-x+(M+M_g)at\}}\right]\right\}$$

Region 3

$$\Delta c_{p_3}(t) = \frac{4}{(M^2-1)^{1/2}}$$

$$T = \frac{at}{c} \tag{24}$$

$$X = \begin{cases} -\frac{x}{c} + \frac{Vt}{c}, & \text{leading edge intercepted first} \\ \frac{c-x}{c} + \frac{Vt}{c}, & \text{trailing edge intercepted first} \end{cases} \tag{25}$$

The dynamic pressure $q = \frac{1}{2}\rho_\infty V_r^2$ and ambient pressure p_∞ used to calculate the local pressure on the airfoil are based on the preblast values of p_∞, ρ_∞, and V_r until Δc_p becomes nonzero. After that time, the blast values of p_∞, ρ_∞ and V_r at the leading edge of the airfoil are used.

(1) Subsonic Flight Speed ($M < 1$)

(a) Case 1: $M_g > 1$

The equations for Δc_p in Case 1 were derived by Smiley and Krasnoff (ref. 19). The shock wave first intercepts the wing at leading edge and sweeps over the airfoil at a speed greater than sound as shown in figure 12. Region 1 lies between the shock wave III and the rearward emanating wave IV. These waves, in turn, reflect waves V and VI when they reach the trailing edge, forming Regions 2, 3, and 4.

Extensive calculations are required to determine Δc_p in Region 5, yet the distribution of Δc_p is rather simple in form, blending from the value at reflected wave VI to the zero value at the trailing edge. The loading in this region is relatively unimportant, so the steady-state distribution for Δc_p is obtained by scaling to match Δc_p at reflected wave VI. When reflected wave VI reaches the leading edge, a steady-state pressure distribution exists over the entire airfoil.

(b) Case 2: $0 < M_g < 1$

The solution for Δc_p for Case 2 was derived by Ruetenik (ref. 14) for Regions 1 and 2. No solution has been obtained for Region 3 due to the complexity of the interaction between the singular distributions of loading in Regions 1 and 2 with the wake. The distribution of Δc_p for Region 3 is obtained by using the steady-state distribution for Δc_p and matching with Δc_p at reflected wave V. The matching is accomplished by a linear stretching of the coordinates, based on distance from the trailing edge, to match the loading with the loading along wave V. The specific equations used are

$$\Delta c_p\,(x,t) = \frac{4}{\sqrt{1-M^2}} \sqrt{\frac{c-\bar{\bar{x}}}{\bar{\bar{x}}}} \tag{26}$$

$$\bar{\bar{x}} = c - \frac{c - \bar{x}(t)}{c - x_V(t)}\,(c - x) \tag{27}$$

with $\bar{x}(t)$ defined by

$$\frac{4}{\sqrt{1-M^2}} \sqrt{\frac{c - \bar{x}(t)}{\bar{x}(t)}} = \Delta c_{p_{1,2}}(x_V,t) \tag{28}$$

where $\Delta c_{p_{1,2}}(x_V,t)$ is the value of Δc_p along wave V for Region 1 or 2, as appropriate, and $x_v(t)$ is the chordwise position of wave V. The steady-state distribution of Δc_p is reached when wave V intercepts the leading edge of the airfoil. This concurs with the time required to reach steady-state as indicated by equation (59), reference 21. The steady-state distribution for Δc_p applies after wave V intercepts the leading edge.

(c) Case 3: $-1 < M_g < -M$

In Case 3, the shock arrives from the trailing edge, traveling forward faster than the airfoil Mach number but slower than the speed of sound. The wave diagram is shown in figure 14.

The equations for Δc_p for Regions 1, 2 and 3 were derived using the transformation from the two-dimensional supersonic steady-state wing to the transient one-dimensional airfoil along with the equations for the loading given in Section A13, reference 11. The loading in Region 4 is nearly the same as in Region 2, except for a slight perturbation from Region 3. Because the loading in Region 2 is small, the Δc_p value for Region 4 is obtained using the equation for Region 2.

The steady-state loading distribution is used for Region 5, scaling the distribution asymptotically, following equation (18), reference 21. All values of Δc_p in Region 5 are scaled by the factor $\Phi(\tau)$.

$$\Phi = 1 - \frac{1}{2 + \tau} \tag{29}$$

$$\tau = \frac{at}{c} + \frac{1}{M + M_g} \tag{30}$$

The time factor $\Phi(\tau)$ varies from 0.5 when the blast shock reaches the leading edge, to a maximum of 1.0.

(d) Case 4: $M_g < -1$

In this situation, the blast shock overtakes the airfoil from the rear at a speed greater than the speed of sound. The equation for Δc_p for Regions 1 through 4 are taken from Smiley and Krasnoff (ref. 19). In Regions 5 and 6, the equation for the steady-state distribution of Δc_p is matched to Region 4.

(2) Supersonic Flight Speed (M > 1)

The equations for all regions in Cases 5, 6, and 7 were obtained from table 3 of reference 20.

3.2 LOADING ON FUSELAGE SURFACES: PREBLAST AND BLAST ENCOUNTER

Since the fuselage shape is not known a priori, it is difficult to set up a practical, yet rational, procedure for computing the time variation of the pressure at an arbitrary point on the actual fuselage. The devised procedure is an attempt to estimate the pressures, admitting the fact that much of it is based on intuition and involves many simplifications (which have been adopted in related situations, e.g., see Norris and Hansen, reference 22) which may not be fully justifiable for certain configurations.

If wind tunnel data were available for the particular fuselage, such data could be used. These data would have to include pressure coefficients at a sufficient number of points on the fuselage for a range of Mach numbers and Reynolds numbers. They would also have to cover a wide range of angles of attack and angles of yaw, and combinations thereof. Unfortunately, such extensive data are never obtained for actual configurations. In addition, the variety of configurations encountered prevents the use of one set of data for all configurations.

Other theoretical means are available. Methods have been devised to determine pressures on bodies at subsonic and supersonic speeds for certain types of bodies. Methods for subsonic and supersonic cylindrical bodies (e.g., refs. 23-26) are not only limited but also extremely laborious. They are rejected here on practical grounds recognizing, in addition, that other aspects of the problem can only be treated in very approximate fashion. The Munk-Jones slender-body theory or the linearized supersonic theory for pointed bodies of revolution will be of some help. The Munk-Jones theory gives running loads

per unit body length, independent of Mach number, and considers only those additional pressures due to angle of attack. It has certain complications if the cross section is not circular. Both of the slender-body theories (Munk-Jones and linearized supersonic theory for pointed bodies of revolution) are Mach number independent for the pressures induced by angle of attack. The pressures at zero angles of attack can be obtained for the supersonic case; however, they are Mach number dependent, and cannot be easily introduced.

The point is that neither sufficient data nor well-established practical methods exist to perform even the steady-state calculations of pressures called for in the present problem for the preblast and post-diffractive phases of the pressure-time histories. The rough approximations which are described below appear to offer the best solution.

Consider the two bodies in figure 19, where the actual fuselage, (a), and an equivalent body of revolution, (b), have the same cross-sectional area distributions along their lengths. For purposes of equating the pressures on the two bodies, points on the two bodies may be related according to either of the two following schemes

(a) $\tilde{X}_b = \tilde{X}_B \leftrightarrow X_b = X_B$

$$\tilde{\theta} \leftrightarrow \theta, \text{ i.e., } \frac{\tilde{y}_b}{\tilde{z}_b} \leftrightarrow \frac{y_b}{z_b}$$

(b) $\tilde{X}_b = \tilde{X}_B \leftrightarrow X_b = X_B$

$$\left(\frac{\partial \tilde{y}_b}{\partial z_b}\right)_{\tilde{X}_B} \leftrightarrow \left(\frac{\partial y_b}{\partial z_b}\right)_{X_B}$$

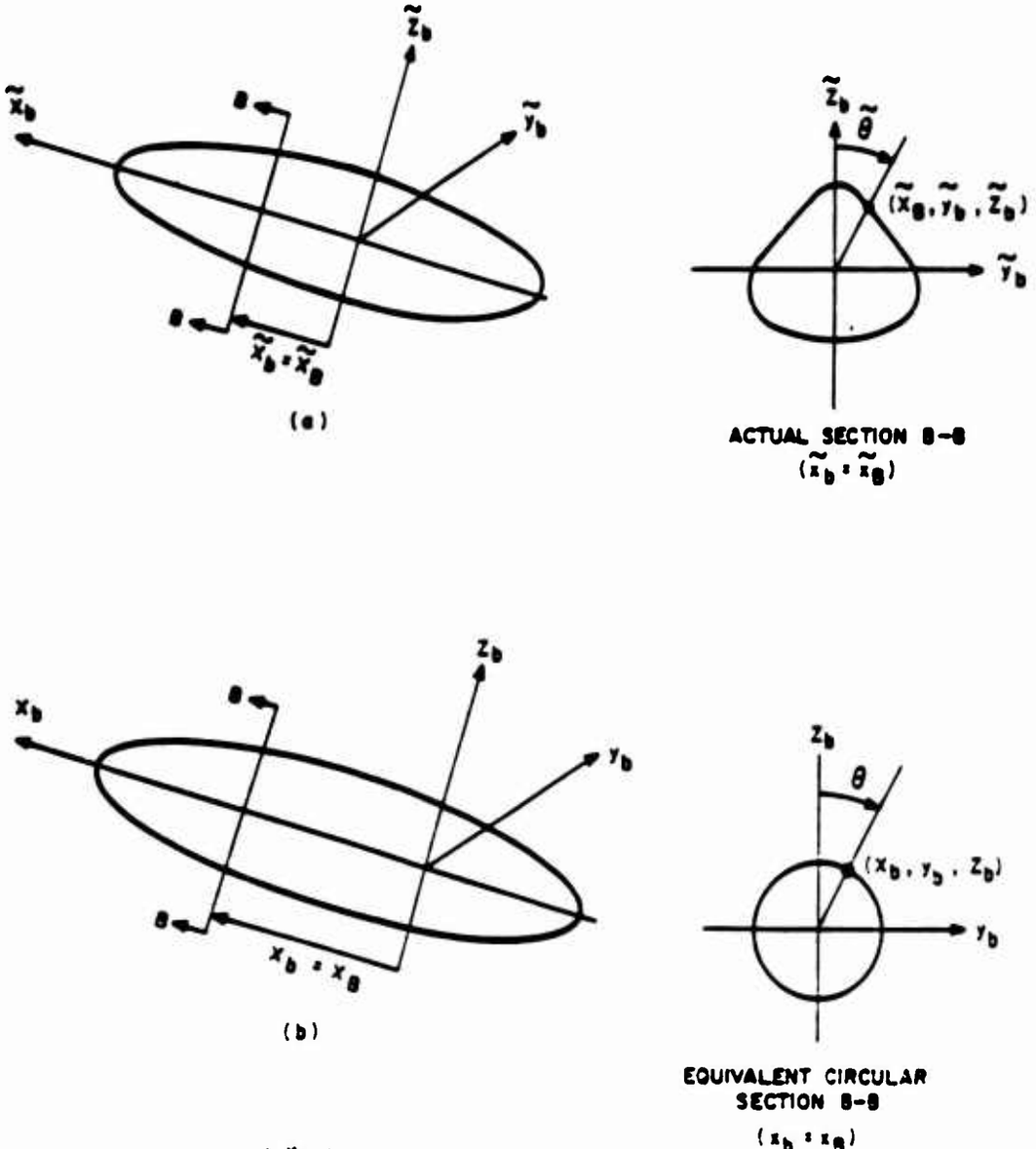

Figure 19. Actual and Equivalent Body

This implies that the points which have the same slope of the contour in the plane section B-B are related.

Scheme (b) was chosen, since it results in the proper inclination to the relative flow. Selection of the point $(\tilde{x}_b, \tilde{y}_b, \tilde{z}_b)$ where the pressure versus time is desired permits unique determination of the related point (x_b, y_b, z_b) on the equivalent body where the pressures will be obtained.

The replacement of the actual body by a body of revolution represents a very substantial simplification. If the direction of the blast is arbitrary, the blast will produce an incremental angle of yaw (α_ψ) in addition to an incremental angle of attack. However, these two can be combined with the initial angle of attack (α_o) in the preblast pitch plane $(z_b - x_b)$ to form a single angle of attack in a plane different from the pitch or yaw plane.

Consider the equivalent body and the cross section for a point (x_{2b}, y_{2b}, z_{2b}) where the pressure is desired, as shown in figure 20. Note that the body-coordinate system is left-handed with the origin at any point on the x_b-axis of the body.

The objective is to find the pressure at point (x_{2b}, y_{2b}, z_{2b}) before and after the blast encounter. The pressure-time history will be assumed to vary in the fashion shown in figure 21. This is similar to the pressure-time history presented by Norris and Hansen (ref. 22) for stationary cylinders encountering blasts.

The pressure variation spans the following three time ranges of interest:

(a) Period prior to blast arrival, $t \leq t_a$ where t_a denotes the time of shock arrival at (x_{2b}, y_{2b}, z_{2b})

(b) The diffraction period, $t_a < t < t_d$, where $t_d = t_c + t_a$ denotes the time when the flow returns to essentially

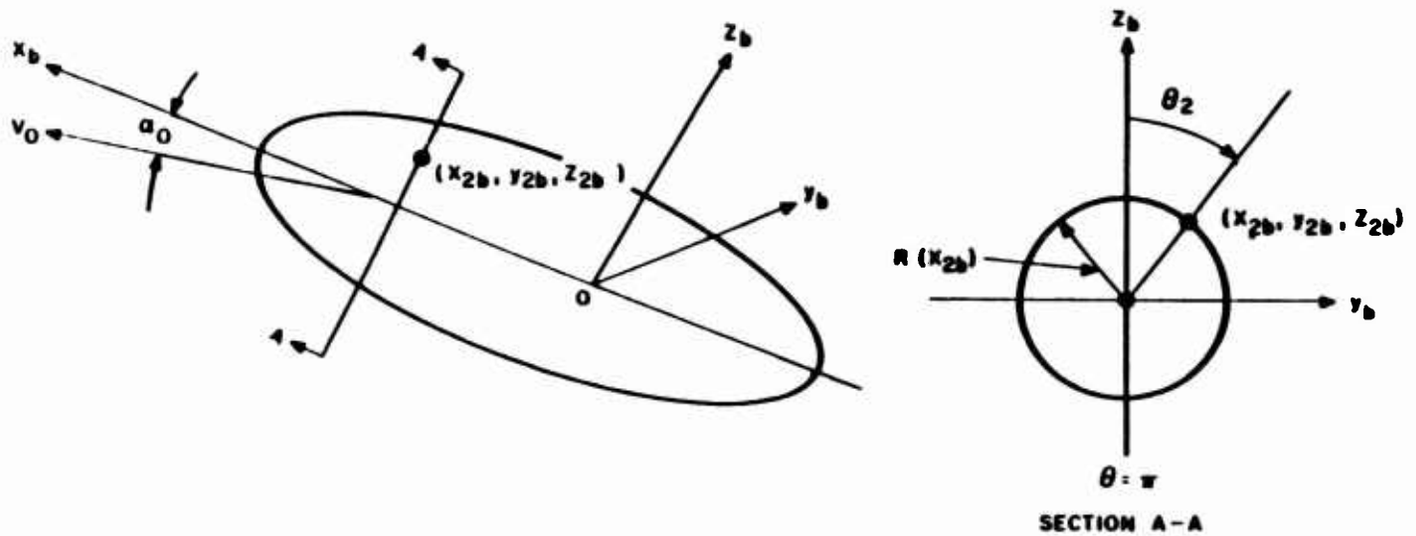

NOTE · α_0 IS ANGLE OF ATTACK IN THE $(z_b - x_b)$ - PLANE

Figure 20. Coordinate Systems and Notations on the Equivalent Body

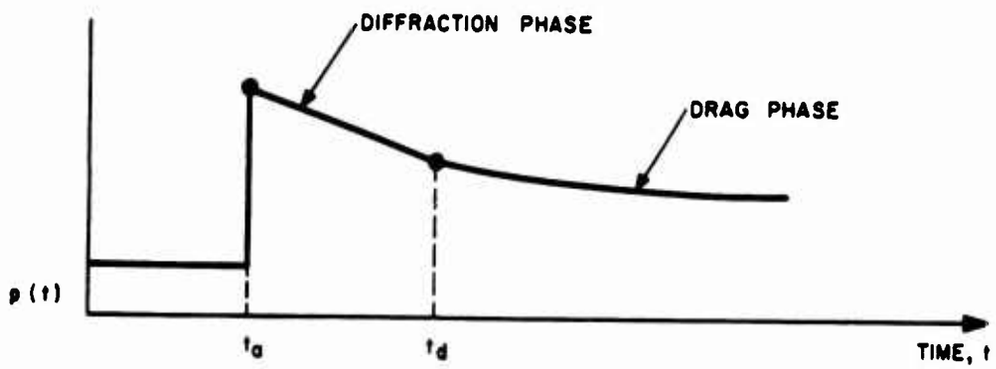

Figure 21. Assumed Timewise Pressure Variation

"steady-state" conditions following blast encounter and t_c is the clearing time. An abrupt increase in pressure may occur at time t_a^+ (or $t_a + \varepsilon$, $\varepsilon \to 0$).

(c) The post-diffraction phase or the drag phase, $t \geq t_d$.

Range (a) is truly a steady-state period. Range (c) can be treated as steady-state based on instantaneous free-stream conditions dictated by blast conditions at the point in question. To construct pressure versus time plots like that of figure 21, the following problems need to be resolved:

1. Determination of the steady-state pressure at the point of interest based on preblast conditions.
2. The shock arrival time, t_a, for the point of interest.
3. The length of the diffractive period t_c.
4. The pressure at time t_a^+, $p(t_a^+)$.
5. The pressure at time t_d, $p(t_d)$, based on instantaneous "gust" and "free-stream" conditions at t_d.
6. Pressures during the diffractive period, assuming <u>linear</u> variation with time between pressures $p(t_a^+)$ and $p(t_d)$.
7. Pressures at selected times $t > t_d$, $p(t)$, based on instantaneous "gust" and "free-stream" conditions at t.

Each of these will now be discussed individually. First, however, some preparatory work is needed. Divide the body into three parts, as shown in figure 22. The definitions are arbitrarily made so that x_d is the station at which $(dR/dx_b) = -0.15$ and x_g is the station at which $(dR/dx_b) = 0.15$, where R is the radius. Pressures on Part (c) are not expected to be large, especially for large forward speeds, V_o; therefore, Part (c) can be treated in a very approximate fashion as a portion of Part (b) with $(dR/dx_b) > 0$.

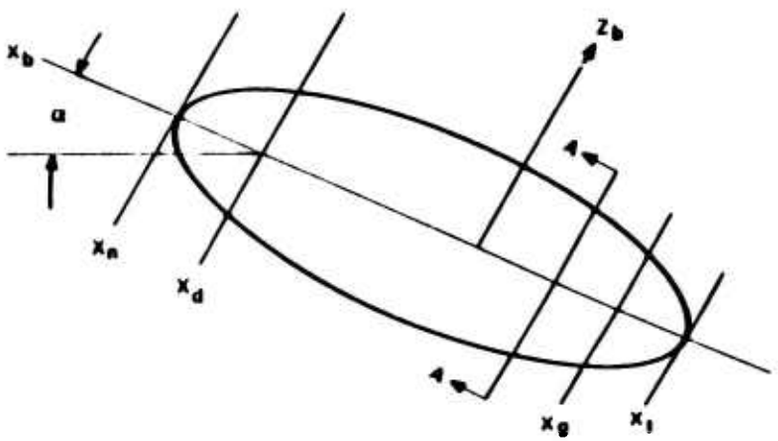

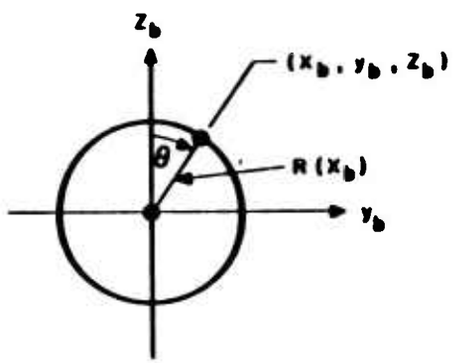

SECTION A-A

PART (a): $x_d < x_b \leq x_n$ BLUNT NOSE SECTION

PART (b): $x_g \leq x_b \leq x_d$ "QUASI-CYLINDRICAL" SECTION

PART (c): $x_t \leq x_b < x_g$ TAIL SECTION

Figure 22. Definition of Parts of Equivalent Body

The steady-state pressure coefficient (C_p), due to angle of attack for the quasi-cylindrical section, is a function of position (x_b and θ) and angle of attack (α)* according to slender-body theory.

$$C_p\ (x_b,\theta,\alpha) = \begin{cases} 4\alpha\cos^2\alpha\ \dfrac{dR}{dx_b}\cos\theta + a(A)\ \sin^2\alpha\ \dfrac{dR}{dx_b} & \leq 0 \\ \\ a(A)\ \sin^2\alpha & \dfrac{dR}{dx_b} > 0 \end{cases} \tag{31}$$

$$A = \begin{cases} \pi - |\theta| & \alpha \geq 0 \\ \\ |\theta| & \alpha < 0 \end{cases} \tag{32}$$

$$a(A) = \begin{cases} 1-4\sin^2 A & 0 \leq A \leq \pi/2 \\ -10.278 + 4.6333A & \pi/2 < A < 2\pi/3 \\ -0.574 & 2\pi/3 \leq A \leq \pi \end{cases} . \tag{33}$$

The term $4\alpha\cos^2\alpha(dR/dx_b)\cos\theta$ comes from slender-body theory (see Liepmann and Roshko, reference 25, page 245, with α^2 omitted and $\alpha\cos^2\alpha$ added to reduce the total dynamic pressure to dynamic pressure based on axial velocity. The added $\cos^2\alpha$ factor also reduces the (dR/dx_b) contribution for large angles of attack. The $a(A)\sin^2\alpha$

*The angle of attack is defined as the angle between the negative of the relative wind and the body axis x_b.

term gives the cross-flow drag in accordance with Allen and Perkins (reference 26). The constants in the formulas for the circumferential pressure variation, a(A), are chosen so that the circumferential pressure variations result in a value of 0.35 for the sectional coefficient, C_d, a reasonable value for supercritical Reynolds numbers. The circumferential pressure variation, shown in figure 23, matches a typical pressure variation along the periphery of a cylinder engulfed in a supercritical Reynolds number flow.

Equations (31) describe the steady-state pressure coefficient for the quasi-cylindrical and tail sections of the body, but are not appropriate for the blunt nose section. The nose section pressures will be approximated by using the pressure coefficient at $x_b = x_n$, which will be taken as the stagnation point. This pressure coefficient is a function of Mach number, M, only, and will be denoted by C_{p_o}.

$$C_{p_o}(M) = \begin{cases} \dfrac{(1+M^2/5)^{7/2}-1}{0.7M^2} & M \leq 1 \\ \dfrac{\left(\dfrac{6M^2}{5}\right)^{7/2}\left(\dfrac{6}{7M^2-1}\right)^{5/2}-1}{0.7M^2} & M \geq 1 \end{cases} \tag{34}$$

Consider now the seven problems listed earlier. The first is that of determining the preblast pressure. For the quasi-cylindrical and tail sections, C_p $(t \leq t_a)$ is given by equation (31), using the preblast angle of attack.

The determination of the pressure coefficient for the nose section is more complicated. At the nose point, which is the stagnation point for $\alpha = 0$, C_{p_o} is applicable exactly at $\alpha = 0$, and approximately if α

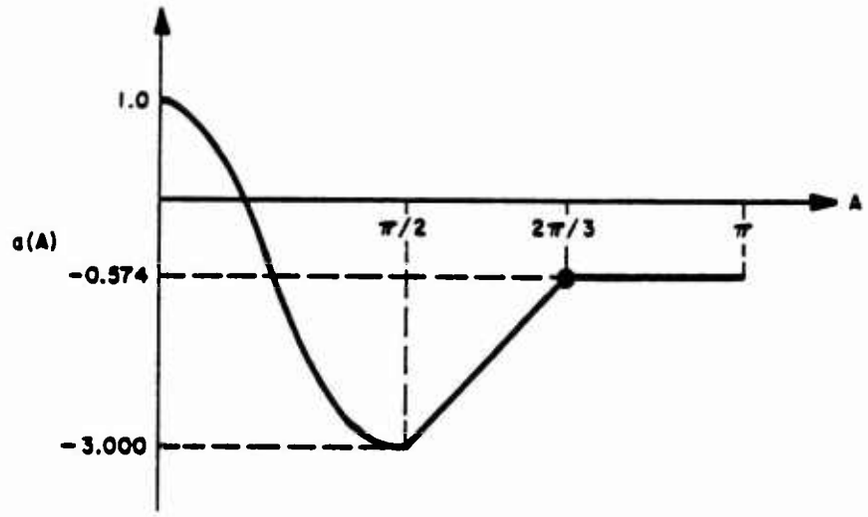

Figure 23. Circumferential Pressure Variation, a(A)

is finite. The pressure coefficient for a quasi-cylindrical section, $C_p(x_d,\theta,\alpha)$, is defined by equation (31) where θ is the same as that for point (x_b, y_b, z_b).

By definition, $\left(\frac{dR}{dx_b}\right)_{x_d} = -0.15$. Let

$$\delta = \tan^{-1}\left(-\frac{dR}{dx_b}\right)_{x_b} \tag{35}$$

$$\delta_d = \tan^{-1}\left(-\frac{dR}{dx_b}\right)_{x_d} = \tan^{-1}(0.15) \tag{36}$$

The transition from the stagnation point pressure coefficient to the pressure coefficient at x_d for $t < t_a$ can be represented by

$$C_p(x_b>x_d,\theta,\alpha) = [C_{p_o} - C_p(x_d,\theta,\alpha)]\left(\frac{\sin\delta - \sin\delta_d}{1-\sin\delta_d}\right)^2 + C_p(x_d,\theta,\alpha) \tag{37}$$

The form of equation (37) is patterned after the pressure distribution given by Newtonian flow, that is, proportional to $\sin^2\delta$. The variation in pressure coefficient given by equation (37) roughly approximates this distribution because C_{p_o} is substantially larger than C_p, and $\sin\delta_d$ is small in comparison with unity.

The pressure coefficients defined above are used to obtain the pressure in accordance with the equation

$$p = p_\infty + q_\infty C_p \tag{38}$$

where p_∞ and q_∞ are the free-stream pressure and dynamic pressure. Equation (38) is appropriate for transforming the pressure coefficient into pressure for both preblast and blast conditions, provided that p_∞ and q_∞ describe the local ambient conditions in front of or at some point behind the shock, as appropriate. One note of caution is required in applying equation (38): The pressure calculated by equation (38) may be negative, which is, of course, a physical impossibility. If this happens, the pressure should be set equal to zero.

Next, the determination of the time of shock arrival, t_a, and the clearing time, t_c, must be considered. The blast characteristics routine used in the NOVA program returns the shock position for a given time. It is a simple matter, then to proceed in small timewise steps, calculating the position of the desired point on the body relative to the burst point at each step, and comparing this with the shock position at the time associated with that step. In this way, the time of arrival, t_a, can be identified as closely as desired.

Similarly, the time at which the shock first touches the fuselage can be identified. The time at which the fuselage is intercepted t_i, is needed to define the clearing time, t_c. Determination of t_i is somewhat more cumbersome than the determination of t_a, because a number of points on the fuselage must be considered to identify the time at which the shock first intercepts the fuselage. Basically, however, t_i is determined in the same way as t_a.

The clearing time t_c is an artificial parameter which has been devised to present the actual pressure versus time in the approximate fashion of figure 21. It may be thought of as a rough measure of the time required for the flow to return to essentially quasi-steady conditions following shock arrival. Attempts to define t_c experimentally are rather limited and are confined primarily to tests on stationary cylinders (e.g., reference 27).

There is some degree of arbitrariness in defining t_c because (a) the diffractive pressure variations are not generally linear, and (b) the start of the quasi-steady period may be very difficult to determine. Both of these points are strongly influenced by the location of the point, the shape of the body, and the shock orientation and strength. In what follows, then, an attempt is made to give a definition of t_c which will result in reasonable representations of the diffractive phase pressures. There is obviously no single approach which could handle accurately all possible cases that may arise.

To begin with, consider the case of a wedge flying supersonically prior to a head-on blast encounter. During the blast traversal, the shock pattern has been noted to be such that a region behind the shock of approximately $a_{bs}(t-t_i)$ in width (a_{bs} = speed of sound behind the blast shock) is still in a diffractive phase (ref. 28). Figure 2- illustrates this point. Thus, one may consider for the above situation that a "diffraction wave" starts traveling back from the shock wave at time t_i. This wave travels at the speed of sound, a_{bs}, relative to the shock. At some time $t > t_i$, then, the diffraction wave is at a distance $a_{bs}(t-t_i)$ behind the shock. Since the position of the diffraction wave can be referenced to the position of the shock front, the procedure described above can be used to determine the time at which the diffraction wave reaches the desired point, t_d. The clearing time, t_c, is then simply the difference between t_d and t_a.

If this analytical definition for t_c is adopted for bodies flying at different speeds, and encountering blasts from arbitrary orientations, some problems arise. First consider the case of a cylinder which is intercepted side-on by a shock wave. The above definition of t_c results in a clearing time of zero for the extreme windward points, since t_i and t_a are identical for such points, and therefore, the diffraction wave also arrives at t_a ($t_d = t_a$). Tests on scaled missile models in the DASACON shock tube (ref. 27) however, indicate that a

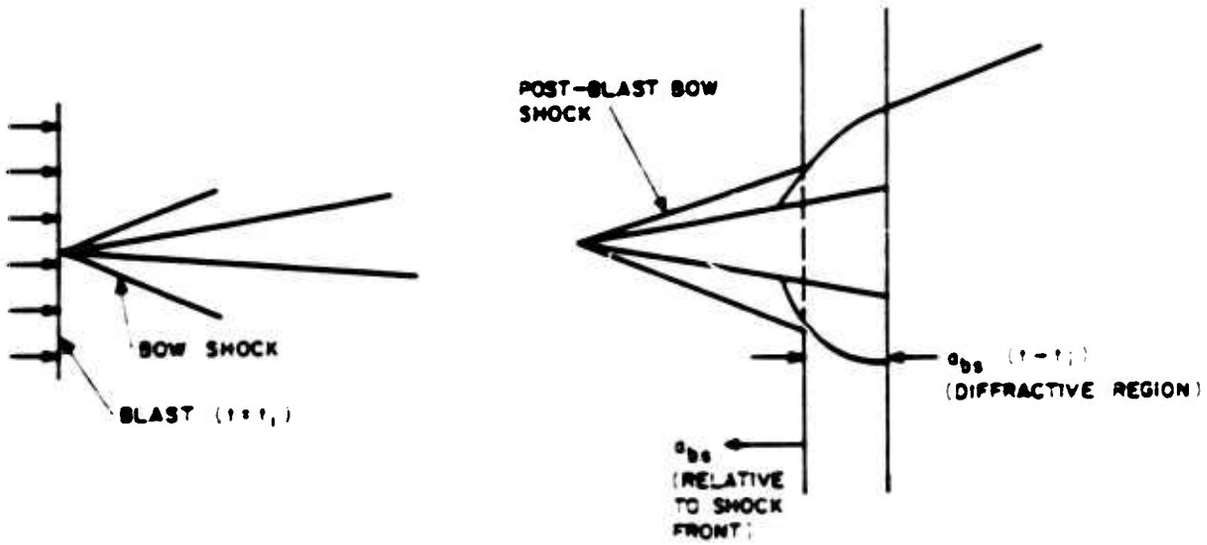

Figure 24. Sketch of Shock Pattern of a Head-On Blast Intercept over a Supersonic Airfoil

clearing time of about $(2R/a_{bs})$ is appropriate, particularly for points on the windward side which experience the highest pressures. Accordingly, the adopted procedure is to determine t_c as described earlier, and to use the larger of that value or $(2R/a_{bs})$.

The second problem which arises may be illustrated by the case when the blast arrives directly from the back and the vehicle velocity nears the value $V_s - a_{bs}$, where V_s is the velocity of the shock front. For such cases, the clearing time (t_c), as defined above, becomes unrealistically high. No experimental results are available to establish an upper limit on t_c in a manner such as that used to establish the lower limit. The value of $(6R/a_{bs})$ has arbitrarily been chosen as the upper limit of t_c in the program.

To determine the pressure at time t_a^+, it is necessary to define the orientation of the shock front relative to the fuselage local surface normal. When t_a is determined, as described previously, the shock orientation in space is automatically available. The unit vector normal to the shock, in the direction of shock propagation, will be designated by $\bar{n}_s$. The unit vector normal to the body and directed inward is given by

$$\bar{n}_b = \left(\bar{i}_b \frac{dR}{dx_b} - \bar{j}_b \sin\theta - \bar{k}_b \cos\theta\right) \frac{1}{\sqrt{1 + \left(\frac{dR}{dx_b}\right)^2}} \qquad (39)$$

where $\bar{i}_b$, $\bar{j}_b$, and $\bar{k}_b$ are the unit vectors in the x_b, y_b, and z_b directions, respectively. Defining a new coordinate system, x, y, z, which is related to the x_b, y_b, z_b system by a rotation $-\alpha_o$ about the y_b axis, so that the x axis is horizontal,

$$\bar{n}_b = \left| \bar{i} \left(\frac{dR}{dx_b} \cos\alpha_o + \cos\theta \sin\alpha_o \right) - \bar{j} \sin\theta \right.$$

$$\left. + \bar{k} \left(\frac{dR}{dx_b} \sin\alpha_o - \cos\theta \cos\alpha_o \right) \right| \frac{1}{\sqrt{1 + \left(\frac{dR}{dx_b} \right)^2}} \qquad (40)$$

where $\bar{i}$, $\bar{j}$, and $\bar{k}$ are the unit vectors in the x, y, and z directions, respectively.

If the components of $\bar{n}_s$ (the unit vector normal to the shock in the direction of shock-front propagation) in the x, y, z directions are n_x, n_y, n_z, respectively, then the shock plane and the plane tangent to the fuselage body make an angle

$$\theta_{sb} = \cos^{-1}(\bar{n}_b \cdot \bar{n}_s)$$

$$= \cos^{-1} \left\{ \frac{1}{\sqrt{1 + \frac{dR}{dx_b}^2}} \left| n_x \left(\frac{dR}{dx_b} \cos\alpha_o + \cos\theta \sin\alpha_o \right) \right. \right.$$

$$\left. \left. - n_y \sin\theta + n_z \left(\frac{dR}{dx_b} \sin\alpha_o - \cos\theta \cos\alpha_o \right) \right| \right\}, \quad 0 \leq \theta_{sb} \leq \pi$$

(41)

If the vehicle has no component of its velocity V_o normal to the surface, then the theory of plane shock reflection from a stationary plane surface can be used. This would be nearly true for regions where dR/dx_b is small, i.e., in quasi-cylindrical portions. For high $|dR/dx_b|$ regions, i.e., the nose section, this would not be strictly applicable. In fact, with "blunt" bodies in supersonic flow, there is a shock-shock interaction problem which is not easily included.

In the absence of a better practical procedure for such regions, the reflection theory of a plane shock on a plane stationary wall will be used. Norris and Hansen (ref. 22) give $\Delta p/\Delta p_s$ as a function of θ_{sb}, where Δp is the incremental pressure on the body and Δp_s is the shock overpressure. $\Delta p/\Delta p_s$ versus θ_{sb} is dependent on the pressure ratio across the shock. The curves of $\Delta p/\Delta p_s$ versus θ_{sb} exhibit bumps in the neighborhood of transition from a regular reflection to a Mach reflection. These bumps have not been observed experimentally on circular cylinders. Rather than use the curves in Norris and Hansen directly, the approximation depicted in figure 25 is used. The curve shows constant $\Delta p/\Delta p_s$ for $0 \leq \theta_{sb} \leq \pi/4$, and linear variations of $\Delta p/\Delta p_s$ with θ_{sb} between $\pi/4$ and $\pi/2$, and between $\pi/2$ and π.

In figure 25, the parameter $\bar{r}_p$ is the reflection factor for normal incidence, and is given by

$$\bar{r}_p = 2\,\frac{p_\infty + 4/7\ \Delta p_s}{p_\infty + 1/7\ \Delta p_s} \tag{42}$$

Thus, referring to figure 25,

$$\frac{\Delta p}{\Delta p_s} = \begin{cases} \bar{r}_p & 0 \leq \theta_{sb} \leq \pi/4 \\ \bar{r}_p + (1 - \bar{r}_p)\left(\dfrac{\theta_{sb} - \pi/4}{\pi/4}\right) & \dfrac{\pi}{4} < \theta_{sb} \leq \pi/2 \\ 1.5 - \dfrac{\theta_{sb}}{\pi} & \dfrac{\pi}{2} < \theta_{sb} \leq \pi \end{cases} \tag{43}$$

The pressure at t_a^+ is then determined from

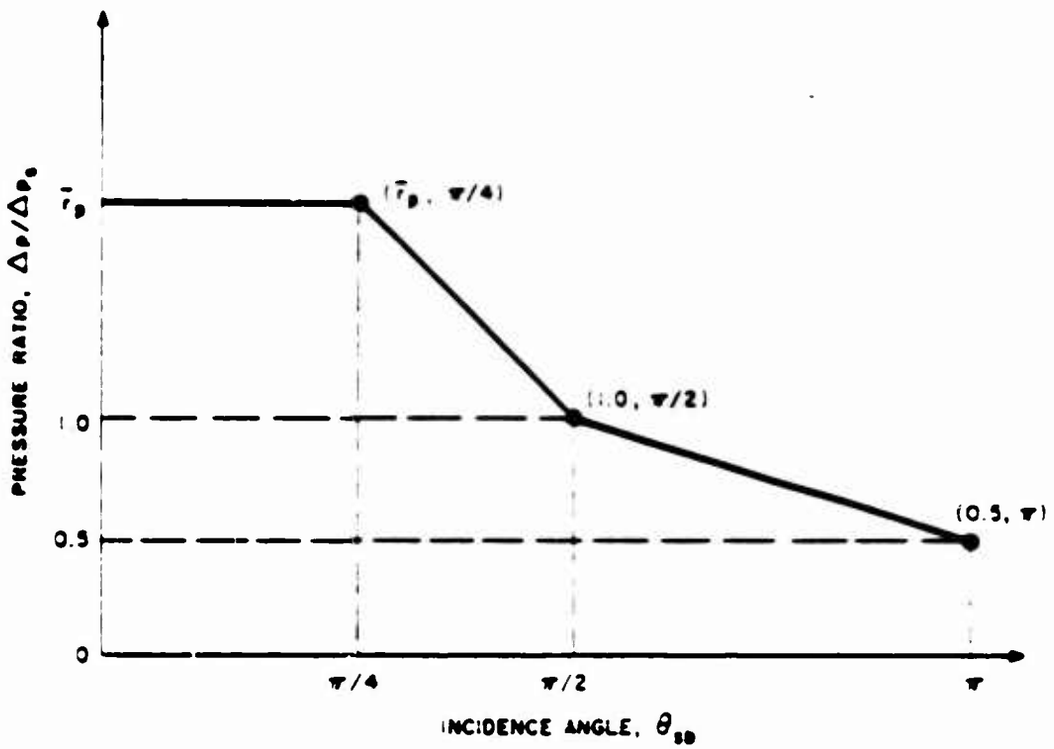

Figure 25. Variation of Reflection Factor with Incidence Angle

$$p(t_a^+) = p(t_a^-) + \left(\frac{\Delta p}{\Delta p_s}\right) \Delta p_s \tag{44}$$

where $p(t_a^-)$ is the pressure just before shock arrival, or the original steady-state pressure from equations (31) through (38).

Next, consider the pressure at the end of the diffraction period, $p(t_j)$. From the blast routines and the range and orientation of the point in question relative to the burst point, the ambient density, $\rho_\infty(t_d)$, pressure, $p_\infty(t_d)$, and material velocity components, $w_x(t_d)$, $w_y(t_d)$, and $w_z(t_d)$, are known. The x, y, z coordinate system is that described in connection with equation (40). The total velocity is, then,

$$V_T(t_d) = \sqrt{[V_o - w_x(t_d)]^2 + [w_y(t_d)]^2 + [w_z(t_d)]^2} \tag{45}$$

To find the angle of attack of the section containing the point in question, the total velocity <u>of the air relative to the body</u> is resolved into components in the x_b, y_b, z_b, body coordinate system.

$$V_{T_{x_b}} = -(V_o - w_x)\cos\alpha_o + w_z \sin\alpha_o \tag{46}$$

$$V_{T_{y_b}} = w_y \tag{47}$$

$$V_{T_{z_b}} = (V_o - w_x)\sin\alpha_o + w_z \cos\alpha_o \tag{48}$$

The flow is then inclined at an angle γ from the z_b axis, where

$$\gamma = \tan^{-1} \frac{V_{T_{y_b}}}{V_{T_{z_b}}} \qquad -\pi/2 \leq \gamma \leq \pi/2 \tag{49}$$

An effective θ may be defined as the angle between the flow and the point in question. Calling this angle $\bar{\theta}$,

$$\bar{\theta} \equiv \theta - \gamma \tag{50}$$

To maintain $\bar{\theta}$ in the interval $-\pi \rightarrow \pi$, if $\bar{\theta} > \pi$, subtract 2π, and if $\bar{\theta} < -\pi$, add 2π. Finally, the angle of attack is given by

$$\alpha = \tan^{-1} \left[\frac{V_{T_{y_b}} \sin\gamma + V_{T_{z_b}} \cos\gamma}{-V_{T_{x_b}}} \right] \qquad -\pi/2 \leq \alpha \leq \pi/2 \tag{51}$$

Equations (31) through (38) are used with $\bar{\theta}$ replacing θ to find $p(t_d)$. Note that, if a nose point is involved, there is an implicit assumption that $V_{T_{x_b}} < 0$. Also, for a nose point, the flow parameters to be employed for the stagnation point, including the Mach number in equation (31), and for $x_b = x_d$, are those corresponding to the point in question.

Pressures during the diffraction period are found by linear interpolation.

$$p(t) = p(t_a^+) + \frac{t-t_a}{t_c} \left\{ p(t_d) - p(t_a^+) \right\} \qquad t_a < t \leq t_d \tag{52}$$

For times greater than t_d, the pressure at a point is found in precisely the same way as $p(t_d)$; that is, equations (45) through (51) are used, with $t > t_d$ replacing t_d, and the parameters so defined are used with equations (31) through (38) to obtain the pressure.

The foregoing procedures serve to define completely the pressure-time history for a point on a fuselage with a straight centerline, due to a single shock. Modifications necessary to accommodate a nonstraight centerline and a double shock will now be described.

The computer program permits the centerline of the fuselage to be described by two straight lines, as shown in figure 26. The bend occurs at $x_b = x_{BF}$, which is assumed to be aft of the transition point from the nose section to the quasi-cylindrical section, x_d. All of the preceding procedures remain valid, as long as the initial angle of attack is defined by

$$\alpha_o = \begin{cases} \alpha_{o_F} & x_b > x_{BF} \\ \alpha_{o_F} - \beta & x_b < x_{BF} \end{cases} \qquad (53)$$

If the aircraft is intercepted by the blast wave at a point just above the triple point, a second shock will follow closely behind the first. The pressure-time history for this case is shown in figure 27. Subscripts 1 and 2 are used to identify the first and second shocks, respectively. Prior to the time t_{a_2}, the pressure is, of course, given by the procedures already described. The jump in pressure at time t_{a_2} is $(\Delta p/\Delta p_{s_2})\,\Delta p_{s_2}$. The shock overpressure Δp_{s_2}, for the second shock is obtained from the blast routine and $(\Delta p/\Delta p_{s_2})$ is obtained from

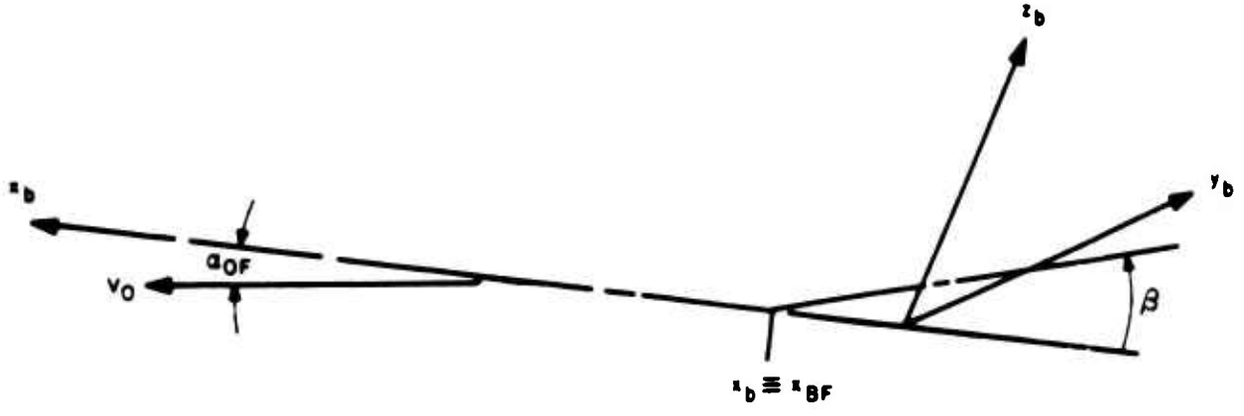

Figure 26. Geometry of Fuselage with Bent Centerline

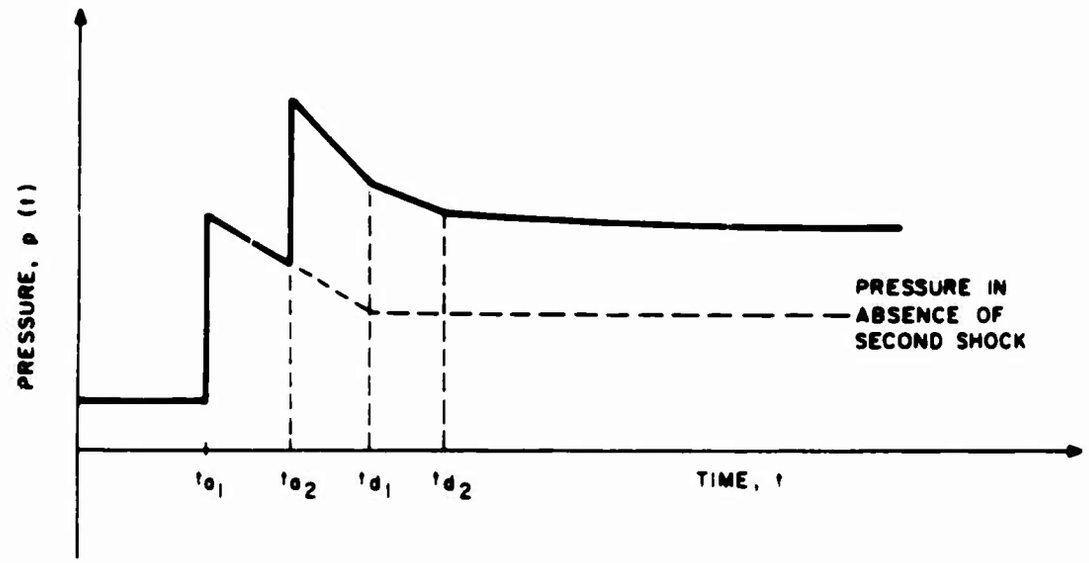

(a) $t_{a_2} < t_{d_1}$ SECOND SHOCK ARRIVES BEFORE DIFFRACTION OF FIRST WAVE IS COMPLETE

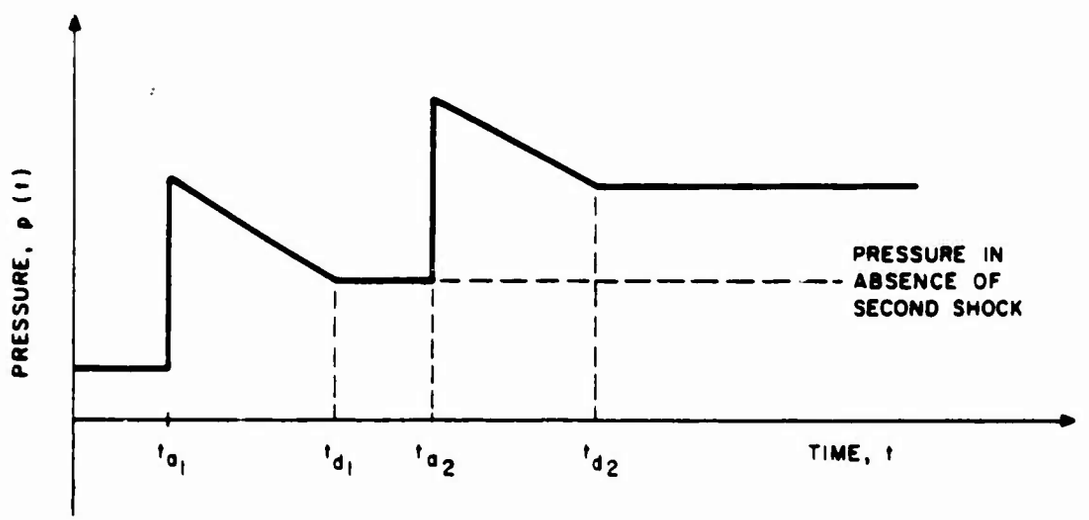

(b) $t_{a_2} \geq t_{d_1}$ SECOND SHOCK ARRIVES AFTER DIFFRACTION OF FIRST WAVE IS COMPLETE

Figure 27 - Pressure-Time History for Double Shock

equations (42) and (43) using the ambient pressure corresponding to time $t_{a_2}^-$ for p_∞. The pressures at t_{d_2} and later are given by procedures already described, using flow parameters from the blast routine for the doubly shocked air. The only remaining point requiring definition is $p(t_{d_1})$ for $t_{a_2} < t_{d_1}$.

$$p(t_{d_1}) = p_1(t_{d_1}) + (p(t_{a_2}^+) - p(t_{a_2}^-)) - \frac{t_{d_1} - t_{a_2}}{t_{d_2} - t_{a_2}} \left[(p(t_{a_2}^+) - p(t_{a_2}^-)) - (p(t_{d_2}) - p_1(t_{d_2})) \right] \quad t_{a_2} < t_{d_1} \qquad (54)$$

The quantity $p_1(t_{d_1})$ in equation (54) is the pressure that would exist at time t_{d_1} in the absence of the second shock and $p_1(t_{d_2})$ is to be interpreted similarly. Linear variations in pressure are assumed from t_{a_2} to t_{d_1} and from t_{d_1} to t_{d_2}.

SECTION IV
STRUCTURAL RESPONSE TECHNIQUES

The structural elements of an aircraft vehicle susceptible to overpressure damage consist of the following:

1. Stringers on the fuselage or on lifting surfaces
2. Longerons or frames on the fuselage
3. Single-layered or honeycomb panels on the fuselage or on lifting surfaces
4. Acrylic, glass, or plexiglass canopies
5. Multilayered radomes
6. Rib webs on lifting surfaces

Two structural response codes were developed for predicting the elastic and inelastic response of these structural elements to the overpressure loading associated with the blast wave. The first of these response codes is called DEPROB for Dynamic Elastic Plastic Response of Beams and was developed for use with stringers, longerons, frames, ribs, and also for conical or cylindrical shaped radomes which may be represented by a ring. The second of these response codes is called DEPROP for Dynamic Elastic Plastic Response of Panels and was developed for use with single-layered and honeycomb panels, canopies, and certain radomes.

Provision is made in each code to determine the static preblast solution due to internal pressurization and aerodynamic loads on the structural element. This steady-state solution then provides the initial conditions for the dynamic response associated with a time-dependent blast wave. The formulation for each of the two response codes is described in detail in the remainder of this section.

4.1 DYNAMIC ELASTIC-PLASTIC RESPONSE OF BEAMS - DEPROB

The structural response program DEPROB calculates the static and dynamic, elastic or elastic-plastic, response of aircraft elements which can be modeled as beam or ring elements. These elements can have arbitrary spanwise shape, can have arbitrary cross section involving different materials and varying spanwise along the beam, can have any combination of boundary conditions -- clamped, simply supported, or free-- and can respond to a transient pressure function which varies with both time and spanwise position.

The basis for the code is a finite-difference method developed by MIT (refs. 29 and 30) to predict the deformations of a circular ring to impulsive and transient loadings. DEPROB represents considerable modification and extension of the capabilities of that original effort. The remainder of this section will describe in detail the DEPROB code. As partial verification, the final portion presents comparisons of the dynamic response of two clamped beams tested experimentally and analyzed by DEPROB and by the MIT code.

4.1.1 Basic Theory

The finite difference technique applied to two-dimensional structures in DEPROB assumes a spanwise model consisting of a series of discrete masses interconnected by straight, weightless bars, as indicated in figure 28. Beams with variable geometrical cross section in the spanwise direction are reduced to a series of links, each completely uniform. Each bar and mass then has its own material properties. Beam response to externally applied forces is computed at each mass point.

The actual cross section is idealized by introducing a set of discrete points called flanges. These flanges have normal stress distributions, and are interconnected by material of infinite shear rigidity as indicated in figure 29. Flange elongations are governed by the Bernoulli assumption that plane sections remain plane.

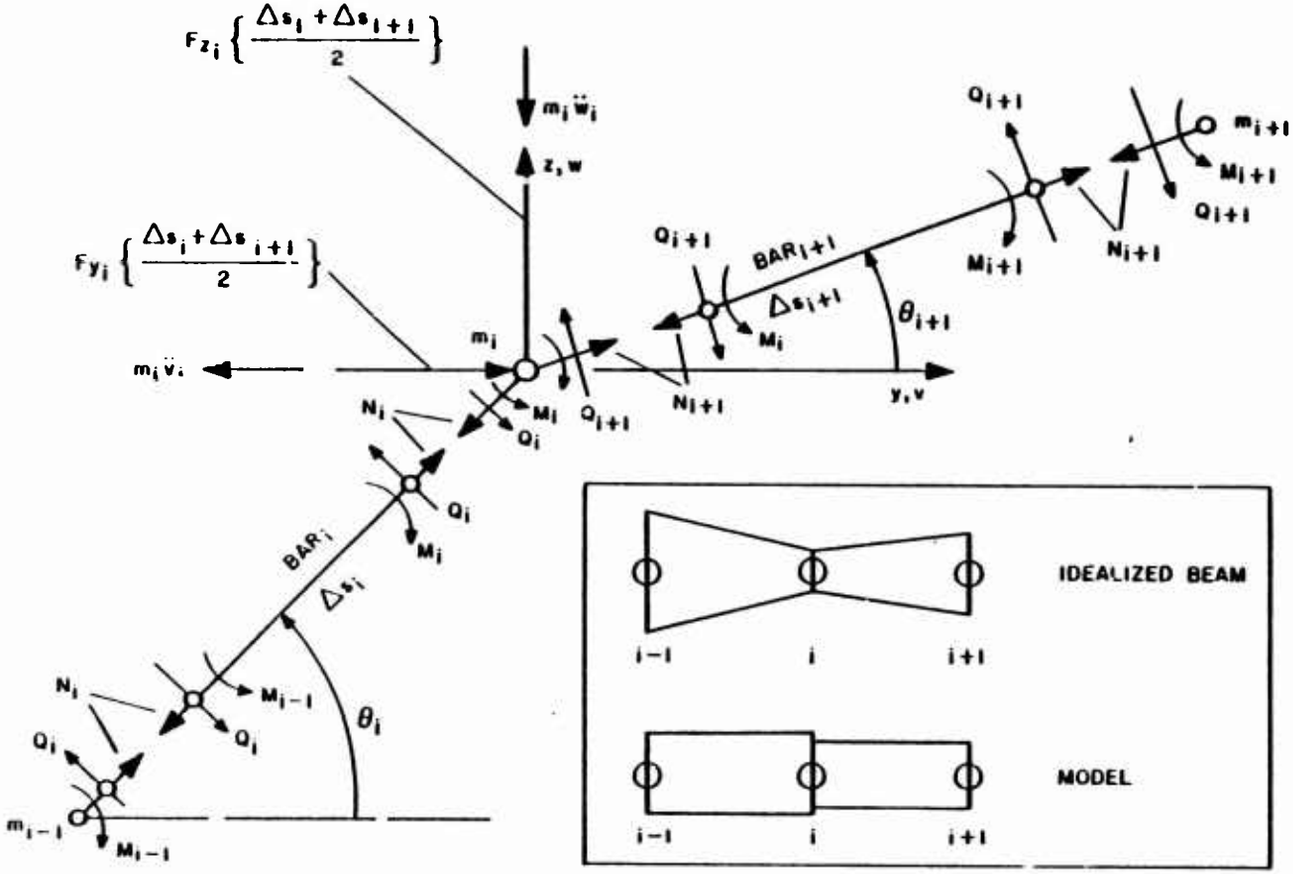

Figure 28. Bar-Mass Representation of a Beam

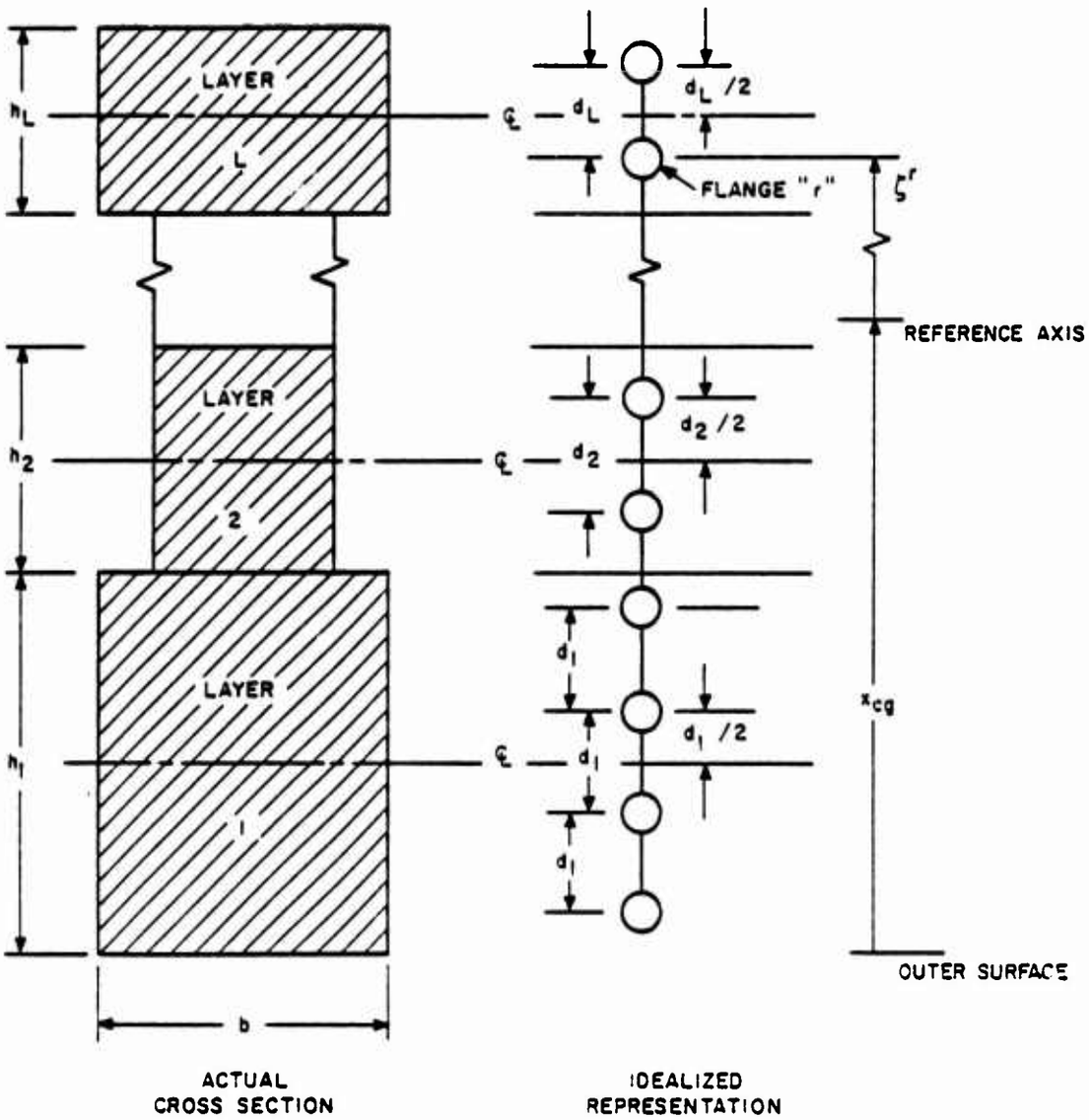

Figure 29. Actual Cross Section and an Idealized Representation

The stress-strain curve of each layer of material is modeled by a series of straight lines, as shown in figure 30. Enough straight line segments will, in the limit, describe any curve. The curves may differ in tension or compression, except for the elastic slopes (segment 1), which must be the same. However, the yield stress, defined as the break point stress at the end of the first segment, may differ in tension and compression.

A more complete description of the theoretical development of DEPROB is now presented in subsections 4.1.2 to 4.1.11.

4.1.2 Equations of Motion

The governing equations of dynamic equilibrium take the form

$$\frac{\partial}{\partial s} (N \cos \theta) - \frac{\partial}{\partial s} (Q \sin \theta) + F_y - m\ddot{v} = 0$$

$$\frac{\partial}{\partial s} (N \sin \theta) + \frac{\partial}{\partial s} (Q \cos \theta) + F_z - m\ddot{w} = 0$$

and, ignoring rotary inertia,

$$\frac{\partial M}{\partial s} - Q = 0$$

Referring to figure 28, the corresponding finite difference equations are, for the ith mass point,

$$N_{i+1}\cos\theta_{i+1} - N_i\cos\theta_i - Q_{i+1}\sin\theta_{i+1} + Q_i\sin\theta_i + F_{y_i}\left(\frac{\Delta s_i + \Delta s_{i+1}}{2}\right) - m_i\ddot{v}_i = 0 \qquad (55)$$

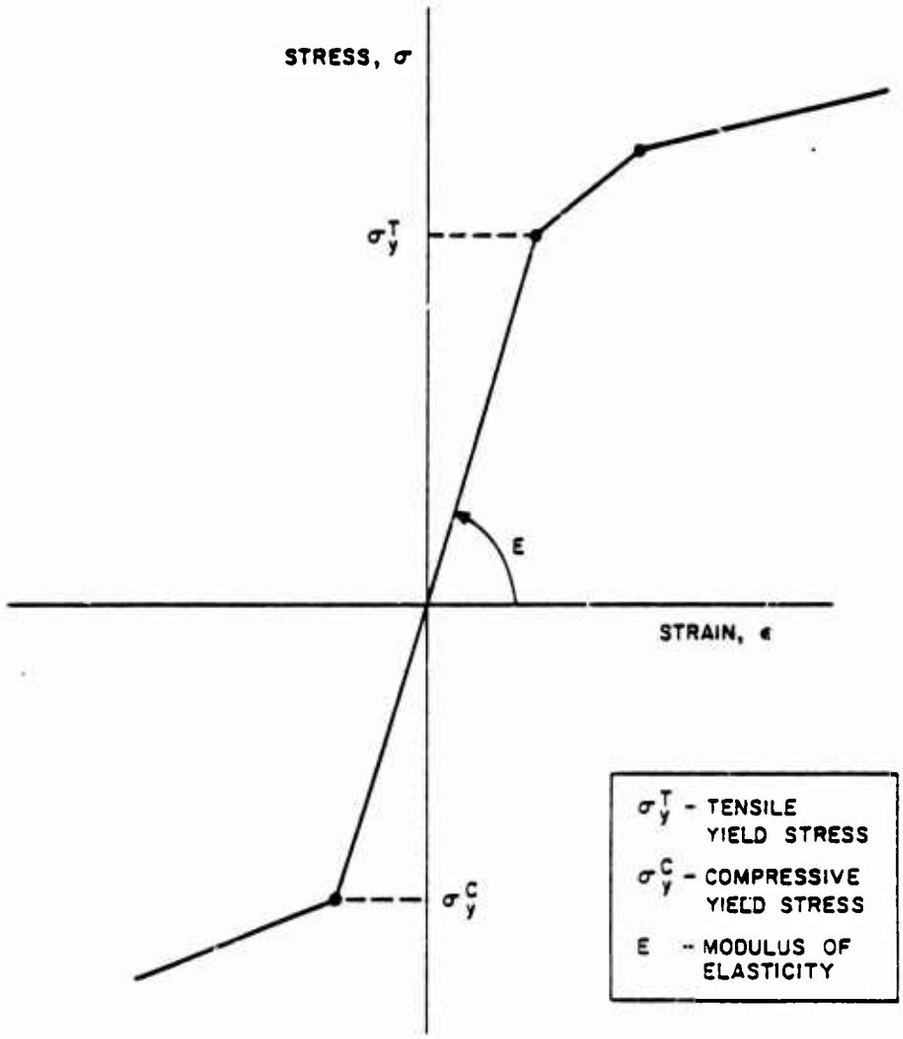

Figure 30. Idealized Stress-Strain Curve

$$N_{i+1}\sin\theta_{i+1} - N_i \sin\theta_i + Q_{i+1}\cos\theta_{i+1}$$

$$-Q_i\cos\theta_i + F_{z_i}\left(\frac{\Delta s_i + \Delta s_{i+1}}{2}\right) - m_i \ddot{w}_i = 0 \qquad (56)$$

$$M_i - M_{i-1} - Q_i\,\Delta s_i = 0 \qquad (57)$$

where, from geometrical considerations,

$$\Delta s_i = [(v_i - v_{i-1})^2 + (w_i - w_{i-1})^2]^{1/2} \qquad (58)$$

$$\sin\theta_i = \frac{w_i - w_{i-1}}{\Delta s_i} \qquad (59)$$

$$\cos\theta_i = \frac{v_i - v_{i-1}}{\Delta s_i} \qquad (60)$$

The fundamental variables entering into the above equations of motion are defined as follows:

N	=	internal axial force
Q	=	internal shear force
M	=	internal moment
θ	=	angle between y-axis and bar
Δs	=	length of bar
m	=	discrete mass
v	=	position in the y direction

w = position in the z direction

F_y = external force per unit length in the y direction

F_z = external force per unit length in the z direction

The double dot over the variables v and w represents double differentiation with respect to time, i.e., $\ddot{v} = d^2(v)/dt$. Since each mass point must be in dynamic equilibrium at all times, equations (55-57) must apply to all points, i = 1,N, where N is the total number of masses in the model.

The numerical procedure for solving equations (55-57) is to first find all Q_i's from equation (57), then find $\ddot{v}_i$ and $\ddot{w}_i$ from equations (55) and (56), respectively. Determination of N_i, M_i, F_{y_i}, F_{z_i} and m_i will be explained in Subsections 4.1.3 to 4.1.8, and the temporal integration technique used to extrapolate quantities to the next time step is described in Subsection 4.1.10.

4.1.3 Variable Cross Section

For beams of variable cross sections where the width and thickness of any of the layers varies spanwise along the beam, a set of cross sections is developed where each corresponds to a particular bar in the bar-mass model (fig. 28). The width and thickness is initially specified at each mass point and each end of the beam. From that information uniform cross sections (width and thickness remaining constant) are generated. These uniform segments extend from one mass point to the next and the idealized dimensions of each are found by averaging the dimensions at either end.

Variations are assumed to be small so that laterally applied external pressure loads are assumed to act normal to the beam as located by the mass points. In other words, the local variations in surface orientations are neglected in determining the direction of the load vector.

4.1.4 Idealized Model of the Cross Section

The creation of an idealized model of the actual cross section requires first reducing the cross section to a set of uniform, rectangular layers, as shown in figure 29. Each layer, however, can have different physical properties as well as different geometric properties. The second step in modeling the cross section is to represent each layer by a set of one or more flanges in order to represent the extensional and bending stiffness in the layer. The more flanges used, the more accurate the representation, but at the expense of additional computer time. Hence, the number of flanges and the spacing within each layer must be optimized.

It should be noted that for a beam with nonuniform cross section in the spanwise direction the cross section at the center of the beam is modeled for the desired number of flanges and flange spacing and this flange representation is used for the entire beam. To do otherwise would be exceedingly complicated, resulting in little additional accuracy. This assumption does not significantly affect the ability to analyze nonuniform cross sections.

The number of flanges allotted to each layer of material is determined on the basis of bending of a composite beam. The number of flanges in a layer is allotted approximately in proportion to the elastic modulus, E, and the width, b, for the layer, the depth, h, of the layer. Because the thickness plays a more important role in bending, the number of flanges is actually determined by $h(Eb)^{0.75}$. The allotment is not exactly proportional to $(h(Eb)^{0.75})$ for each layer since this would result in fractional numbers of flanges. Actually, in the computer program, the number of flanges for each layer is obtained by selecting an even number n (2, 4, 6,...) for the layer with the largest value of $(h(EB^{0.75})$, calculating a number n_k for each layer "k" from

$$n_k = n \frac{h_k(E_k b_k)^{0.75}}{h(Eb)^{0.75}} \tag{61}$$

and rounding n_k to the nearest even integer, or if less than 1.5, n_k is rounded to 1. Even integers are preferable because the bending stiffness of each layer of material can be represented more effectively with a minimum number of flanges. The reasons for this selection are more readily apparent from the discussions which follow on the area and spacing of the flanges.

The area and spacing of the flanges in each layer are evaluated from considerations of both the extensional and bending stiffnesses of the cross section. It is desirable, if possible, to duplicate the bending and axial extensional stiffness of the entire cross section through all phases of stress; elastic, elastic plus plastic, and all plastic. It is impossible to duplicate all possible elastic plus plastic stress conditions without the use of an infinite number of flanges in each layer of material. It is possible, however, to reproduce easily the normal force, N, and the moment, M, resulting from the following strain conditions:

1. Any purely elastic strain
2. Purely plastic axial strain
3. Purely plastic bending strain

Satisfying the above strain conditions guarantees that any strain condition will be reasonably well reproduced.

For a multilayered beam, if the elastic extensional and elastic bending stiffnesses of each layer of material of the cross section are reproduced, all three of the strain conditions listed above are correctly treated. Figure 29 illustrates the actual cross section for a multilayered beam and the idealized flange representation of the cross section used in the computer program. In the idealized representation the flanges in a layer are of equal area and are distributed symmetrically about the centerline of the layer. The elastic extensional and elastic bending stiffnesses are reproduced by the following area and spacing of the flanges:

$$A_k = \frac{b_k h_k}{n_k} \tag{62}$$

$$d_k = \frac{h_k}{\sqrt{n_k^2 - 1}} \tag{63}$$

where

A_k = the area of each flange in layer "k"

b_k = width of layer "k"

d_k = spacing between flanges in layer "k"

h_k = the height of layer "k"

n_k = the number of flanges in layer "k"

k = the kth layer

As pointed out earlier, this representation is based on an even number of flanges for each layer of material. Actually, the uniform spacing between flanges could be based on a symmetrical distribution of flanges about the centerline of the layer, with one flange located on the centerline. This representation is not desirable because the flange located at the centerline is ineffective in reproducing the elastic and purely plastic bending stiffness of the layer.

The one exception to the spacing formulas (63) is when only one flange is assigned to the layer, in which case the flange is located at the center of the layer and $d_k = 0$.

The strain for pure bending is zero within some layer of the cross section. Therefore, the correct representation of the purely plastic bending condition is obtained by dividing the layer in which the strain is zero into two equal layers. The dividing line is the zero strain axis, and both layers have identical material properties. The flange area and spacing are determined as before except that the idealized cross section contains L+1 layers instead of the L layers of the

actual cross section. This approach is very useful for a single-layer cross section because the two layers are positioned symmetrically about the centroidal axis. Representing the elastic bending stiffness of each layer by flanges distributed symmetrically about the centerline of each layer reproduces both the elastic bending and purely plastic bending stiffnesses of the entire cross section.

The internal bending moment for the cross section is determined by using the reference axis in figure 29. The inertial forces are also based upon accelerations at the reference axis; therefore, the reference axis is located at the center of gravity of the cross section.

$$X_{cg} = \frac{\sum_{k=1}^{L} (h_1 + \ldots + h_{k-1} + \frac{h_k}{2}) \rho_k h_k b_k}{\sum_{k=1}^{L} \rho_k h_k b_k} \tag{64}$$

where

X_{cg} = the location of the centroidal axis (reference axis) with respect to the base of the cross section

ρ_k = the mass density of layer "k"

L = number of layers in the cross section

and the other variables are as defined earlier. As indicated in figure 29, the distance from the center of gravity to the rth flange located in the kth layer is depicted by ζ^r, and represents the bending moment arm for that flange. In the case of variable cross section, the parameters A_k, d_k, ζ and X_{cg} will all depend on spanwise position, and henceforth the subscript "i" will be attached to them to indicate that dependence.

4.1.5 Strain-Displacement Relations

Referring to figures 28 and 29 again, the finite difference equations representing the strain-displacement relations for the rth flange in the cross section at segment i are given by

$$\varepsilon^r_{i_N} = \frac{\Delta s_i - \Delta s_{i,o}}{\Delta s_{i,o}} - \zeta^r_i \left[\frac{\Delta\theta_i - \Delta\theta_{i,o}}{\Delta\bar{s}_{i,o}} + \frac{\Delta\theta_{i-1} - \Delta\theta_{i-1,o}}{\Delta\bar{s}_{i-1,o}} \right] \tag{65}$$

$$\varepsilon^r_{i_M} = \frac{1}{2} \left[\frac{\Delta s_i - \Delta s_{i,o}}{\Delta s_{i,o}} + \frac{\Delta s_{i+1} - \Delta s_{i+1,o}}{\Delta s_{i+1,o}} \right]$$

$$- \frac{1}{2} (\zeta^r_i + \zeta^r_{i+1}) \frac{(\Delta\theta_i - \Delta\theta_{i,o})}{\Delta\bar{s}_{i,o}} \tag{66}$$

where

$$\Delta\bar{s}_{i,o} = \frac{1}{2} (\Delta s_{i,o} + \Delta s_{i+1,o}) \tag{67}$$

$$\Delta\theta_i = \theta_{i+1} - \theta_i$$

$$= \sin^{-1}(\sin\theta_{i+1}\cos\theta_i - \cos\theta_{i+1}\sin\theta_i) \tag{68}$$

and

ε_N = strain used to compute the internal force, N.

ε_M = strain used to compute the internal moment, M.

The change of angle at mass i, $\Delta\theta_i$, is computed from the inverse sine formula since the sines and cosines are already available (eqs. (59-60)). Likewise, Δs_i is available from equation (58). The subscript "o" refers to the unstrained conditions.

The two distinct formulas for computing ε_N and ε_M arise from discretization - the fact that the internal force is computed in the ith bar; the moment is computed at the ith mass. Once the stresses, σ, are calculated based on the strains, the force and moment are the result of the following summations over all the flanges:

$$N_i = \sum_r \sigma^r_{i_N} A^r_i \tag{69}$$

$$M_i = \frac{1}{4} \sum_r \sigma^r_{i_M} (A^r_i + A^r_{i+1})(\zeta^r_i + \zeta^r_{i+1}) \tag{70}$$

The following section describes the stress-strain relations.

4.1.6 Stress-Strain Relations

The stress-strain model, depicted in figures 30 and 31, consists of a set of piece-wise linear segments defined at coordinates $((\varepsilon_k,\sigma_k)$, k = 1,2,...n). This uniaxial curve may be different in tension and compression, although the initial slope, σ_1/ε_1, is constrained to be the same in the following mathematic model.

In order to incorporate strain hardening and elastic unloading and reyielding, a "mechanical sublayer" model is adopted (ref. 31). This model is based on kinematic hardening (in a uniaxial sense) which takes the Bauschinger effect into account (see figure 32).

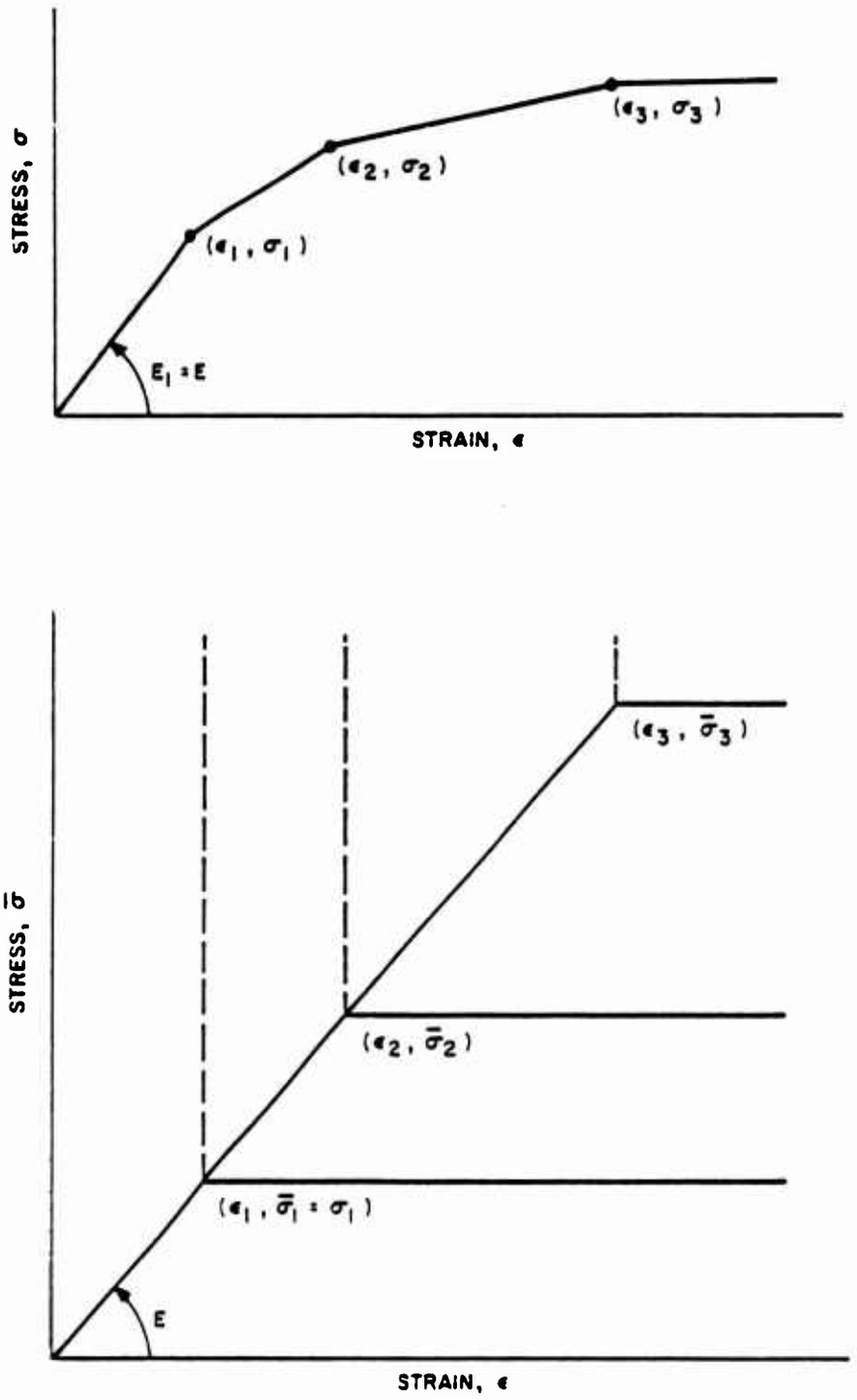

Figure 31. Schematic of Mechanical Sublayer Stress-Strain Model

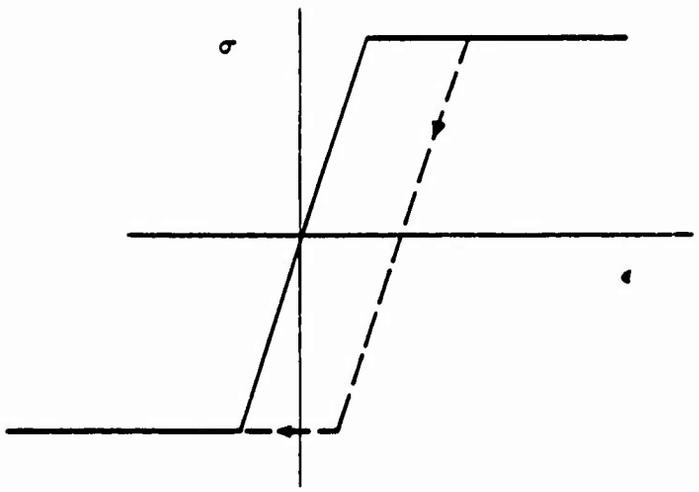

(a) Elastic-Perfectly Plastic Cycle

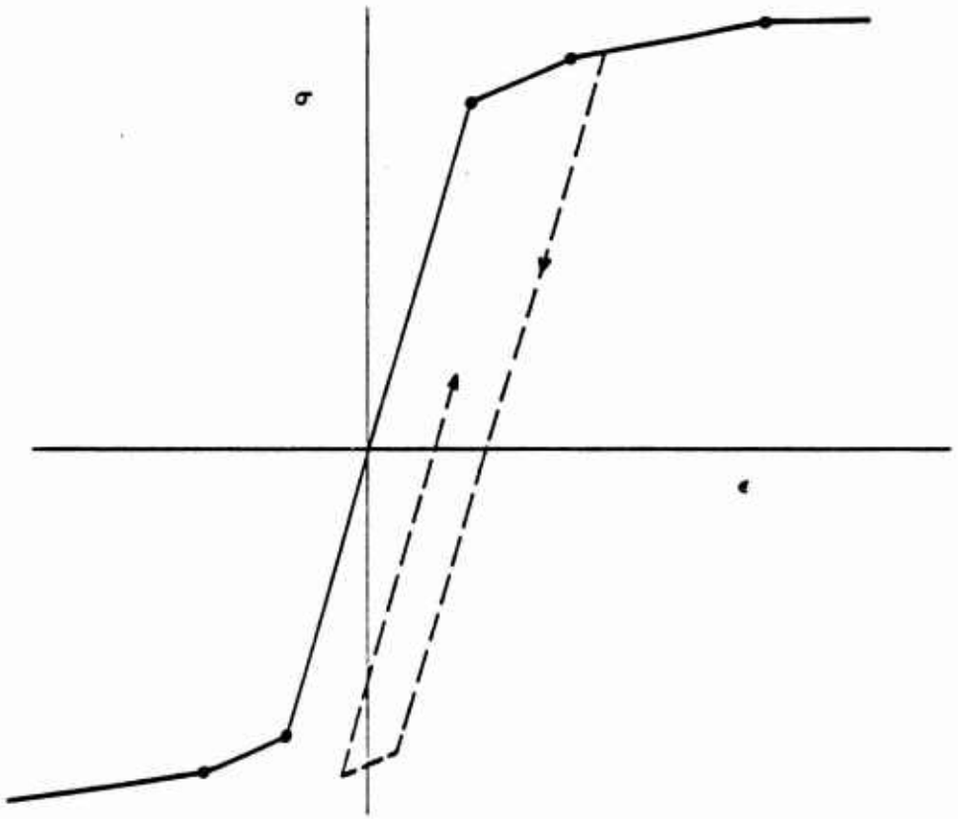

(b) General Loading Cycle

Figure 32. Cyclical Stress-Strain Load Paths

Each flange in the program is conceptually broken down into several subcomponents, or "sublayers". Each of these sublayers behaves in an elastic-perfectly plastic manner and each has the same modulus of elasticity, E, but each has a distinct fictitious yield stress associated with it, $\bar{\sigma}_k$. The value of $\bar{\sigma}_k$ is simply given by

$$\bar{\sigma}_k = E\varepsilon_k \tag{71}$$

Once the stress in each sublayer is found from its own elastic-perfectly plastic model and the strain, ε, the total stress can be determined by summing over each sublayer after weighting the stress in each sublayer by an appropriate weighting factor. This weighting factor simply takes into account the fictitious yield stresses used in the model.

$$\sigma = \sum_{k=1}^{n} c_k \, \sigma_k(\varepsilon) \tag{72}$$

where

$$c_k \equiv - \frac{E_{k+1} - E_k}{E} \tag{73}$$

and

$$E_k \equiv \begin{cases} E & k=1 \\ \dfrac{\sigma_k - \sigma_{k-1}}{\varepsilon_k - \varepsilon_{k-1}} & k=2,3,\ldots n \\ 0 & k=n+1 \end{cases} \tag{74}$$

In the case of an elastic-perfectly plastic material, there is only one sublayer. In general, each distinct slope of the stress-strain model in the entire tension-compression regime will dictate a unique sublayer, except for zero slope segments, which are automatically accounted for. The method makes two assumptions: 1) the modulus of elasticity is the same in both tension and compression, and 2) the break point stresses increase for increasing strain.

For problems involving complex cyclical load paths where points may unload, reyield, unload, etc., the method provides a very convenient mechanism to follow this behavior as only elastic-perfectly plastic curves are ultimately involved. It is also of note that the computation of the weighting factors, c_k's, need only be performed once since they are independent of time.

4.1.7 Boundary Conditions

DEPROB has the ability to analyze any combination of clamped, simply supported, and free edge conditions, including a symmetric "edge", where only half of the beam or ring is analyzed when the beam and its external loading are symmetric about the center. Each of the edge conditions is discussed below and the appropriate equations presented.

Clamped Edge

An ideal clamped edge condition is assumed, where zero deflection and zero slope are assumed at the clamp, as indicated in figure 33(a).

According to finite-difference techniques, the zero slope constraint would best be approximated by including at least one mass very near the edge, so that the zero slope constraint is maintained in a very localized region. For large deflection problems dominated by

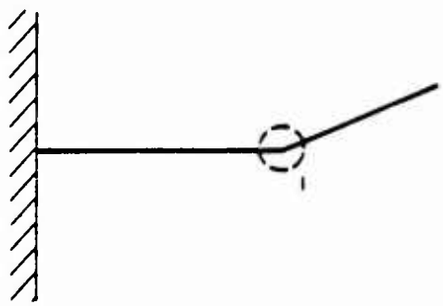

(a) Finite Difference Model

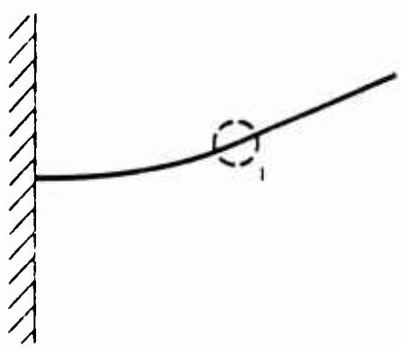

(b) Quasi-Static Model

Figure 33. Clamped Edge Models for Time > 0.

membrane forces, however, a large stress concentration occurs near the clamped edge and results in very large computational times due to the additional masses but, more importantly, also due to the small time increment thereby required in the solution. The time increment, Δt, as will be seen in subsection 4.1.10, is proportional to the shortest link in the model.

A new technique has been applied which eliminates these problems, with computational time on the order of ordinary finite-difference calculations, yet permitting a much higher degree of accuracy. This is accomplished by subdividing the segment (bar) nearest the edge into 10 unevenly spaced subsegments, with the subsegments more closely spaced near the edge. These subsegments are not used in the finite-difference equations, however. Instead they are the basis of a static solution, where, through an iterative process, the forces and the moment at the end of the first segment are found at each instant of time by satisfying the end deflections and an end slope condition. The use of a static solution is equivalent to ignoring the mass of the first bar, which is consistent with the discretization used throughout.

Figure 33(b) shows the relative advantage of this method over the previous method indicated in figure 33(a). The new method permits a more precise solution between the clamp and mass point 1, as it is allowed to deform with the rest of the beam.

When the beam is initially modeled, however, the first segment must be oriented perpendicular to the assumed wall, as shown in figure 34(a). It is appropriate that the length of that segment be on the order of other segments in the beam. Either or both of the ends of the beam can be clamped.

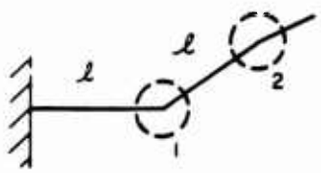

(a) Clamped

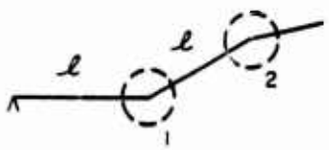

(b) Simply Supported

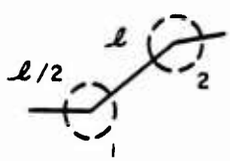

(c) Free

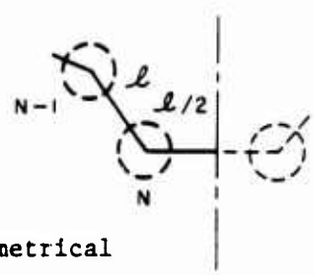

(d) Symmetrical

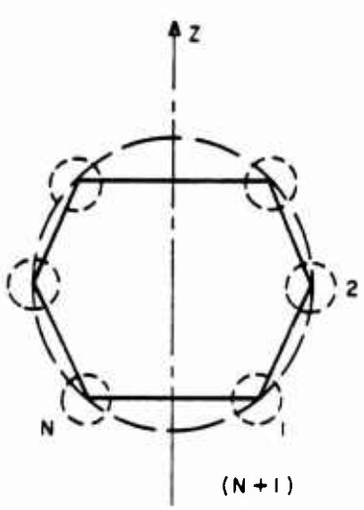

(e) Free Ring

Figure 34. Edge Conditions for Beam

Simply Supported Edge

A no-slip, knife edge (hinge) condition is imposed by requiring no deflection and no moment at the edge. As shown in figure 34(b), it is appropriate to initially model the beam with the segment nearest the edge approximately the same length as other segments in the beam. Either or both of the ends of the beam can be simply supported.

Free Edge

The free edge is characterized by zero moment and zero internal force in the outer bar. As indicated in figure 34(c), that outer segment should be roughly half that of other segments in the beam. Either or both of the ends can be free.

In the event that both ends are considered free, the structure can be analyzed if the center of gravity remains stationary and no rotation is introduced. The net translation and rotation of the beam are accounted for by calculating the accelerations responsible for this motion and subtracting them from the left-hand sides of equations (55) and (56). The rigid body accelerations $\ddot{v}$ and $\ddot{w}$ associated with translation are calculated from

$$\ddot{v}_T = \frac{\sum_{i=1}^{N} F_{y_i}}{M} \tag{75}$$

$$\ddot{w}_T = \frac{\sum_{i=1}^{N} F_{z_i}}{M} \tag{76}$$

where

$$M = \sum_{i=1}^{N} m_i \tag{77}$$

The rigid body rotational acceleration is determined from

$$\ddot{\theta} = \frac{\Gamma}{I} \tag{78}$$

where

$$I = \sum_{i=1}^{N} m_i r_i^2 \tag{79}$$

$$r_i^2 = (v_i - \bar{v})^2 + (w_i - \bar{w})^2 \tag{80}$$

$$\bar{v} = \frac{\sum_{i=1}^{N} m_i v_i}{M} \tag{81}$$

$$\bar{w} = \frac{\sum_{i=1}^{N} m_i w_i}{M} \tag{82}$$

$$\Gamma = \sum_{i=1}^{N} \left[(v_i - \bar{v}) F_{z_i} - (w_i - \bar{w}) F_{y_i} \right] \tag{83}$$

The coordinates $\bar{v}$, $\bar{w}$ represent the coordinates of the center of gravity of the system. Finally, the y and z components of acceleration due to the angular acceleration are, respectively,

$$\ddot{v}_{R_i} = -\ddot{\theta} (w_i - \bar{w}) \tag{84}$$

$$\ddot{w}_{R_i} = \ddot{\theta} (v_i - \bar{v}) \tag{85}$$

The total rigid body motion is formed by adding the contributions from eq. (75), (76), (84) and (85).

Symmetric Edge

When the beam and its loading are both symmetric about the center of the beam, only the first half need be analyzed. The program will automatically rotate the structure so that the plane of symmetry is parallel with the vertical (z) axis in figure 34(d). A fictitious mass (N+1) is constrained to move as a mirror image to mass N, thus enforcing zero slope and symmetric motion about the plane of symmetry. As indicated, the segment nearest the plane of symmetry should be only roughly half the length of other segments, because its mirror image is an equal distance on the other side.

Free Ring

As indicated in figure 34(e), the free ring must be modeled symmetrically, but is assumed to close on itself. The program then rotates the structure so that the plane of symmetry is parallel to the vertical (z) axis. As was the case with a free-free beam, rigid body rotation and translation are subtracted out of the solution, leaving motion only relative to the time dependent c.g. of the system.

4.1.8 Elastic Support at Discrete Points

The flexibility of DEPROB, particularly the ability to apply external loads to discrete mass points, lends itself to the analysis of three special structural configurations of interest. They are 1) a relatively weak frame situated between other relatively strong frames and deriving support from the connecting longerons and stringers, 2) a frame deriving support from outer skin when internally loaded (preblast) and 3) stringers and longerons deriving support from outer skin as in (2). Each will be discussed below.

A weak frame may derive elastic support from a longeron at the point at which the two structures are joined. The frames are assumed to be evenly spaced such that the stiffness coefficient associated with the longeron is given by

$$\frac{f}{\delta} = \frac{-192\ E'I'}{\ell'^3} \tag{86}$$

where

E' = modulus of elasticity of longeron
I' = moment of inertia of longeron
ℓ' = length of longeron between strong frames or bulkheads

The frame, analyzed by DEPROB, will then receive a restoring force proportional to the displacement δ and applied to the frame at that point. This technique obviously excludes dynamic coupling of the two elements but should be a reasonable approximation, particularly for the weak frame situation.

When a frame element is subjected to a net outward preload pressure due to internal pressurization of the fuselage, the outer skin makes a very significant hoop stress contribution in resisting outward

deformation that would not be properly accounted for when modeling the skin as part of the frame cross section. In order to correct for this, the tensile stress-strain curve is modified within the program to take into account the larger effective skin area when the outer layer is in tension.

For fuselage stringers and longerons under net outward preload pressure, a different approach is taken to correct the same problem that existed with the frame. In this case, a cylindrical section of aircraft skin actually contributes to the hoop stress strength of the structure. The restoring force at each point along the stringer can be shown to be approximately proportional to the deflection of the element:

$$f = \begin{cases} 0 & \delta \leq 0 \\ -2E\theta_s h \sin \frac{\theta_s}{2} \delta & \delta > 0 \end{cases} \qquad (87)$$

where

E = modulus of elasticity of skin

h = thickness of skin

θ_s = angular spacing between stringers around the fuselage

4.1.9 Preload Static Solution

The method chosen for solution of the preblast deformations due to steady-state loads is an iterative relaxation procedure designed to reduce the accelerations to zero. Once this equilibrium state is reached, the displacements are stored in the program so that a change of blast range or orientation will not necessitate solving the preblast problem again.

Due to the complexity of the solution procedure, the static solution is found for only seven boundary condition combinations. These should, however, solve any practical aircraft problem. The allowable combinations are

	1st End	2nd End
1)	Clamped	Clamped
2)	Clamped	Free
3)	Clamped	Symmetric
4)	Clamped	Simply supported
5)	Simply supported	Simply supported
6)	Simply supported	Symmetric
7)	Free ring	

4.1.10 Numerical Analysis

Integration of the second-order differential equations (55-56) is accomplished numerically by extrapolating the 2N displacements v_i, w_i in time. The integration used is the central difference formula

$$X_{k+1} = (\Delta t)^2 \ddot{X}_k + 2X_k - X_{k-1} \tag{88}$$

where

- X represents one of the 2N displacements
- Δt is the time increment
- k denotes the time step, 0,1,2...

Note that step zero corresponds to static conditions just after the blast has arrived but before the structure has responded. In order to start the procedure, the back point X_{-1} must be established. This is done at step zero by letting

$$X_{-1} = X_o + 1/2\ (\Delta t)^2\ \ddot{X}_o \tag{89}$$

The central difference formula (88) is known as an open method. For elastic problems the solution will be accurate, for all practical purposes, as long as the solution remains stable. Too large a time increment, however, will trigger a numerical instability. Stability can be related to longitudinal and lateral vibration frequencies of the beam (ref. 30). These criteria depend on the material properties and the geometry, including the spacing between adjacent mass points. For multilayered beams, average material properties are computed; and for beams of variable cross section, each station along the beam is checked to find the critical Δt. The following equations represent the Δt criteria, where the minimum value (when all links i=1,N are considered) is appropriate:

$$\Delta t = r\ \Delta s_{o,i} \sqrt{\frac{\bar{\rho}_i}{\bar{E}_i}}\ \text{Min} \left\{ \begin{array}{l} 1.0 \\ \\ \dfrac{\sqrt{3}\ n\ \Delta s_{o,i}}{\sqrt{n^2-1}\ h_i} \end{array} \right. \tag{90}$$

where n is the maximum number of flanges assigned to any layer, h is the total thickness of the cross section, and

$$\frac{\bar{\rho}_i}{\bar{E}_i} = \frac{\sum_{k=1}^{L} \rho_k h_k b_k}{\sum_{k=1}^{L} E_k h_k b_k} \tag{91}$$

The constant r has as a value a theoretical upper limit of 1.0, but a conservative value of 0.9 is used to avoid marginally unstable cases. It should be noted, however, that initially curved beam elements which experience "snap-through" buckling may require a significantly smaller time increment than that predicted by the above formula.

For solutions which go inelastic, and for column buckling types of problems, the solution may deteriorate without actually diverging. For these cases it is recommended that particular attention be paid to the validity of the results. This can easily be checked by using a time increment somewhat smaller than that previously used and comparing results.

4.1.11 DEPROB Response Comparisons with Experiments and with an MIT Code

As partial verification of the DEPROB code, the dynamic responses of two clamped-clamped uniform straight aluminum beams, subjected to impulsive loads on the center portion of the span, are presented in table 11 and figures 35 and 36. Deflection time histories are shown for each beam as determined by 1) DEPROB calculations, 2) experiment (ref. 29), and 3) MIT beam code.

These particular beam tests were selected due to the relatively good experimental data and because of the inelastic nature of the response. The second beam is nearly identical to the first except it is twice as thick and does not exhibit as much strain hardening as the first. In order to make these comparisons, the DEPROB program was temporarily modified to incorporate an impulsive lateral load over a portion of the beam.

The most important conclusion which can be drawn from the results is that the two structural response codes predict almost exactly the same deflection time history (comparison of strains was not possible). This is no surprise, since DEPROB is based to a large degree in the MIT code; but, nevertheless, enough changes have been made so that these results are reassuring. Secondly, the two experimental traces show no significant differences from the code predictions, except at late times, thus lending even more credence to the DEPROB results.

TABLE 11

GEOMETRICAL AND PHYSICAL PROPERTIES OF BEAMS

DEPROB Models	Beam 95 (ref. 29)	Beam 111 (ref. 29)
Material Properties	Aluminum 6061-T6	Aluminum 6061-T6
E, psi	10.81×10^6	10.7×10^6
σ_o, psi	41600	41200
E_t, psi	161000	61200
ρ, lb/in^3	0.098	0.097
Length, in	10.0	10.0
Thickness, in	0.124	0.242
Width, in	1.195	1.195
Total Impulse, psi-sec	0.1575	0.2724
Initial Velocity, ft/sec	5003	4480
Length of Charge (centered on ℄)	1.932	1.988
Edge Conditions	Clamped	Clamped
Number of Masses in Half Span Model	30	30
Number of Flanges	12	12
Time Increment, sec	0.75×10^{-6}	0.75×10^{-6}
Measured Permanent Set, in	0.581	0.522

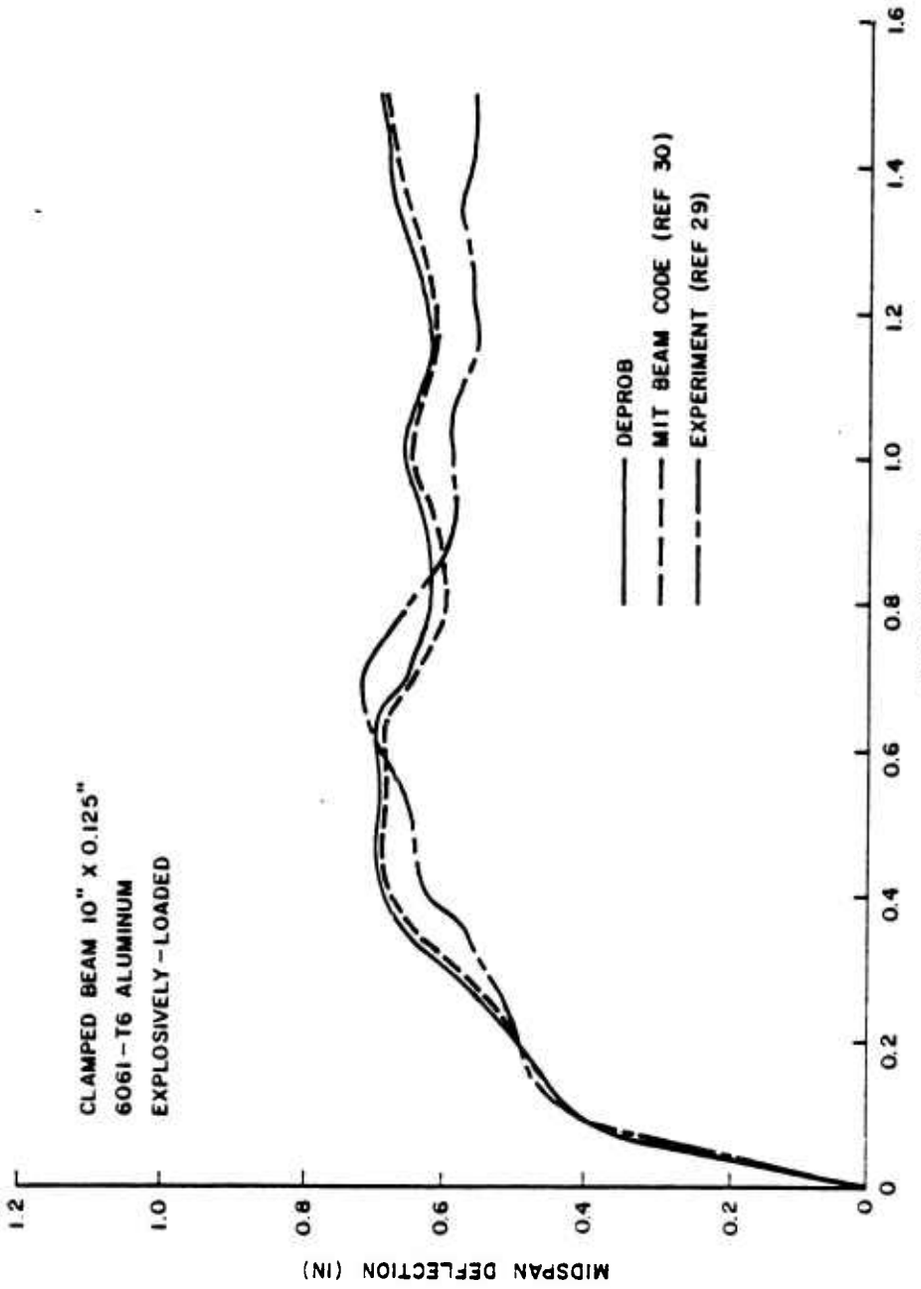

Figure 35. Dynamic Response of Beam 1/8 Inch Thick

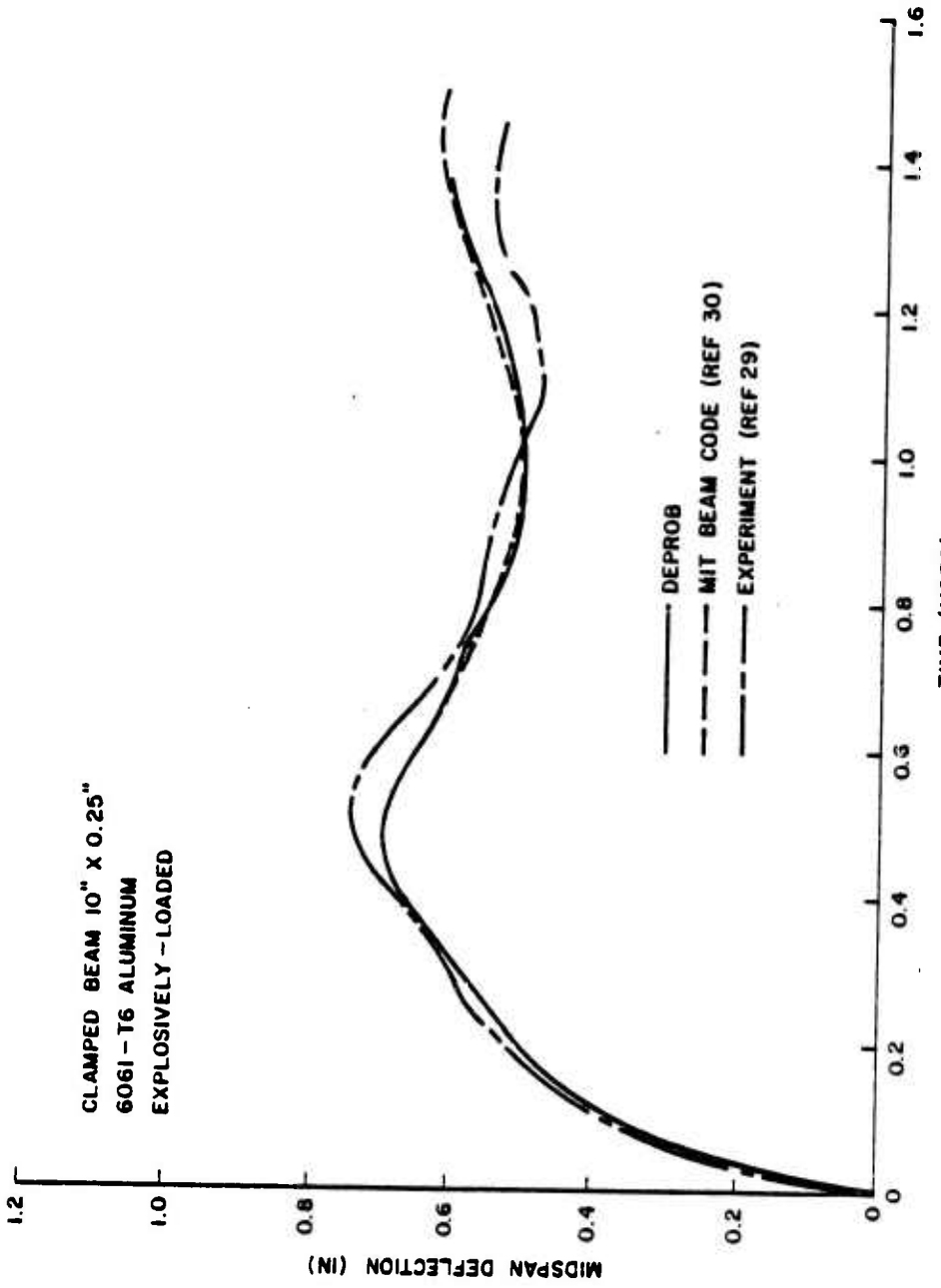

Figure 36. Dynamic Response of Beam 1/4 Inch Thick

4.2 DYNAMIC ELASTIC-PLASTIC RESPONSE OF PANELS — DEPROP

The structural response program DEPROP was developed to calculate the linear elastic and elastic-plastic response of aircraft panels to static and dynamic pressure loads. Panels on aircraft can generally be approximated by cylindrical or flat panels with combination of clamped and simply supported boundary conditions and can be single or multi-layered with isotropic or orthotropic material properties. The DEPROP program is a modification of a dynamic nonlinear cylindrical shell program called DEPICS (refs. 32-34) and contains the capabilities of specifying a static uniform pressure loading (preload) and a transient uniform pressure loading on the panel.

The DEPROP analysis is based on the Novozhilov nonlinear strain-displacement relations for large displacement response of thin panels based on the assumption of undeformable normals. The program has response options for either linear elastic or elastic-plastic material behavior. The linear elastic option can be used with multiple layers of isotropic or orthotropic material. An elastically isotropic material possesses elastic properties which are identical in all directions and are, therefore, independent of the orientation of the coordinate axes. The elastically orthotropic material defined for these panels under plane stress conditions possesses three orthogonal planes of elastic symmetry that are parallel to the geometric coordinate axes. The elastic-plastic option provides an estimate of severe damage for a single-layered isotropic panel for a material with an assumed uniaxial bilinear stress-strain curve. The inelastic formulation is based on the Mises-Hencky yield surface, a kinematic hardening model and the Hencky stress-strain relations from the deformation theory of plasticity with modifications for regions of elastic unloading and reyielding. The DEPROP program calculates displacement, strain, and stress time histories at selected positions on the panel to be used in conjunction with various damage criteria.

4.2.1 Basic Theory

The single-layered cylindrical panel is considered to have a constant thickness h, mean radius a, subtended angle θ_o and length ℓ. The cylindrical coordinates (x, θ, z) and the axial, tangential, and radial displacement components (u, v, w) are shown in figure 37 on the coordinate surface which is located at the median surface of the panel. The governing equations of motion for the panel are obtained from the principle of virtual work for a dynamic structural system (ref. 35) which is given by

$$\int_{t_1}^{t_2} \left[\iiint_V \sigma_{ij} \, \delta\tilde{\varepsilon}_{ij} dV - \delta T - \iint_A \bar{F} \cdot \delta\bar{d} \, dA \right] dt = 0 \qquad (92)$$

where the panel is undergoing an arbitrary set of infinitesimal virtual displacements δu, δv, δw that satisfy the geometrical boundary conditions and vanish at $t=t_1$ and t_2; T is the kinetic energy; σ_{ij} are the components of total stress; $\tilde{\varepsilon}_{ij}$ are the components of total strain; $\bar{F}$ is the surface force vector; $\bar{d}$ is the displacement vector; and integrations are carried over volume V and deformed surface area A. It should be noted that this principle holds regardless of whether the material's stress-strain relations are elastic or inelastic and whether the force system is conservative or nonconservative. If it is assumed that $T=T(\dot{u},\dot{v},\dot{w})$, then

$$\delta T = \frac{\partial T}{\partial \dot{u}} \delta\dot{u} + \frac{\partial T}{\partial \dot{v}} \delta\dot{v} + \frac{\partial T}{\partial \dot{w}} \delta\dot{w} \qquad (93)$$

where the dots denote differentiation with respect to time. With equation 93 and using integration by parts,

$$\int_{t_1}^{t_2} \delta T \, dt = - \int_{t_1}^{t_2} \left(\frac{d}{dt} \frac{\partial T}{\partial \dot{u}} \delta u + \frac{d}{dt} \frac{\partial T}{\partial \dot{v}} \delta v + \frac{d}{dt} \frac{\partial T}{\partial \dot{w}} \delta w \right) dt \qquad (94)$$

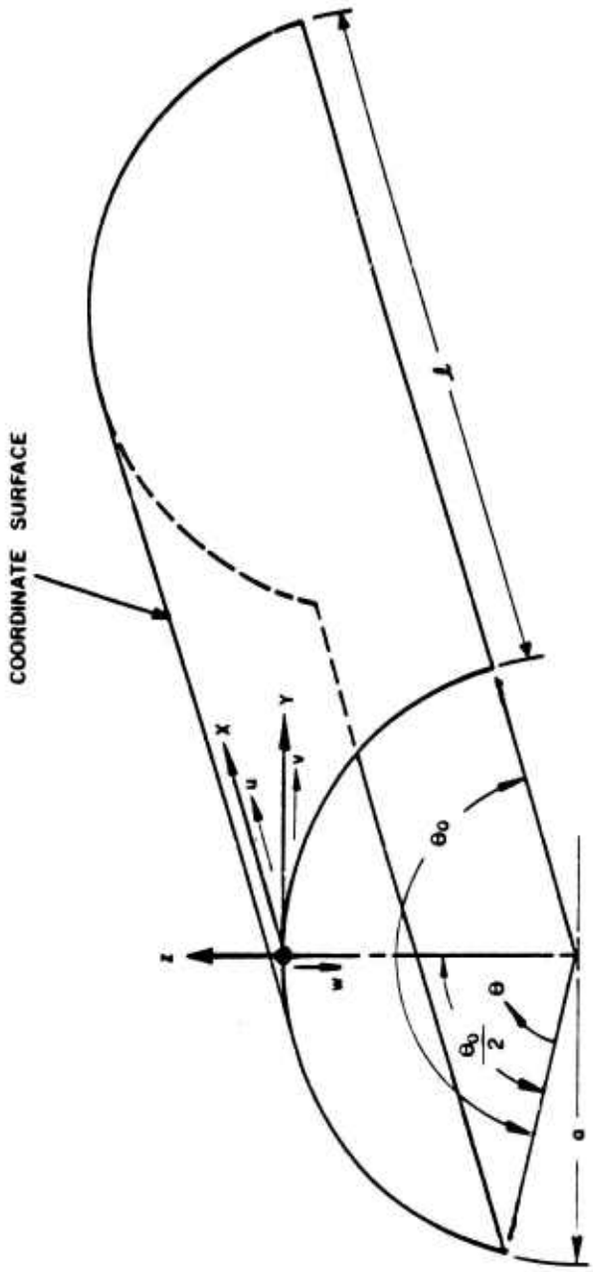

Figure 37 - Coordinate Surface for Cylindrical Panel

It is assumed that the uniform blast pressure, p(t), acts on the coordinate surface of the cylindrical or flat panel. As the panel surface deforms, the elemental pressure force vector remains normal to the coordinate surface so that it changes direction during deformation. The magnitude of this force vector also changes as the element surface area of the deformed panel changes. It should be noted that the portion of the pressure loading associated with the force vector's dependence on the deformations represents a nonconservative force system. Based on the rectangular coordinate system (X,Y,Z), the components η_X, η_Y and η_Z of the inward unit normal surface vector and the components d_X, d_Y and d_Z of the displacement vector $\bar{d}$ were defined in reference 32 in terms of u, v and w and their spatial derivatives. Thus, the vector dot product of the force and virtual displacement is expressed as

$$\bar{F} \cdot \delta\bar{d} = p(t)(\eta_X \delta d_X + \eta_Y \delta d_Y + \eta_Z \delta d_Z) \tag{95}$$

By neglecting terms above the second order and recasting in terms of the virtual displacements δu, δv and δw, the virtual work done by the external forces is given by

$$\int\int_A \bar{F} \cdot \delta\bar{d}\, dA = \int\int_{\bar{A}} p(t)(N_u \delta u + N_v \delta v + N_w \delta w) d\bar{A} \tag{96}$$

where

$$N_u = -(w_x + \overset{\circ}{w}_x)$$

$$N_v = -(w_\theta + \overset{\circ}{w}_\theta + v)/a$$

$$N_w = 1 - (w + \overset{\circ}{w} - v_\theta)/a + u_x$$

$$\bar{A} = \text{undeformed surface area}$$

The subscripts on the displacement components denote spatial derivatives and $\overset{\circ}{w}$ denotes initial radial imperfection in the panel.

With equations 94 and 96 and the relation

$$\delta\tilde{\varepsilon}_{ij} = \frac{\partial\tilde{\varepsilon}_{ij}}{\partial u}\,\delta u + \frac{\partial\tilde{\varepsilon}_{ij}}{\partial v}\,\delta v + \frac{\partial\tilde{\varepsilon}_{ij}}{\partial w}\,\delta w$$

equation 92 becomes

$$\int_{t_1}^{t_2} \Bigg\{ \left[\frac{d}{dt}\,\frac{\partial T}{\partial \dot{u}} + \iiint_V \sigma_{ij}\,\frac{\partial\tilde{\varepsilon}_{ij}}{\partial u}\,dV - \iint_{\bar{A}} pN_u\,d\bar{A} \right] \delta u + \left[\frac{d}{dt}\,\frac{\partial T}{\partial \dot{v}} \right.$$

$$\left. + \iiint_V \sigma_{ij}\,\frac{\partial\tilde{\varepsilon}_{ij}}{\partial v}\,dV - \iint_{\bar{A}} pN_v\,d\bar{A} \right] \delta v + \left[\frac{d}{dt}\,\frac{\partial T}{\partial \dot{w}} \right.$$

$$\left. + \iiint_V \sigma_{ij}\,\frac{\partial\tilde{\varepsilon}_{ij}}{\partial w}\,dV - \iint_{\bar{A}} pN_w\,d\bar{A} \right] \delta w \Bigg\}\,dt = 0 \qquad (97)$$

The displacement components are assumed in the following truncated series form with undetermined time-dependent coefficients, $u_{mn}(t)$, $v_{mn}(t)$, $w_{mn}(t)$:

$$u(x,\theta,t) = \sum_{m=1}^{M} \sum_{n=1}^{N} u_{mn}\phi_m^u(x)\phi_n^u(\theta)$$

$$v(x,\theta,t) = \sum_{m=1}^{M} \sum_{n=1}^{N} v_{mn}\phi_m^v(x)\phi_n^v(\theta)$$

$$w(x,\theta,t) = \sum_{m=1}^{M} \sum_{n=1}^{N} w_{mn}\phi_m^w(x)\phi_n^w(\theta) \tag{98}$$

where $\phi_m(x)$ and $\phi_n(\theta)$ are functions that satisfy the geometric boundary conditions of the panels. The initial radial imperfection in the panel is represented by

$$\overset{\circ}{w}(x,\theta) = \sum_{m=1}^{M} \sum_{n=1}^{N} \Delta_{mn}\phi_m^w(x)\phi_n^w(\theta) \tag{99}$$

where Δ_{mn} are prescribed values based on known or assumed deviations from the ideal shape of the panel. Based on equation 98, the following relations are obtained:

$$\delta u = \sum_{m=1}^{M} \sum_{n=1}^{N} \delta u_{mn}\phi_m^u\phi_n^u, \quad \delta v = \sum_{m=1}^{M} \sum_{n=1}^{N} \delta v_{mn}\phi_m^v\phi_n^v, \quad \delta w = \sum_{m=1}^{M} \sum_{n=1}^{N} \delta w_{mn}\phi_m^w\phi_n^w$$

$$\frac{\partial u}{\partial u_{mn}} = \phi_m^u\phi_n^u, \quad \frac{\partial v}{\partial v_{mn}} = \phi_m^v\phi_n^v, \quad \frac{\partial w}{\partial w_{mn}} = \phi_m^w\phi_n^w \tag{100}$$

Introducing equation 100 into equation 97 and since δu_{mn}, δv_{mn} and δw_{mn} are arbitrary, the following 3MN equations of motion are obtained:

$$\frac{d}{dt}\frac{\partial T}{\partial \dot{u}_{mn}} + \iiint_V \sigma_{ij}\frac{\partial \tilde{\varepsilon}_{ij}}{\partial u_{mn}}\,dV - \int_A \hat{Q}_{mn}^u\,d\bar{A} = 0 \tag{101a}$$

$$\frac{d}{dt}\frac{\partial T}{\partial \dot{v}_{mn}} + \iiint_V \sigma_{ij}\frac{\partial \tilde{\varepsilon}_{ij}}{\partial v_{mn}}\,dV - \iint_{\bar{A}} \tilde{Q}^{v}_{mn}\,d\bar{A} = 0 \qquad (101b)$$

$$\frac{d}{dt}\frac{\partial T}{\partial \dot{w}_{mn}} + \iiint_V \sigma_{ij}\frac{\partial \tilde{\varepsilon}_{ij}}{\partial w_{mn}}\,dV - \iint_{\bar{A}} \tilde{Q}^{w}_{mn}\,d\bar{A} = 0 \qquad (101c)$$

$(m=1,2,3\ldots M) \quad (n=1,2,3\ldots N)$

where the integrands of the generalized forces ($\tilde{Q}^{u}_{mn}$, $\tilde{Q}^{v}_{mn}$, $\tilde{Q}^{w}_{mn}$) are given by

$$\tilde{Q}^{u}_{mn} = pN_u\frac{\partial u}{\partial u_{mn}}, \quad \tilde{Q}^{v}_{mn} = pN_v\frac{\partial v}{\partial v_{mn}}, \quad \tilde{Q}^{w}_{mn} = pN_w\frac{\partial w}{\partial w_{mn}} \qquad (102)$$

The kinetic energy of a single-layered panel is given as

$$T = \frac{a\rho h}{2}\int_0^{\ell}\int_0^{\theta_o}(\dot{u}^2 + \dot{v}^2 + \dot{w}^2)\,dx d\theta \qquad (103)$$

where ρ is the mass density of the material and the dots denote differentiation with respect to time. The rotary inertia contributions to the kinetic energy have been neglected. Modification of the mass density for multilayered panes is introduced in subsection 4.2.5. Further development of equation 101 depends upon the establishment of the strain-displacement relations, the stress-strain relations and the displacement component spatial functions.

4.2.2 Strain-Displacement Relations

The strain-displacement relations used in this analysis are based on the assumptions: (1) strains are small compared with unity, (2) the thickness of the shell is small compared with the radius and (3) the Kirchhoff - Love hypothesis that straight fibers which are normal to the undeformed coordinate surface remain straight and normal to the deformed coordinate surface and are not elongated, thus neglecting transverse shear and normal strains. The basic formulation of the following set of nonlinear strain-displacement relations is attributed to Novozhilov (ref. 36). The total strain consists of membrane and bending components expressed by the form $\varepsilon = \varepsilon + z\kappa$. The membrane elongation and shear strains (ε_{xx}, $\varepsilon_{\theta\theta}$, $\varepsilon_{x\theta}$) on the coordinate surface are expressed in terms of the displacement components and their spatial derivatives:

$$\varepsilon_{xx} = u_x + \frac{1}{2}\left[w_x^2 + u_x^2 + v_x^2\right] + w_x \overset{\circ}{w}_x \tag{104a}$$

$$\varepsilon_{\theta\theta} = \frac{1}{a} v_\theta - \frac{1}{a}\lambda w + \frac{1}{2a^2}\left[(w_\theta + \lambda v)^2 + (v_\theta - \lambda w)^2 + u_\theta{}^2\right] + \frac{1}{a^2} w_\theta \overset{\circ}{w}_\theta \tag{104b}$$

$$\varepsilon_{x\theta} = v_x + \frac{1}{a} u_\theta + \frac{1}{a} w_x (w_\theta + \lambda v) + \frac{1}{a} v_x (v_\theta - \lambda w) + \frac{1}{a} u_\theta u_x + \frac{1}{a}\left(\overset{\circ}{w}_x w_\theta + \overset{\circ}{w}_\theta w_x\right) \tag{104c}$$

Similarly, the change of curvature quantities (κ_{xx}, $\kappa_{\theta\theta}$, $\kappa_{x\theta}$) of the coordinate surface which characterize the bending and torsional deformations of the panel are given by

$$\kappa_{xx} = w_{xx}\,(1 + v_\theta/a - \lambda w/a + u_x) \tag{105a}$$

$$\begin{aligned}\kappa_{\theta\theta} = {} & \frac{1}{a^2} w_{\theta\theta} + \frac{\lambda}{a^2} v_\theta + \frac{\lambda}{a^2} (-w + v_\theta) + \frac{\lambda}{a} u_x \\ & + \frac{1}{a^3} (w_{\theta\theta} + \lambda v_\theta)(v_\theta - \lambda w) \\ & + \frac{1}{a^2} w_{\theta\theta} u_x + \frac{\lambda}{a^3} (v_\theta - w)^2 + \frac{\lambda}{a^3} (w_\theta + v)^2 \\ & + \frac{\lambda}{a^3} w_\theta (w_\theta + v)\end{aligned} \tag{105b}$$

$$\begin{aligned}\kappa_{x\theta} = {} & \frac{2}{a} w_{x\theta} + \frac{\lambda}{a} v_x + \frac{2}{a^2} w_{x\theta}\,(v_\theta + a u_x - \lambda w) \\ & + \frac{2\lambda}{a^2} w_x (w_\theta + v)\end{aligned} \tag{105c}$$

Primarily, only those nonlinear terms are included in equation 105 which involve the radial displacement and its derivatives. The subscripts on the displacement components in equation 104 and 105 denote partial spatial derivatives. The end terms in equation 104 are included to account for the initial radial imperfection of the panel as indicated by Donnell's representation in reference 37. The parameter λ is introduced in the strain-displacement relations so that they apply to both curved and flat panels. Thus, $\lambda = 1$ for curved panels. For flat panels, $\lambda = 0$, $a = 1$, θ is replaced by y, and θ_o is replaced by b, the width of the flat panel.

4.2.3 Constitutive Relations

In DEPROP, the behavior of the panel material is treated as elastic-plastic for isotropic single-layered panels and elastic for isotropic and orthotropic multilayered panels. The elastic-plastic analysis for the single-layered panel has been established as the basic formulation in the DEPROP program. The elastic multilayered analysis is established as an alternate option based on appropriate modifications of the elastic-plastic formulation. In the DEPROP analysis the solution involves total strains and stresses; therefore, for response in the inelastic region, it is convenient to use the deformation theory of plasticity instead of flow theory which involves incremental strains and stresses. Plastic deformation theory is based on an averaging process that permits a total strain solution dependent upon only the final stress state at the end of a loading path. In general, deformation theory is an approximation of the more rigorous flow (incremental) theory but is equivalent to flow theory for an elastic-plastic material when the stress loading is proportional, that is, the ratio of principal stresses remain constant during the loading process. However, since the dynamic response solution is solved incrementally in time by numerical methods in DEPROP, the strain increments are small and the stress state is fairly constant in the plastic region over each time step for which the equations of motion are solved. Thus, the plastic deformation theory provides a much more accurate solution when the averaging process takes place separately over each small time increment as the response solution is obtained by a step-by-step timewise procedure.

In deformation theory the total strain is a function of the state of stress and consists of a recoverable elastic component and a nonrecoverable plastic component. It is assumed that the material is incompressible, that is, no permanent change in volume, due to the plastic strain. Thus, the total plastic strain is equal to the deviator plastic strain. Furthermore, it is assumed that the material's uniaxial

stress-strain curve is modeled by the bilinear representation shown in figure 38 in which the strain hardening is defined by slope E_t. This stress-strain representation is interpreted for the biaxial state of stress through the use of the effective stress ($\bar{\sigma}$)-effective strain ($\bar{\varepsilon}$) concept in which the secant modulus (E_s) indicated in figure 38 is defined by

$$E_s = \frac{\bar{\sigma}}{\bar{\varepsilon}} = \frac{\sigma_o + E_t\,(\bar{\varepsilon} - \varepsilon_o)}{\bar{\varepsilon}} \tag{106}$$

where σ_o, ε_o are the yield stress and strain, respectively, from the material's uniaxial bilinear representation. Thus, the effective stress, effective strain and secant modulus quantities are used to relate the biaxial stress-strain condition to the assumed uniaxial bilinear stress-strain representation for the isotropic material. The effective stress and strain, expressed as $\bar{\sigma} = f(\sigma_{ij})$ and $\bar{\varepsilon} = g(\tilde{\varepsilon}_{ij})$, are functions of the total stress and strain components, respectively, and are more conveniently introduced in explicit form later in the development.

The Hencky stress-strain relations for deformation theory (ref. 38) are used in the plastic region and are given in the following form:

$$\tilde{\varepsilon}_{ij} = \frac{1}{E}\left[(1+\nu)\sigma_{ij} - \nu\sigma_{kk}\delta_{ij}\right] + \frac{3}{2}\left(\frac{1}{E_s} - \frac{1}{E}\right)\left[\sigma_{ij} - \frac{1}{3}\sigma_{kk}\delta_{ij}\right] \tag{107}$$

where E is the modulus of elasticity, ν is Poisson's ratio and δ_{ij} is the Kronecker delta. The first portion of equation 107 represents the elastic component of strain while the second portion represents the plastic component of strain in terms of the deviator stress. For use in equation 101, the stress-strain relations in equation 107 are inverted into the form $\sigma_{ij} = f(\tilde{\varepsilon}_{ij})$ for the case of plane stress ($\sigma_{zz}=\sigma_{\theta z}=\sigma_{xz}=0$), and are given by

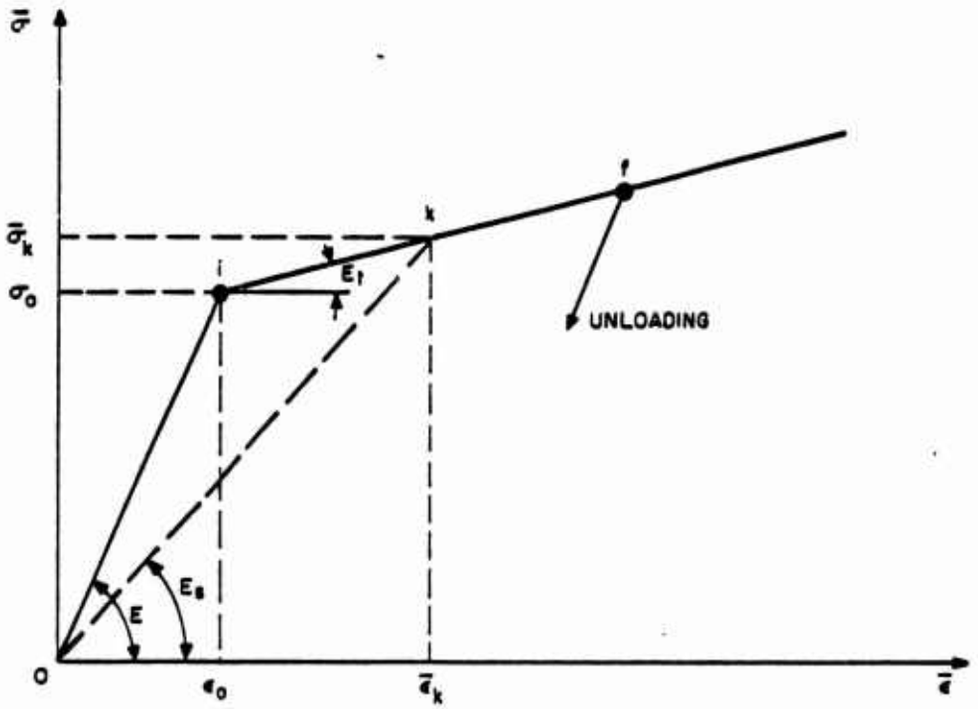

Figure 38. Effective Stress-Strain Bilinear Representation

$$\sigma_{ij} = \frac{E_s}{1-\nu_s^2}\left[(1-\nu_s)\tilde{\varepsilon}_{ij} + \nu_s\tilde{\varepsilon}_{kk}\delta_{ij}\right] \quad (i,j,k=1,2) \qquad (108)$$

where

$$\nu_s = \frac{1}{2} - \frac{E_s}{E}\left(\frac{1}{2} - \nu\right)$$

$$\tilde{\varepsilon}_{12} = \frac{1}{2}\tilde{\varepsilon}_{x\theta},\ \tilde{\varepsilon}_{11} = \tilde{\varepsilon}_{xx},\ \tilde{\varepsilon}_{22} = \tilde{\varepsilon}_{\theta\theta}$$

It should be noted that the forms of the stress-strain relations in the elastic (E_s=E) and plastic regions are identical.

The yield criterion, in conjunction with a hardening rule, and the stress-strain relation for unloading and reyielding by which the past strain history is preserved are to be established. The initiation of yielding for a biaxial state of stress is based on the Mises-Hencky yield criterion (ref. 38) given as

$$\bar{\sigma} = \left[\sigma_{11}^2 + \sigma_{22}^2 - \sigma_{11}\,\sigma_{22} + 3\sigma_{12}^2\right]^{1/2} \qquad (109)$$

where $\bar{\sigma}$ is the equivalent or effective stress and

$$\sigma_{11} = \sigma_{xx},\ \sigma_{22} = \sigma_{\theta\theta},\ \sigma_{12} = \sigma_{x\theta}$$

This yield criterion states that plastic flow will occur when the equivalent stress $\bar{\sigma}$ reaches a value equal to the uniaxial yield stress in tension σ_o. A kinematic hardening model is employed in conjunction with the Mises-Hencky yield surface which accounts for the Bauschinger effect when reyielding occurs due to the strain reversals during unloading. The Bauschinger effect for a strain hardening material is described by the yielding behavior of a material at a reduced yield stress when reloaded in the opposite direction from that of the initial yielding.

The kinematic hardening models discussed in reference 39 assume that during plastic deformation the yield surface translates as a rigid body in stress space with the size, shape and orientation of the elliptical yield surface being invariant. The kinematic hardening model to be used in this analysis is illustrated in figure 39 for the Mises-Hencky yield surface in the plane of the principal stresses σ_1 and σ_2. Corresponding to the initial yielding position (i) and the unloading position (f) indicated in figure 38, the rigid translation of the yield surface for a shift of the stress state from position (i) to position (f) is shown in figure 39. The change in total stress components from position (i) to position (f) are defined by $\overset{\sim}{\alpha}_{ij}$ and, similarly, the corresponding change in the total strain components are defined by $\overset{\gamma}{\beta}_{ij}$, so that

$$\overset{\sim}{\alpha}{}^{r}_{ij} = \overset{\sim}{\alpha}{}^{r-1}_{ij} + \sigma^{r-1}_{ij(f)} - \sigma^{r-1}_{ij(i)}$$

$$\overset{\gamma}{\beta}{}^{r}_{ij} = \overset{\gamma}{\beta}{}^{r-1}_{ij} + \overset{\sim}{\varepsilon}{}^{r-1}_{ij(f)} - \overset{\sim}{\varepsilon}{}^{r-1}_{ij(i)} \qquad (110)$$

where

r = the number of elastic unloadings from yielded conditions (r=1,2...)

$\overset{\sim}{\alpha}{}^{o}_{ij} = \overset{\gamma}{\beta}{}^{o}_{ij} = 0$

(i) indicates initiation of yielding or reyielding

(f) indicates final position prior to unloading

The yield criterion for the translated yield surface is based on the effective stress given as

$$\bar{\sigma} = [(\sigma_{11}-\overset{\sim}{\alpha}{}^{r}_{11})^2 - (\sigma_{11}-\overset{\sim}{\alpha}{}^{r}_{11})(\sigma_{22}-\overset{\sim}{\alpha}{}^{r}_{22}) + (\sigma_{22}-\overset{\sim}{\alpha}{}^{r}_{22})^2 + 3(\sigma_{12}-\overset{\sim}{\alpha}{}^{r}_{12})^2]^{1/2} \qquad (111)$$

Furthermore, it is advantageous in this analysis to relocate the origin on the $\bar{\varepsilon}$ axis after each unloading such that the extended elastic

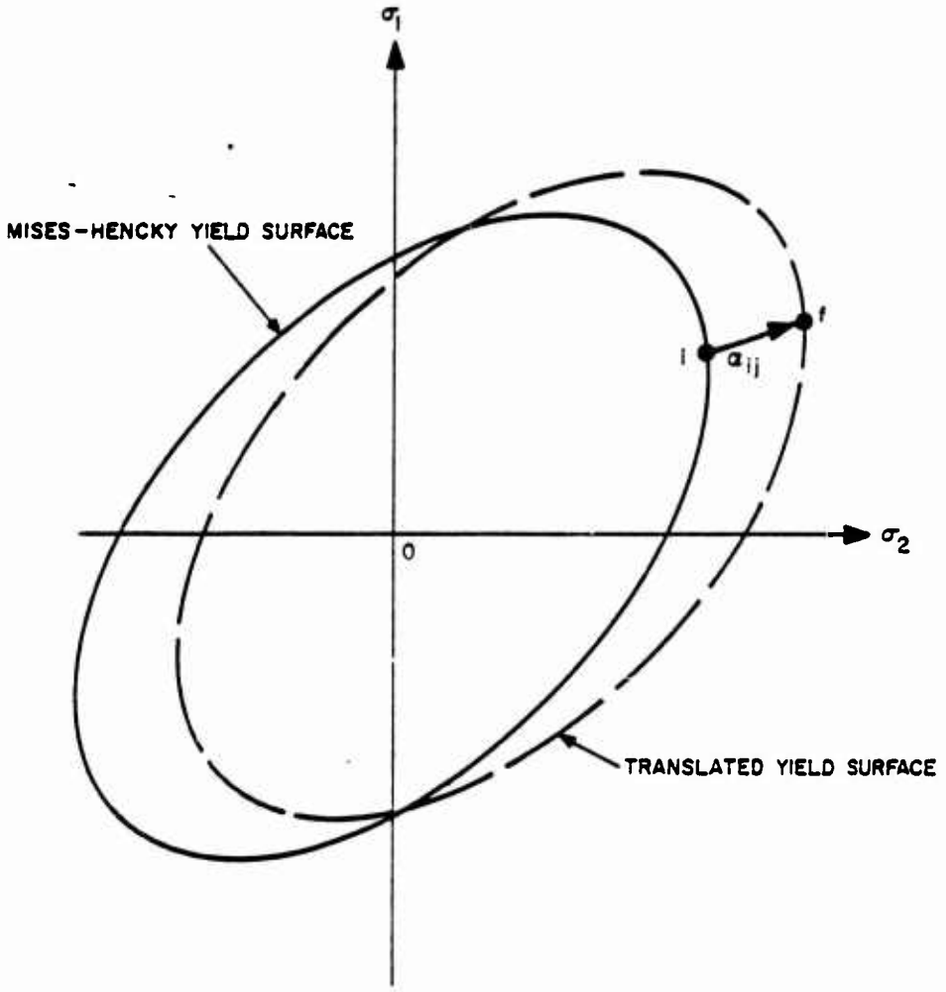

Figure 39. Kinematic Hardening Model

unloading curve passes through the zero position. This is accomplished by defining the effective strain as follows:

$$\bar{\varepsilon} = \left\{ \frac{1}{(1-\nu_s^2)^2} \left[(1-\nu_s+\nu_s^2) \left((\tilde{\varepsilon}_{11} - \tilde{\beta}^r_{11})^2 + (\tilde{\varepsilon}_{22}-\tilde{\beta}^r_{22})^2 \right) \right. \right.$$

$$\left. - (1-\nu_s+\nu_s^2)(\tilde{\varepsilon}_{11}-\tilde{\beta}^r_{11})(\tilde{\varepsilon}_{22}-\tilde{\beta}^r_{22}) \right] \qquad (112)$$

$$\left. + \frac{3}{(1+\nu_s)^2} (\tilde{\varepsilon}_{12}-\tilde{\beta}^r_{12})^2 \right\}^{1/2}$$

Thus, the elastic-plastic behavior of the material for subsequent yieldings after an unloading has occurred is always based on the same $\bar{\sigma}$ versus $\bar{\varepsilon}$ curve which originates at position (0,0). This approach requires that the stress-strain relations be modified by the $\tilde{\alpha}_{ij}$ and $\tilde{\beta}_{ij}$ quantities for unloading and reyielding conditions to account for the past stress-strain history. The general form of the stress-strain relations for the elastic, elastic-plastic, elastic unloading and plastic reyielding regions are identical, so that the general stress-strain relations based on the form of equation (108) is given by

$$\sigma_{ij} = \tilde{\alpha}^r_{ij} + \frac{E_s}{1-\nu_s^2} \left[(1-\nu_s)(\tilde{\varepsilon}_{ij}-\tilde{\beta}^r_{ij}) + \nu_s(\tilde{\varepsilon}_{kk}-\tilde{\beta}^r_{kk})\delta_{ij} \right] \qquad (113)$$

$$(i,j,k = 1,2)$$

where for the following regions of response,

a) initial elastic loading $\quad E_s=E,\ \tilde{\alpha}^r_{ij} = \tilde{\beta}^r_{ij} = 0$

b) initial plastic loading $\quad E_s=E_s,\ \tilde{\alpha}^r_{ij} = \tilde{\beta}^r_{ij} = 0$

c) qth elastic unloading $E_s = E,\ \tilde{\alpha}_{ij}^{r} = \tilde{\alpha}_{ij}^{q},\ \tilde{\beta}_{ij}^{r} = \tilde{\beta}_{ij}^{q}$

d) qth reyielding $E_s = E_s,\ \tilde{\alpha}_{ij}^{r} = \tilde{\alpha}_{ij}^{q},\ \tilde{\beta}_{ij}^{r} = \tilde{\beta}_{ij}^{q}$

Thus, there are four basic regions of response for which the stress-strain relations have been established by equation 113. For an elastic-perfectly plastic material, $E_t = 0$ and $\tilde{\alpha}_{ij}^{r}$ are set equal to zero in equations 111 and 113. It should be noted that for a strain hardening material, a stress path which may move along the yield surface (neutral loading) would not be properly represented in the analysis, since, upon unloading, the yield surface would be rigidly translated.

For elastic, isotropic or orthotropic multilayered panels, the stress-strain relation formulation follows the approach presented in reference 40. In orthotropic layers, the geometric cylindrical coordinate axes and principal orthotropic direction are assumed parallel. The multilayered cross section for the panel is shown in figure 40 with the nomenclature used in the following formulation. The position of the coordinate surface relative to the inner surface of the panel is defined by the distance $\bar{H}$. The membrane and bending stress resultants for the multilayered panel are given by

$$\tilde{\sigma}_{xx}^{m} = C_{11}\varepsilon_{xx} + C_{12}\varepsilon_{\theta\theta} + F_{11}\kappa_{xx} + F_{12}\kappa_{\theta\theta} \tag{114a}$$

$$\tilde{\sigma}_{\theta\theta}^{m} = C_{22}\varepsilon_{\theta\theta} + C_{12}\varepsilon_{xx} + F_{22}\kappa_{\theta\theta} + F_{12}\kappa_{xx} \tag{114b}$$

$$\tilde{\sigma}_{x\theta}^{m} = C_{33}\varepsilon_{x\theta} + F_{33}\kappa_{x\theta} \tag{114c}$$

$$\tilde{\sigma}_{xx}^{b} = D_{11}\kappa_{xx} + D_{12}\kappa_{\theta\theta} + F_{11}\varepsilon_{xx} + F_{12}\varepsilon_{\theta\theta} \tag{114d}$$

$$\tilde{\sigma}_{\theta\theta}^{b} = D_{22}\kappa_{\theta\theta} + D_{12}\kappa_{xx} + F_{22}\varepsilon_{\theta\theta} + F_{12}\varepsilon_{xx} \tag{114e}$$

$$\tilde{\sigma}_{x\theta}^{b} = D_{33}\kappa_{x\theta} + F_{33}\varepsilon_{x\theta} \tag{114f}$$

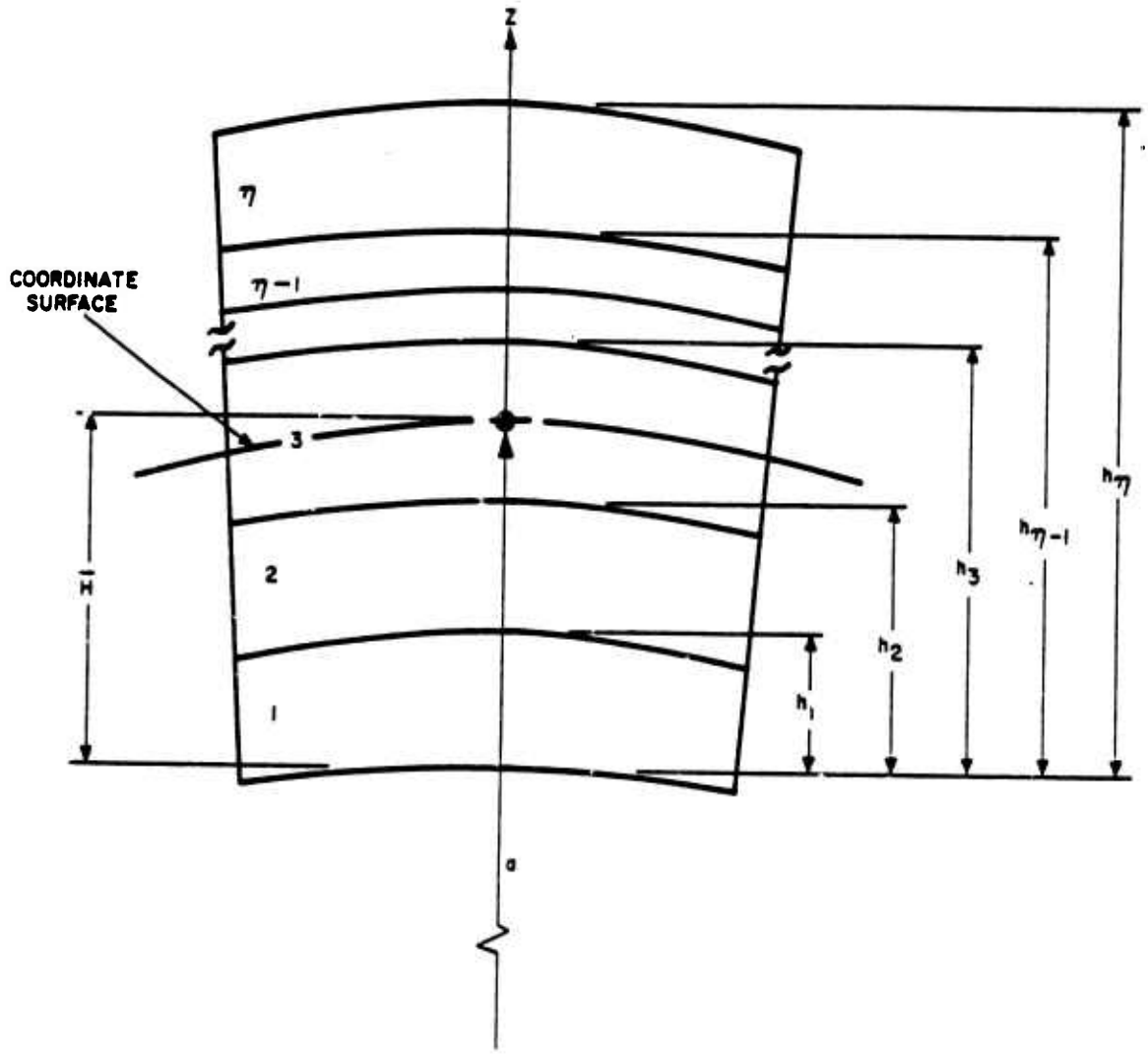

Figure 40 - Multilayered Cross Section

The elastic stiffness constants C_{ij}, F_{ij} and D_{ij} are defined by

$$C_{ij} = \sum_{k=1}^{\eta} B_{ij}^{k} \, (h_k - h_{k-1})$$

$$F_{ij} = -\frac{1}{2} \sum_{k=1}^{\eta} B_{ij}^{k} \, [(h_k^2 - h_{k-1}^2) - 2 \bar{H}(h_k - h_{k-1})]$$

$$D_{ij} = \frac{1}{3} \sum_{k=1}^{\eta} B_{ij}^{k} [(h_k^3 - h_{k-1}^3) - 3 \bar{H}(h_k^2 - h_{k-1}^2) + 3\bar{H}^2(h_k - h_{k-1})]$$

$$B_{11}^{k} = \frac{E_x^k}{1-\nu_x^k \nu_\theta^k}, \quad B_{22}^{k} = \frac{E_\theta^k}{1-\nu_x^k \nu_\theta^k}, \quad B_{33}^{k} = G_{x\theta}^{k}, \quad B_{12}^{k} = \frac{\nu_x^k E_\theta^k}{1-\nu_x^k \nu_\theta^k} = \frac{\nu_\theta^k E_x^k}{1-\nu_x^k \nu_\theta^k}$$

where

E_x^k, E_θ^k are the moduli of elasticity in the x and θ directions, respectively, of the kth layer

ν_x^k, ν_θ^k are Poisson's ratios in the x and θ directions, respectively, of the kth layer

$G_{x\theta}^k$ is the shear modulus of the kth layer

h_k is the distance from the inner shell surface to the outer surface of the kth layer

η is the total number of layers

For an isotropic material $E_x = E_\theta = E$, $\nu_x = \nu_\theta = \nu$ and $G_{x\theta} = \frac{E}{2(1+\nu)}$.

It has been found that the optimal position of the coordinate surface for the most efficient modal convergence is at the neutral axis of the cross section. When the coordinate surface is located at the neutral axis, the interaction stiffnesses F_{ij} vanish. These interaction stiffnesses reflect the influence of the change in curvature on the membrane stress resultants and the membrane strains on the bending stress resultants. As discussed in reference 40, for the general case of an antisymmetrical orthotropic multilayered cross section, a neutral axis, which is defined when all $F_{ij} = 0$, does not exist except for special combinations of elastic characteristics of the various layers. For the general case, the position of the coordinate axis, defined by $\bar{H}$, is established for this analysis by setting $F_{11} = F_{22} = F_{12} = F_{33} = 0$ to obtain the values

$$\bar{H}_{ij} = \frac{\sum_{k=1}^{n} B_{ij}^{k} \left(h_k^2 - h_{k-1}^2\right)}{2 \sum_{k=1}^{n} B_{ij}^{k} \left(h_k - h_{k-1}\right)} \tag{115}$$

and then $\bar{H}$ is determined by averaging these values as follows:

$$\bar{H} = \frac{1}{4} \left(\bar{H}_{11} + \bar{H}_{22} + \bar{H}_{12} + \bar{H}_{33}\right) \tag{116}$$

It should be noted that for cases where the neutral axis does exist, the coordinate surface is located at this position through the above procedure. When the center of mass of the cross section does not coincide with the neutral axis, a slight discrepancy in the inplane inertia would be introduced since the rotary inertia is not included in this analysis. Experimental results indicate that the rotary inertia affected the response quantities by about only 1% for a shell undergoing large displacement response.

4.2.4 Displacement Component Functions

In equation 98 the displacement components are expressed in series form as a product of time-dependent coefficients and independent spatial functions $\phi_m(x)$ and $\phi_n(\theta)$. These spatial functions are selected so as to satisfy the geometric boundary conditions of the panels. The boundaries of the panel are assumed to be either clamped or simply supported and spatial functions are defined to cover all combinations of these boundary conditions for the four edges of a panel defined by $x = 0, \ell$ and $\theta = 0, \theta_o$. On clamped edges the boundary conditions

$$w = v = u = \frac{\partial w}{\partial x} = \frac{\partial w}{\partial \epsilon} = 0$$

are to be satisfied while on simply supported edges the boundary conditions

$$w = v = u = \frac{\partial^2 w}{\partial x^2} = \frac{\partial^2 w}{\partial \theta^2} = 0$$

are to be satisfied. Since the panels are uniformly loaded, the assumed displacement functions will adhere to this symmetry. The nondimensional variables $\gamma = \frac{\pi x}{\ell}$ and $\beta = \frac{\pi \theta}{\theta_o}$ are introduced for use in this analysis. The spatial functions for the u and v displacements are assumed to be the same whether the edges are clamped or simply supported and are given by

$$\begin{aligned} \phi_m^u(\gamma) &= \sin 2m\gamma \\ \phi_n^u(\beta) &= \sin (2n-1)\beta \\ \phi_m^v(\gamma) &= \sin (2m-1)\gamma \\ \phi_n^v(\beta) &= \sin 2n\beta \end{aligned} \qquad (117)$$

The boundary combinations for the γ and β directions are based on opposite edges being both clamped, both simply supported or one clamped and one simply supported. The w-displacement functions for the γ and β directions are based on the natural vibratory mode shapes of a uniform beam with corresponding end boundary conditions. These spatial functions in the γ and β directions are given as follows for the three boundary combinations:

For clamped/clamped or clamped/simply supported

$$\phi_m^w = \cosh \frac{\lambda_m \gamma}{\pi} - \cos \frac{\lambda_m \gamma}{\pi} - \alpha_m \left(\sinh \frac{\lambda_m \gamma}{\pi} - \sin \frac{\lambda_m \gamma}{\pi} \right)$$

$$\phi_n^w = \cosh \frac{\lambda_n \beta}{\pi} - \cos \frac{\lambda_n \beta}{\pi} - \alpha_n \left(\sinh \frac{\lambda_n \beta}{\pi} - \sin \frac{\lambda_n \beta}{\pi} \right) \qquad (118)$$

where

λ_m or λ_n are the odd roots of $\cos \lambda_i \cosh \lambda_i = 1$ for the clamped/clamped boundary condition

λ_m or λ_n are the odd roots of $\tan \lambda_i = \tanh \lambda_i$ for the clamped/simply supported boundary condition

$$\alpha_i = \frac{\cosh \lambda_i - \cos \lambda_i}{\sinh \lambda_i - \sin \lambda_i}$$

i = n or m

For simply supported/simply supported

$$\phi_m^w = \sin (2m-1)\gamma$$

$$\phi_n^w = \sin (2n-1)\beta \qquad (119)$$

It should be noted that the functions given in equations 118 and 119 are orthogonal.

For the general curved panel, there are nine combinations of boundary conditions provided by the DEPROP program, namely,

	γ-direction	β-direction
1.	C-C	C-C
2.	S-S	S-S
3.	C-C	S-S
4.	S-S	C-C
5.	C-S	C-C
6.	C-C	C-S
7.	C-S	S-S
8.	S-S	C-S
9.	C-S	C-S

The first four combinations (1-4) have symmetry in both directions, the next four combinations (5-8) have nonsymmetry in one direction and combination 9 has nonsymmetry in both directions.

4.2.5 Governing Equations of Motion

With the strain-displacement relations (equations 104 and 105), the stress-strain relations (equations 113 and 114) and the displacement component functions (equations 117-119) defined, the governing equations of motion (equation 101) for elastic-plastic deformations are developed further by performing the indicated spatial integrations. For convenience, the dimensionless quantities $W = \frac{w}{a}$, $V = \frac{v}{a}$, $U = \frac{u}{a}$, $\overset{\circ}{W} = \frac{w}{a}$, $\gamma = \frac{\pi x}{\ell}$, $\beta = \frac{\pi\theta}{\theta_0}$, $L = \frac{\ell}{\pi a}$, $J = \frac{\pi}{\theta_0}$, $R = \frac{a}{h}$ and $K = \kappa a$ are introduced into the formulations. With this notation and the spatial integration for the kinetic energy in equation 103 performed analytically, the governing equations of motion in the radial displacement direction (equation 101c) are given by

$$k_\gamma k_\beta \rho \ell^2 \ddot{W}_{mn} + \frac{2L^2}{h} \int_0^\pi \int_0^\pi \int_{-h/2}^{h/2} \sigma_{ij} \frac{\partial \tilde{\varepsilon}_{ij}}{\partial W_{mn}} d\gamma d\beta dz - \int_0^\pi \int_0^\pi \tilde{Q}_w d\gamma d\beta = 0$$

$$(m=1,2,\ldots M)$$
$$(n=1,2,\ldots N) \qquad (120)$$

where for the w-equations

k_γ, $k_\beta = \sqrt{2}$ for C-C or C-S opposite boundaries

$= 1/\sqrt{2}$ for S-S opposite boundaries,

for the u and v-equations

$k_\gamma = k_\beta = 1/\sqrt{2}$

and

$$\tilde{Q}_w = 2L^2 Rp(1 - \lambda W - \lambda \mathring{W} + JV_\beta + \frac{1}{L} U_\gamma) \frac{\partial W}{\partial W_{mn}}$$

$$\tilde{Q}_v = -2L^2 Rp(JW_\beta + J\mathring{W}_\beta + \lambda V) \frac{\partial V}{\partial V_{mn}} \qquad (121)$$

$$\tilde{Q}_u = -2LRp(W_\gamma + \mathring{W}_\gamma) \frac{\partial U}{\partial U_{mn}}$$

Although equation 120 is given in terms W_{mn}, the equations of motion for the tangential and axial displacement directions can be obtained by replacing W_{mn} with V_{mn} and U_{mn}, respectively, and using the appropriate k_γ, k_β and $\tilde{Q}$ expressions.

The remaining spatial integrations in equation 120 are to be accomplished numerically thus providing a mechanism for discretization through the spatial points selected to compute the representative elastic-plastic behavior throughout the panel. Thus, a sufficient number of spatial points must be specified to obtain a satisfactory deformation response solution. For integration through the thickness of the panel in the z direction, it is convenient to separate the integrand

into parts which either are or are not explicitly dependent on the z variable, that is, involving membrane strains and bending strains. The total strain quantities $\tilde{\varepsilon}_{ij}$ given in equation 120 for an arbitrary position in the panel consist of the membrane and bending components given by

$$\tilde{\varepsilon}_{ij} = \varepsilon_{ij} + z\kappa_{ij} \tag{122}$$

Therefore, the integrand can be given by $f^m + zf^b$ where

$$f^m = \sigma_{xx} \frac{\partial \varepsilon_{xx}}{\partial W_{mn}} + \sigma_{\theta\theta} \frac{\partial \varepsilon_{\theta\theta}}{\partial W_{mn}} + \sigma_{x\theta} \frac{\partial \varepsilon_{x\theta}}{\partial W_{mn}} \tag{123a}$$

$$f^b = \sigma_{xx} \frac{\partial K_{xx}}{\partial W_{mn}} + \sigma_{\theta\theta} \frac{\partial K_{\theta\theta}}{\partial W_{mn}} + \sigma_{x\theta} \frac{\partial K_{x\theta}}{\partial W_{mn}} \tag{123b}$$

and the total stress components are obtained from equations 113 and 110 in which i,j=1 denotes x and i,j=2 denotes θ. The Legendre-Gauss quadrature formula (ref. 41) was chosen for the numerical integration in the z direction where $\bar{L}$ is the number of points selected through the thickness of the panel. In the γ and β directions it is convenient to have even spacing and it is advantageous to have spatial points on the clamped edges and at the center of the panel. Simpson's quadrature formula (ref. 41) satisfies these desirable features and therefore was selected over various Gaussian quadrature formulas. The number of spatial points selected in the γ and β directions are given by $\bar{M}$ and $\bar{N}$, respectively, where $\bar{M}$ and $\bar{N}$ must be odd numbers. By performing the indicated numerical integrations, equation 120 is recast into the form:

$$k_\gamma k_\beta \rho \ell^2 \ddot{W}_{mn} + \frac{\pi^2}{9(\bar{M}-1)(\bar{N}-1)} \sum_{j=1}^{\bar{M}} \sum_{k=1}^{\bar{N}} H_j H_k \left\{ L^2 \sum_{i=1}^{\bar{L}} H_i \left[f_i^m(\gamma_j, \beta_k) \right.\right.$$

$$\left.\left. + \frac{1}{2R} \xi_i f_i^b (\gamma_j, \beta_k) \right] - \tilde{Q}_w (\gamma_j, \beta_k) \right\} = 0 \qquad (124)$$

$$(m=1,2...M)$$
$$(n=1,2...N)$$

where

ξ_i are the zeros of the Legendre polynomial $P_{\bar{L}}(\xi)$

$$z_i = \frac{h}{2} \xi_i$$

$$H_i = \frac{2(1-\xi_i^2)}{(\bar{L}+1)^2 [P_{\bar{L}+1}(\xi_i)]^2}$$

$H_{j \text{ or } k} = 4$ (j,k = even)

$= 2$ (j,k = odd, except for j=1, $\bar{M}$ or k = 1,$\bar{N}$)

$= 1$ (j=1, $\bar{M}$ and k=1,$\bar{N}$)

$$\gamma_j = \left(\frac{j-1}{\bar{M}-1}\right) \pi$$

$$\beta_k = \left(\frac{k-1}{\bar{N}-1}\right) \pi$$

When symmetry is present in both the γ and β direction, for example, only one quarter of the panel need be considered and the spatial integration takes the form

$$4 \int_0^{\pi/2} \int_0^{\pi/2} F(\gamma,\beta)d\gamma d\beta = \frac{4\pi^2}{9(\bar{M}-1)(\bar{N}-1)} \sum_{j=1}^{\frac{\bar{M}+1}{2}} c_j H_j \sum_{k=1}^{\frac{\bar{N}+1}{2}} d_k H_k F(\gamma_j,\beta_k) \tag{125}$$

where

$$c_j = 1 \qquad j = 1, 2, \ldots \frac{\bar{M}-1}{2}$$

$$= \frac{1}{2} \qquad j = \frac{\bar{M}+1}{2}$$

$$d_k = 1 \qquad k = 1, 2, \ldots \frac{\bar{N}-1}{2}$$

$$= \frac{1}{2} \qquad k = \frac{\bar{N}+1}{2}$$

For the purely elastic solution of a panel, the integrations through the thickness can be obtained analytically, and results in the following simplification in equation 124:

$$\sum_{i=1}^{\bar{L}} H_i f_i^m = 2f^m \quad , \quad \sum_{i=1}^{\bar{L}} H_i \zeta_i f_i^b = \frac{1}{3R} \epsilon^b \tag{126}$$

where σ^m_{ij} replaces σ_{ij} in f^m (equation 123a), $\sigma_{ij}{}^b$ replaces σ_{ij} in f^b (equation 123b) and

$$\sigma^m_{ij} = \frac{E}{1-\nu^2}\left[(1-\nu)\varepsilon_{ij} + \nu\varepsilon_{kk}\delta_{ij}\right] \tag{127a}$$

$$\sigma_{ij}{}^b = \frac{E}{1-\nu^2}\left[(1-\nu)K_{ij} + \nu K_{kk}\delta_{ij}\right] \tag{127b}$$

$$(i,j,k = 1,2)$$

The quantities ε_{xx}, $\varepsilon_{\theta\theta}$ and $\varepsilon_{x\theta}$ are given by the normalized versions of equations 104 and

$$\frac{\partial \varepsilon_{xx}}{\partial U_{mn}} = \frac{1}{L}\left[\frac{\partial U_\gamma}{\partial U_{mn}} + \frac{1}{L}U_\gamma \frac{\partial U_\gamma}{\partial U_{mn}}\right] \tag{128a}$$

$$\frac{\partial \varepsilon_{xx}}{\partial V_{mn}} = \frac{1}{L^2} V_\gamma \frac{\partial V_\gamma}{\partial V_{mn}} \tag{128b}$$

$$\frac{\partial \varepsilon_{xx}}{\partial W_{mn}} = \frac{1}{L^2}\left[W_\gamma \frac{\partial W_\gamma}{\partial W_{mn}} + \overset{\circ}{W}_\gamma \frac{\partial W_\gamma}{\partial W_{mn}}\right] \tag{128c}$$

$$\frac{\partial \varepsilon_{\theta\theta}}{\partial U_{mn}} = J^2 U_\beta \frac{\partial U_\beta}{\partial U_{mn}} \tag{128d}$$

$$\frac{\partial \epsilon_{\theta\theta}}{\partial V_{mn}} = J \frac{\partial V_\beta}{\partial V_{mn}} + \lambda J W_\beta \frac{\partial V}{\partial V_{mn}} + \lambda V \frac{\partial V}{\partial V_{mn}} + J^2 V_\beta \frac{\partial V_\beta}{\partial V_{mn}} - \lambda J W \frac{\partial V_\beta}{\partial V_{mn}} \tag{128e}$$

$$\frac{\partial \epsilon_{\theta\theta}}{\partial W_{mn}} = -\lambda \frac{\partial W}{\partial W_{mn}} + J^2 W_\beta \frac{\partial W_\beta}{\partial W_{mn}} + J^2 \overset{\circ}{W}_\beta \frac{\partial W_\beta}{\partial W_{mn}} + \lambda J V \frac{\partial W_\beta}{\partial W_{mn}}$$

$$-J\lambda V_\beta \frac{\partial W}{\partial W_{mn}} + \lambda W \frac{\partial W}{\partial W_{mn}} \tag{128f}$$

$$\frac{\partial \epsilon_{x\theta}}{\partial U_{mn}} = J \frac{\partial U_\beta}{\partial U_{mn}} + \frac{J U_\beta}{L} \frac{\partial U_\gamma}{\partial U_{mn}} + \frac{J U_\gamma}{L} \frac{\partial U_\beta}{\partial U_{mn}}. \tag{128g}$$

$$\frac{\partial \epsilon_{x\theta}}{\partial V_{mn}} = \frac{1}{L}\left[\frac{\partial V_\gamma}{\partial V_{mn}} + \lambda W_\gamma \frac{\partial V}{\partial V_{mn}} + J V_\gamma \frac{\partial V_\beta}{\partial V_{mn}} + J V_\beta \frac{\partial V_\gamma}{\partial V_{mn}} - \lambda W \frac{\partial V_\gamma}{\partial V_{mn}}\right] \tag{128h}$$

$$\frac{\partial \epsilon_{x\theta}}{\partial W_{mn}} = \frac{1}{L}\left[J W_\gamma \frac{\partial W_\beta}{\partial W_{mn}} + J W_\beta \frac{\partial W_\gamma}{\partial W_{mn}} + J \overset{\circ}{W}_\gamma \frac{\partial W_\beta}{\partial W_{mn}} + J \overset{\circ}{W}_\beta \frac{\partial W_\gamma}{\partial W_{mn}}\right.$$

$$\left. + \lambda V \frac{\partial W_\gamma}{\partial W_{mn}} - \lambda V_\gamma \frac{\partial W}{\partial W_{mn}}\right] \tag{128i}$$

The quantities K_{xx}, $K_{\theta\theta}$ and $K_{x\theta}$ are given by the normalized versions of equations 105 and

$$\frac{\partial K_{xx}}{\partial U_{mn}} = \frac{1}{L^3} W_{\gamma\gamma} \frac{\partial U_\gamma}{\partial U_{mn}} \tag{129a}$$

$$\frac{\partial K_{xx}}{\partial V_{mn}} = \frac{J}{L^2} W_{\gamma\gamma} \frac{\partial V_\beta}{\partial V_{mn}} \tag{129b}$$

$$\frac{\partial K_{xx}}{\partial W_{mn}} = \frac{1}{L^2}\left(1 + JV_\beta + \frac{1}{L} U_\gamma - \lambda W\right) \frac{\partial W_{\gamma\gamma}}{\partial W_{mn}} - \frac{\lambda}{L^2} W_{\gamma\gamma} \frac{\partial W}{\partial W_{mn}} \tag{129c}$$

$$\frac{\partial K_{\theta\theta}}{\partial U_{mn}} = \lambda \frac{1}{L} \frac{\partial U_\gamma}{\partial U_{mn}} + \frac{J^2}{L} W_{\beta\beta} \frac{\partial U_\gamma}{\partial U_{mn}} \tag{129d}$$

$$\frac{\partial K_{\theta\theta}}{\partial V_{mn}} = (2\lambda J + J^3 W_{\beta\beta} + 4\lambda J^2 V_\beta - 3\lambda JW) \frac{\partial V_\beta}{\partial V_{mn}} + \lambda(3JW_\beta + 2V) \frac{\partial V}{\partial V_{mn}} \tag{129e}$$

$$\frac{\partial K_{\theta\theta}}{\partial W_{mn}} = \left(J^2 + J^3 V_\beta - \lambda J^2 W + \frac{J^2}{L} U_\gamma\right) \frac{\partial W_{\beta\beta}}{\partial W_{mn}} + (-\lambda + 2\lambda W - 3\lambda JV_\beta - \lambda J^2 W_{\beta\beta}) \frac{\partial W}{\partial W_{mn}} + \lambda(4J^2 W_\beta + 3JV) \frac{\partial W_\beta}{\partial W_{mn}} \tag{129f}$$

$$\frac{\partial K_{x\theta}}{\partial U_{mn}} = \frac{2J}{L^2} W_{\gamma\beta} \frac{\partial U_\gamma}{\partial U_{mn}} \tag{129g}$$

$$\frac{\partial K_{x\theta}}{\partial V_{mn}} = \lambda \frac{1}{L} \frac{\partial V_\gamma}{\partial V_{mn}} + \frac{2J^2}{L} W_{\gamma\beta} \frac{\partial V_\beta}{\partial V_{mn}} + \frac{2\lambda}{L} W_\gamma \frac{\partial V}{\partial V_{mn}} \tag{129h}$$

$$\frac{\partial K_{x\theta}}{\partial W_{mn}} = \frac{2J}{L}\left(1 + JV_{\beta} + \frac{1}{L}U_{\gamma} - \lambda W\right)\frac{\partial W_{\gamma\beta}}{\partial W_{mn}} - \frac{2\lambda J}{L}W_{\gamma\beta}\frac{\partial W}{\partial W_{mn}}$$

$$+ \frac{2\lambda}{L}(JW_{\beta} + V)\frac{\partial W_{\gamma}}{\partial W_{mn}} + \frac{2\lambda J}{L}W_{\gamma}\frac{\partial W_{\beta}}{\partial W_{mn}} \qquad (129i)$$

For the elastic response solution of multilayered panels, the same formulation is used with several modifications. The stiffness constants in equation 114, C_{ij}, F_{ij} and D_{ij}, are considered to have been divided by a, a^2 and a^3, respectively, and $R = a/h_{\eta}$. In equation 124, ρ is replaced by $\bar{\rho}$ given by

$$\bar{\rho} = \frac{1}{h_{\eta}}\sum_{k=1}^{\eta}\rho_k\,(h_k - h_{k-1})$$

and

$$\sum_{i=1}^{\bar{L}} H_i f_i^m = 2Rf^{\cdot}$$

$$\sum_{i=1}^{\bar{L}} H_i \xi_i f_i^b = 4R^2 f^b$$

The $\tilde{\sigma}^m$ and $\tilde{\sigma}^b$ quantities given in equation 114 replace the appropriate total stress quantities given in equation 123. With these modifications in DEPROP, elastic response solutions can be obtained for multilayered panels of isotropic or orthotropic material layers.

4.2.6 Numerical Analysis

The second-order differential equations given by equation 124 and corresponding equations for V_{mn} and U_{mn} are to be solved numerically in time. The integration method used to obtain an approximate timewise step-by-step solution is based on the central difference formula given by

$$X_{k+1} = \ddot{X}_k (\Delta t)^2 + 2X_k - X_{k-1} \tag{130}$$

where

X represents the normalized undetermined time-dependent displacement coefficients, W_{mn}, V_{mn} and U_{mn}

Δt is the time increment

k denotes the time step

This central-difference method replaces the higher order integration method used in the DEPROP program in reference 1. The central-difference method permits a time increment about 50% greater than the previous higher order integration method without any significant change (less than 1%) in the response solution for the panel problems considered. The starting procedure used for this method is the same as that presented in subsection 4.1.10.

In solving the set of simultaneous second-order differential equations, spatial integrations must be performed in the γ and β directions and in the z direction for the elastic-plastic solution during the stepwise time integration. The required integrations are performed numerically during each time step using the values of the displacement coefficients W_{mn}, V_{mn} and U_{mn} for the particular time step to compute the displacements and their derivatives, the strain quantities and the stress quantities used in equation 124.

Several situations arise in the implementation of the biaxial elastic-plastic theory in DEPROP which require special numerical treatment. These situations are associated with the overshoot during the time increment in which yielding occurs, the criteria for determining elastic unloading and restrictions if unloading is followed by immediate reyielding, and the consistent determination of $\bar{\varepsilon}$, E_s, ν_s and σ_{ij} during each time step. The special numerical schemes used to treat these three situations are described briefly in the following three paragraphs, respectively.

Whenever a point in the panel yields or reyields during a time increment ($\bar{\sigma} > \sigma_o$), the stresses cannot, in general, be computed on a purely elastic basis. The computation of stresses should follow the bilinear stress-strain curve; but this is very difficult to effect since $\bar{\sigma}$ is not a linear function of the σ_{ij}'s. Instead, an iterative scheme is employed to adjust the σ_{ij}'s proportionately, so that $\bar{\sigma} \doteq \sigma_o$. By elastic relations, the associated strains ε_{ij} (σ_{ij}) are then determined for the later computation of $\hat{\beta}_{ij}$ (equation 120). The process for correcting for overshoot when yielding occurs between times t_{k-1} and t_k is illustrated in figure 41. The values of $\bar{\varepsilon}$ and $\bar{\sigma}$ are shown at time t_{k-1}; the values indicated at t_k represent hypothetical uncorrected values. By linearly adjusting the stresses, the point ($\bar{\varepsilon}_o$, $\bar{\sigma}_o$) is reached. It is noted that the actual point at time t_k should be ($\bar{\varepsilon}_k$, $\bar{\sigma}_A$) instead of ($\bar{\varepsilon}_k$, $\bar{\sigma}_o$), but the error in stress is relatively small since $E_t/E \ll 1$. The error introduced is proportional to the size of the integration time step used.

For a point in the panel which is yielding at time t_{k-1}, elastic unloading is detected when, in proceeding to the next time t_k, the equivalent strain decreases, i.e., $\bar{\varepsilon}_k < \bar{\varepsilon}_{k-1}$. When this occurs, $\bar{\varepsilon}_k$ and $\bar{\sigma}_k$ are recomputed using the elastic unloading version of equation 113. Furthermore, unless $\bar{\sigma}_k$ is less than $\bar{\sigma}_{k-1}$, it is assumed that the point did not unload. This possible inconsistency is partially numerical in nature, and is partially due to the nonlinearity of the equations

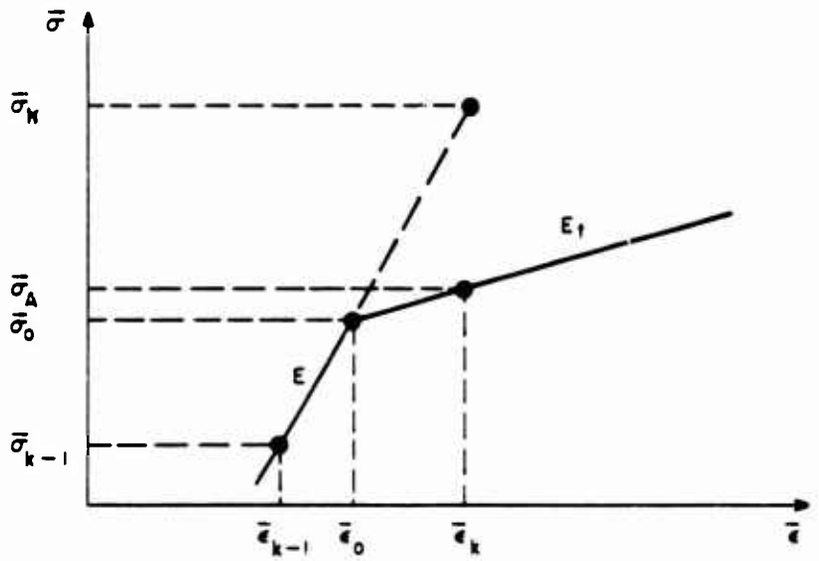

Figure 41. Correction for Overshoot at Yielding

111 or 112. However, only rarely will a point pass the strain criterion for unloading but fail the stress criterion. Due to numerical discrepancies, it is possible for the computed $\bar{\sigma}_k$ in the unloading region to be greater than σ_o at time t_k. This inconsistency results in reyielding without any overshoot correction being made. In fact, this event represents a numerical error and is usually associated with the initial stages of numerical instability of the solution. Consequently, if this event frequently occurs, the run is automatically terminated and a smaller time increment must be selected.

In the temporal integration sequence, the displacement coefficients are computed for the end of the next time step at t_{k+1} through the central-difference formula (equation 130) given the past displacement coefficients at t_k and t_{k-1} and the acceleration at t_k. These extrapolated displacement coefficients are then used to compute ε_{ij} at t_{k+1}. Then, for points in the plastic region, the quantities $\bar{\sigma}$, E_s and ν_s are

evaluated in order to compute σ_{ij} at t_{k+1}. However, $\bar{\varepsilon}$ is dependent on ν_s (equation 112), E_s is dependent on $\bar{\varepsilon}$ (equation 106), ν_s is dependent on E_s (equation 108), and σ_{ij} is dependent on E_s and ν_s (equation 113). Thus, a simple iteration scheme is used to simultaneously solve for the three parameters $\bar{\varepsilon}$, E_s and ν_s, so that a consistent determination of σ_{ij} can be made at t_{k+1}. Then, with the displacements, their derivatives, ε_{ij} and σ_{ij}, all determined at t_{k+1}, the accelerations are computed at t_{k+1} through equation 124 and the whole process is then repeated for the next time step.

A method has been established for estimating time increments Δt for the temporal integration that would result in stable solutions for the majority of panel cases. The proper time increment is a function of geometric and physical properties of flat or curved panels and, for the DEPROP formulation, also a function of the number of modes used and the spacing between spatial integration points. The method for estimating time increments is based on formulas for the higher vibratory frequencies of linear elastic panels which incorporate the aforementioned parameters. The basic frequency formulas for single-layered flat and curved panels were obtained from references 42 and 43 and modified for multilayered panels. The time increment is estimated by the product of the reciprocal of the frequency and an arbitrary adjustment factor. For both threshold of permanent and catastrophic damage levels, the panel response is nonlinear so that the arbitrary adjustment factors are determined by back-figuring from the time increments found to give stable solutions for various representative panels. In some panel cases considered where the spacing between integration points was critical for numerical stability, it was found that the Δt formula used in reference 44 for finite difference solutions is applicable. This formula is based on the time for an inplane elastic wave to propagate between mesh points.

For flat panels the governing time increment used as the initial estimate for Δt in DEPROP solutions is the smaller Δt obtained from the

following two formulas. The first formula is associated with the highest solution frequency of a flat panel with inplane stresses which are assumed to be at a level corresponding to yield or ultimate stress of the panel material and is given by

$$\Delta t_1 = \frac{\pi}{25}\left\{\frac{D_{22}\lambda_{mn}^2}{\sum_{k=1}^{n}\rho_k\,(h_k-h_{k-1})} + \frac{\sum_{k=1}^{n}\sigma_{max}(h_k-h_{k-1})}{\sum_{k=1}^{n}\rho_k\,(h_k-h_{k-1})}\,\lambda_{mn}\right\}^{-1/2} \tag{131}$$

where

$$\lambda_{mn} = \left(\frac{\bar{m}\pi}{\ell}\right)^2 + \left(\frac{\bar{n}\pi}{b}\right)^2$$

σ_{max} = yield or ultimate stress

$\bar{m}$ = 2m-1+c

$\bar{n}$ = 2n-1+c

and c=0, 0.15 and 0.3 for S-S, S-C and C-C boundary conditions, respectively.

The second formula is associated with the elastic wave propagation between integration points in the short direction and is given by

$$\Delta t_2 = \frac{b}{\bar{N}-1}\left[\frac{\sum_{k=1}^{n}\rho_k\,(h_k-h_{k-1})}{C_{22}}\right]^{1/2} \tag{132}$$

For curved cylindrical panels the smallest Δt obtained from five formulas is used for the initial estimate for DEPROP solutions. The first two formulas are associated with high frequency modes of cylindrical shells and are given by

$$\Delta t_1 = \frac{\pi a}{35}\left[\frac{\sum_{k=1}^{n}\rho_k(h_k-h_{k-1})}{C_{22}}\right]^{1/2}\left(\frac{1+\bar{\lambda}^2}{2}-\frac{1}{2}\left[(1-\bar{\lambda}^2)+4\nu^2\bar{\lambda}^2\right]^{1/2}\right)^{-1/2} \tag{133}$$

$$\Delta t_2 = \frac{\pi a}{35}\left\{\frac{D_{22}(\bar{k}^2+\bar{\lambda}^2)^2}{a^2\sum_{k=1}^{n}\rho_k(h_k-h_{k-1})}+\frac{\bar{\lambda}^4 C_{22}}{(\bar{k}^2+\bar{\lambda}^2)^2\sum_{k=1}^{n}\rho_k(h_k-h_{k-1})}\right\}^{-1/2} \tag{134}$$

where

$$\bar{\lambda} = \frac{\bar{m}\pi a}{\ell}$$

$$\bar{k} = \frac{\bar{n}\pi}{\vartheta_o}$$

The third formula is associated with the elastic wave propagation between integration points in the ϑ-direction and is given by

$$\Delta t_3 = \frac{a\theta_o}{\bar{N}-1}\left[\frac{\sum_{k=1}^{n}\rho_k(h_k-h_{k-1})}{C_{22}}\right]^{1/2} \qquad (135)$$

In cases where the length of the panel in the x-direction is much shorter than the arc length in the θ-direction, it was found that the flat panel formulas were more applicable than the above three formulas. Thus, the fourth and fifth formulas used are based on equations 131 and 132 with changing D_{22} to D_{11} and b to $a\theta_o$ in equation 131, and b to $\ell, \bar{N}$ to $\bar{M}$ and C_{22} to C_{11} in equation 132.

The smallest time increment obtained from the modified formulas used for either flat or curved panels represents an estimated value that will generally give a stable solution, but does not necessarily represent an optimal value for minimizing computer time. If a stable solution is obtained with this estimated time increment, the time increment can be increased until two consecutive solutions disagree significantly and the penultimate time increment selected for future computer time optimization, if desired. If the solution diverges using the initial estimated time increment from the formula procedure, halving the time increment should easily result in a solution in the stable range. The DEPROP program provides the option of automatically using the above estimated time increment or having the user select a value.

4.2.7 Preload Static Solution

To account for the steady-state airloads on the panel prior to the blast encounter, the displacement components (u,v,w) are determined for a uniform static pressure load (p_o). These displacements are used as the initial values to start the dynamic solution for the transient blast pressure. The static displacements are obtained from all the equations of motion of the form given in equation 124 by a relaxation

technique that permits a solution of these nonlinear equations by iteratively reducing their residuals to zero. In the case of the equation of motion, the residuals represent the accelerations in the u,v, and w directions. The initial trial values of zero for the modal displacement coefficients u_{mn}, v_{mn}, w_{mn} are used to start the relaxation procedure.

4.2.8 Approximate Solution for Elastic-Plastic Response of Sandwich Panels

The elastic-plastic option of DEPROP is limited to handling single-layered isotropic panels, so that a three-layered isotropic sandwich panel is reduced within the program to an equivalent single-layered panel based on equating corresponding extensional and bending stiffnesses. A sandwich panel with face sheets of the same material described by σ_o, ε_o, E and E_t, can be reduced to an equivalent single-layered panel defined by the following quantities in terms of the nomenclature of figure 40:

$$h_e = \frac{(h_3 + h_2 - h_1)}{(h_3 - h_2 + h_1)} \left[3h_1(h_3 - h_2)\right]^{1/2} \tag{136a}$$

$$E_e = \frac{E(h_3 - h_2 + h_1)}{h_e} \tag{136b}$$

$$\sigma_o^e = E_e \varepsilon_o \tag{136c}$$

$$E_t^e = \frac{E_t(h_3 - h_2 + h_1)}{h_e} \tag{136d}$$

$$\sigma_e = \frac{1}{h_e} \sum_{k=1}^{3} \sigma_k (h_k - h_{k-1}) \tag{136e}$$

where

h_e = equivalent thickness

E = elastic modulus of face sheets (equal to σ_o/ε_o)

E_e = equivalent elastic modulus

E_t = strain hardening modulus of face sheets

E_t^e = equivalent strain hardening modulus

ρ_e = equivalent mass density

σ_o^e = equivalent yield stress

4.2.9 Initial Panel Imperfections

There are initial geometric imperfections in actual panels on an aircraft which should be considered when a panel is being analyzed to determine the threshold of permanent damage. Generally, initial deviations from the cylindrical shape are either not specified or simply not known during flight conditions. The displacements and stresses induced in cylindrical panels may be sensitive to these imperfections depending on their amplitude and shape as indicated in reference 34 for the full cylindrical shell. If initial radial imperfection data are available or a nominal amount is specified as an approximation, such data can be included in the analysis in the form of modal imperfection coefficients, Δ_{mn} (reference equation 99).

4.2.10 DEPROP Response Comparisons with Experiment and the PETROS-3 Structural Code

To evaluate the predictive capabilities of DEPROP, the calculated displacement and strain responses are compared with available experimental results (ref. 45) and with results generated from the finite difference structural code PETROS-3 (ref. 46). The scope of

these comparisons is not extensive enough to result in a conclusive evaluation of DEPROP, but does provide an initial evaluation of DEPROP response relative to available experimental data and another structural code based on a different type of solution technique. For these comparison applications the DEPROP routine of NOVA was temporarily mated to an existing pressure loading routine from Kaman AviDyne's computer program library. This special loading routine included pressure time histories with linear and exponential decaying functions which were used as transient loadings for the DEPROP response comparisons with experiment and the PETROS-3 structural code.

Some shock-tube test data were available for panels from tests performed at the Armament Laboratory at Eglin Air Force Base and are given in reference 45. The tests at Eglin essentially consisted of exposing clamped square panels to a blast from a disposable gas-bag shock tube. The flat panels were subjected to load levels that produced large permanent deformation and, in some cases, rupture of the material along the clamped edges. Primarily, only the permanent sets of the deformed plates were measured and in a few tests the deflection patterns were measured by Moire fringe photography. Strain measurements were not obtained for these tests. The square flat panels are 18 in. by 18 in. and analytical and experimental comparisons are made for plate thicknesses of 0 063 in. and 0.071 in. The panel material is 2024-T3 aluminum for which a typical stress-strain curve is shown in figure 42 by the solid curve. The bilinear representation of this stress-strain curve used in DEPROP is given by the dashed lines and corresponds to a yield stress of 50,000 psi and a strain hardening slope of 1.24×10^5 psi. The geometric and physical properties of these plates are summarized in table 12. Pressure measurements were obtained from an instrumented rigid panel tested separately under essentially the same loading as the test panels. These pressure data were used to determine an approximate analytical fit in reference 45 using a uniform spatial distribution with the temporal decay given by

$$p(t) = p_m (1 - t/\tau) e^{-\frac{\alpha t}{\tau}} \qquad (137)$$

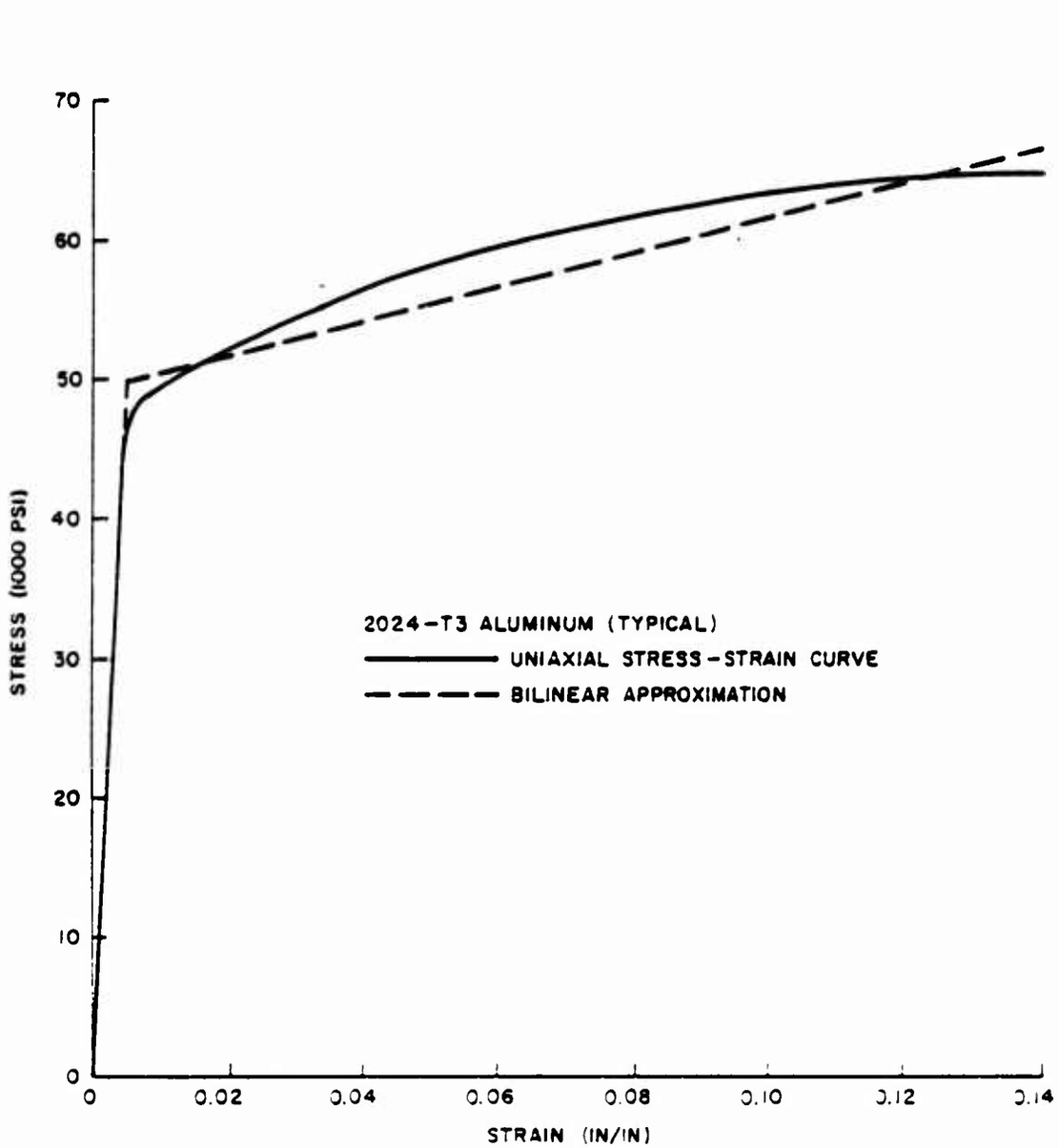

Figure 42. Stress-Strain Representation for 2024-T3 Aluminum

TABLE 12

GEOMETRIC AND PHYSICAL PROPERTIES OF PANELS

Property of Panel	Eglin Tests Comparisons	PETROS-3 Comparisons
Length (in.)	18	20 (Flat Panel)
Width (in.)	18	20 (Flat Panel)
Radius (in.)		100 (Curved Panel)
Subtended Angle (Deg)		11.48 (Curved Panel)
Thickness (in.)	0.063 and 0.071	0.1
Modulus of Elasticity (psi)	10.5×10^6	10^7
Poisson's Ratio	0.33	0.3
Mass Density $\left(\frac{\text{lb-sec}^2}{\text{in}^4}\right)$	0.259×10^{-3}	0.259×10^{-3}
Yield Stress (psi)	50,000	40,000
Strain Hardening Slope (psi)	1.24×10^5	0 and 1.5×10^5

where

p_m = 600 psi

α = 5.7

τ = 1.5 msec

The DEPROP panel routine with the special loading routine was exercised for two test cases (panel thicknesses of 0.063 and 0.071 in.) and the predicted permanent sets compared with the test measurements. The DEPROP solutions employed 25 modes selected from a 7x7 array, a 15x15 spatial integration net over the quarter panel, and five integration points through the thickness. The 0.063-in.-thick panel underwent severe plastic deformations and was considered to be near the threshold of rupture, although it did not fail. Figure 43 illustrates the analytically determined center displacement time history for the 0.063-in. panel. This figure shows an analytical maximum displacement of 3.43 in. and a permanent set of about 3.1 in. comparing closely with the experimental permanent set of 3.0 in. Figure 44 illustrates the deflection shape of the panel at various times during the response. The changing shape pattern predicted by DEPROP corresponds favorably with that observed experimentally through the Moire fringe technique and the final permanent shape. Figure 45 shows the inner and outer surface strain near the center of the panel where the maximum analytical strain occurred. The maximum analytical tensile strain is 0.133 in./in. and the strain behavior across the thickness of the plate at this position is strongly membrane. It should be noted that the maximum tensile strain probably occurs at the center of the clamped edge, but the number of modes used analytically are not sufficient to predict the edge strain accurately. The fracture strain for this material is about 0.15 in./in. and, since this panel did not rupture the edge strain, is probably not much greater than the strain near the center of the plate. For the 0.071-in. panel, figure 46 shows the analytically determined center displacement time history. Two panels of this thickness were tested experimentally and the closeness of the two permanent sets at 2.7 and 2.8 in. indicated good repeatability of the experiment. Figure 46

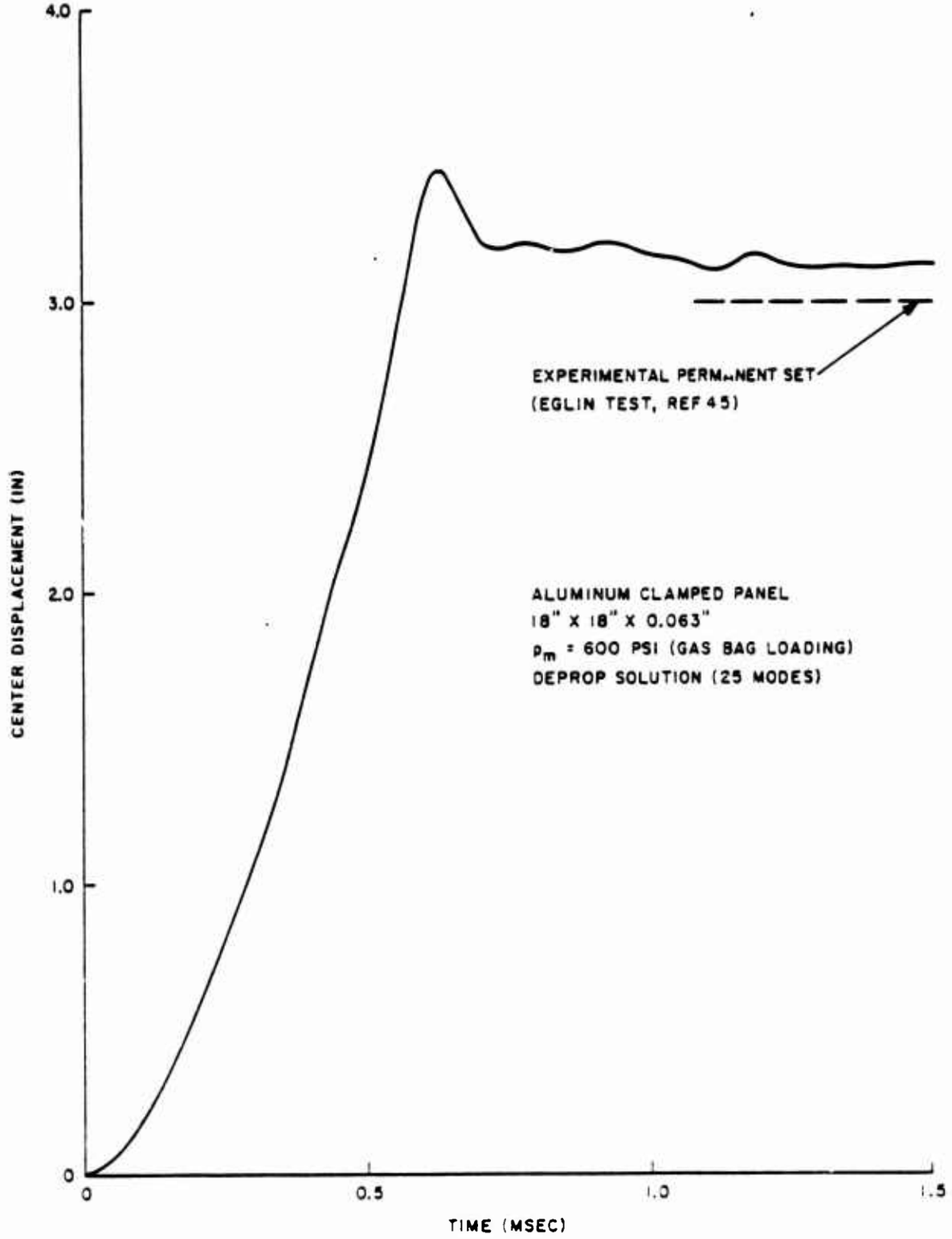

Figure 43. Center Displacement Response from DEPROP of the 0.063 Inch Eglin Test Panel

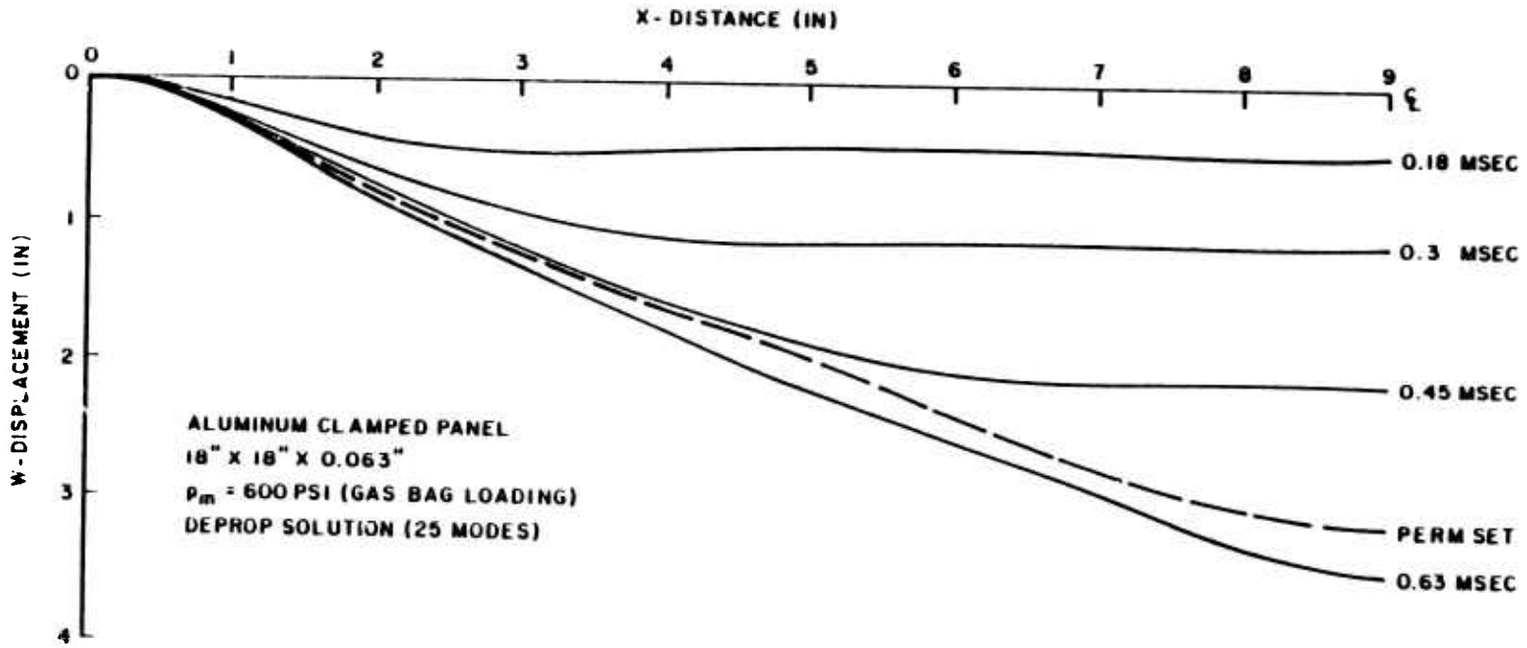

Figure 44. DEPROP Deformed Shapes of the 0.063 Inch Eglin Test Panel at Various Times

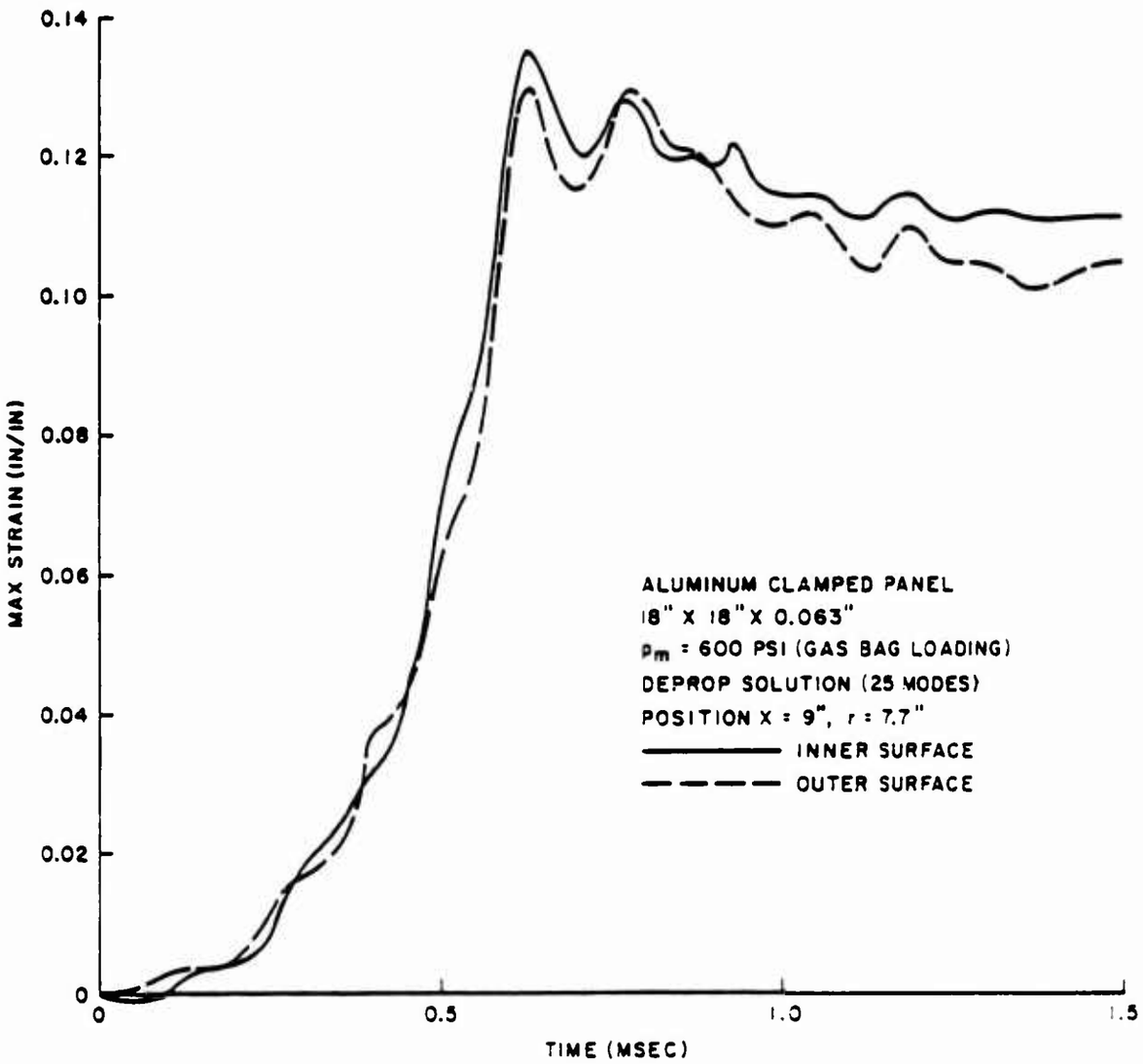

Figure 45. Maximum Strain Response from DEPROP of the [illegible] Test Panel

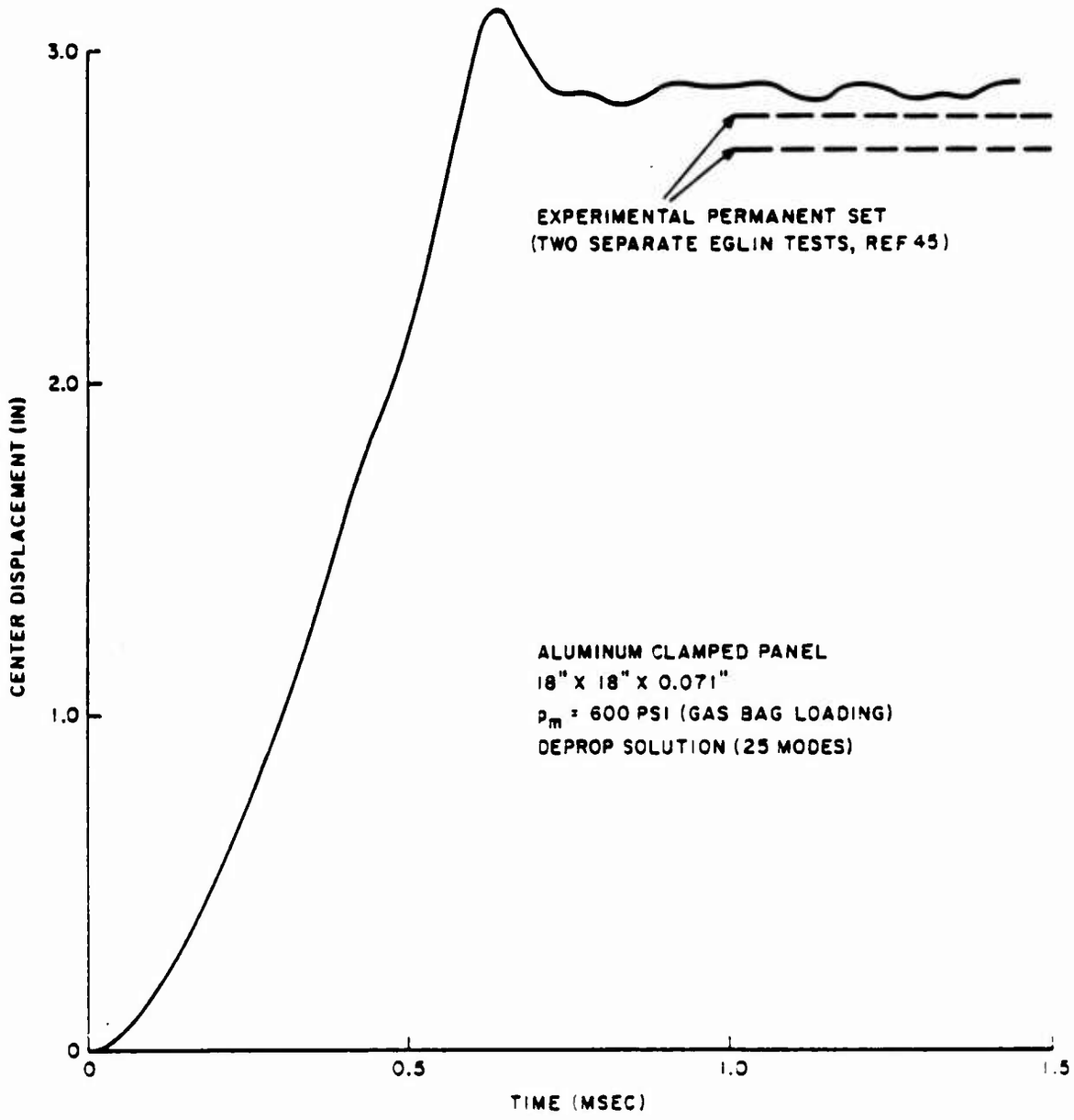

Figure 46. Center Displacement Response from DEPROP of the 0.071 Inch Eglin Test Panel

indicates that DEPROP predicts a permanent set of about 2.85 in. which compares well with the experimental values. The differences in the analytical and experimental permanent set values for the two test plates considered are less than 4%.

Comparisons of displacement and strain responses from DEPROP with PETROS-3 are made for various panels subjected to a simple transient pressure loading. PETROS-3 (ref. 44) is a dynamic response structural code for the calculation of large elastic-plastic deformations of plates and shells based on the finite-difference method of solution. While DEPROP is based on a modal type solution, there are several similarities between the numerical methods used in DEPROP and PETROS-3. Both codes use the same temporal numerical method (central-difference) and the same Gaussian integration technique through the thickness of the panel for elastic-plastic solutions. It should be noted that neither DEPROP nor PETROS-3 can be considered as an absolute standard in these comparisons. Which solution is more accurate in computing displacement and strain quantities within a panel can only be determined by thorough correlation with well controlled experiments. Solutions obtained using DEPROP and PETROS-3 were based on the respective mode or mesh limits presently dimensioned in each program for reasonable computer running times and core size on the CDC 6600 computer. Thus, the solutions are not necessarily optimal relative to complete convergence of strain quantities throughout the panels. For example, neither the number of modes used in the DEPROP solutions nor the finite-difference mesh size used in the PETROS-3 solutions are sufficient to determine accurately the strains at the clamped edges of a panel undergoing large plastic deformations where large strain gradients exist very near the edge. For this reason, only comparisons are made with center strains of the panels. For all the panel solutions using DEPROP and PETROS-3, an adequate time increment was selected so that numerical convergence was achieved on a temporal basis and the same number of integration points through the thickness was used in both code solutions. The panel problems selected were all symmetrical so that only one quarter of the panel was considered in all solutions. For DEPROP solutions, 25 modes were selected

from a 7x7 array and a 15x15 spatial integration net was used on the quarter panel. For PETROS-3 solutions, a uniform finite-difference mesh of 16x16 on the quarter panel was modified by halving the mesh size near the center and edges of the panel to produce a nonuniform 20x20 mesh. Comparisons of center displacement and strain responses from DEPROP and PETROS-3 were made for simply supported and clamped 20 in. x 20 in. x 0.1 in. square panels with purely elastic, elastic-perfectly plastic and elastic-strain hardening materials. A clamped rectangular panel and a clamped cylindrical panel, both with material strain hardening, were also used for the response comparisons. The geometric and physical properties of the various panels are summarized in table 12. Through the special loading routine, these panels were subjected to a uniform pressure loading with a triangular pulse shape that instantaneously rose to the peak pressure at zero time and decayed to zero pressure at 2 msec.

The DEPROP and PETROS-3 comparisons of center displacement and strain responses for various material conditions are shown in figures 47 through 52 for the simply supported square panels at a peak pressure of 200 psi; in figures 53 through 59 for the clamped square panels at peak pressures of 250 psi (elastic-plastic solutions) and 100 psi (purely elastic solution); in figures 60 and 61 for the clamped rectangular panel (aspect ratio of 1.5) at a peak pressure of 250 psi; and in figures 62 through 64 for the clamped cylindrical panel at a peak pressure of 250 psi. From these comparisons of DEPROP and PETROS-3 responses, the following observations are made:

1. The comparisons for purely elastic large displacement response of a square clamped panel (figures 53 and 54) show satisfactory agreement between DEPROP and PETROS-3 for both center displacements and strains.

2. For large elastic-plastic deformations of these panels, the comparisons indicate that the best agreement (magnitude differences less than 5%) occurs for all center displacement responses

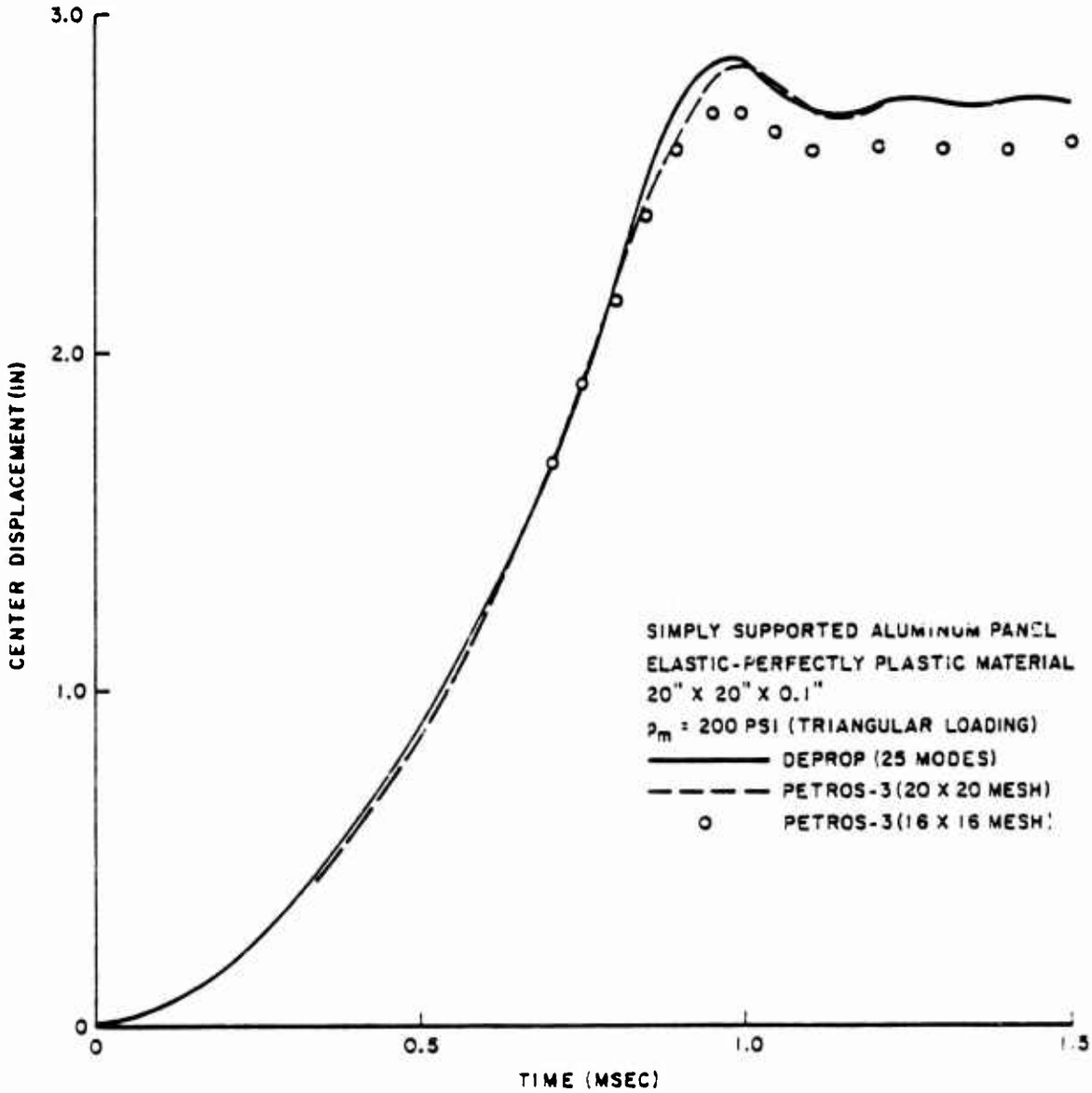

Figure 47. Comparison of DEPROP and PETROS-3 Displacement Response for Simply Supported Panel with Elastic-Perfectly Plastic Material

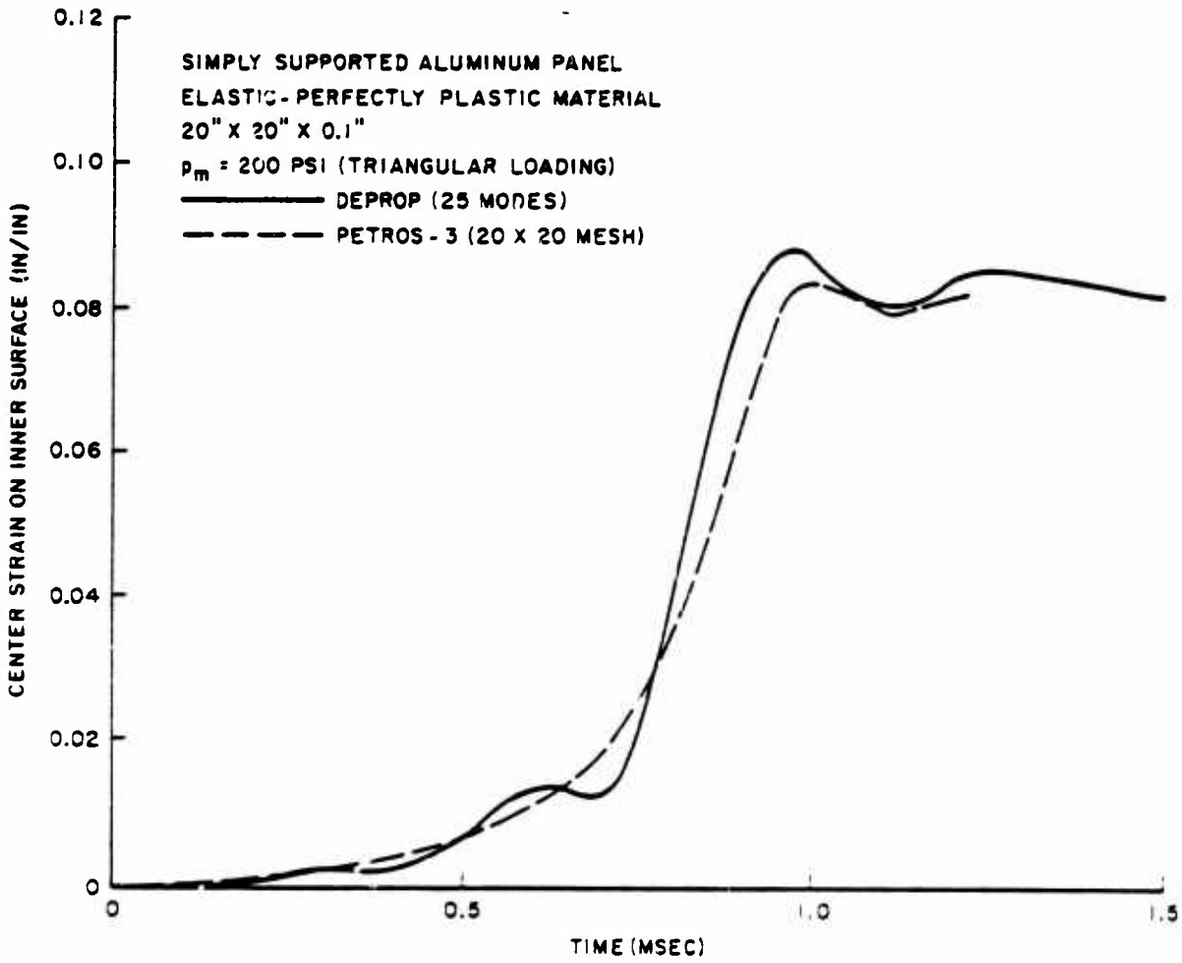

Figure 48. Comparison of DEPROP and PETROS-3 Inner Strain Response for Simply Supported Panel with Elastic-Perfectly Plastic Material

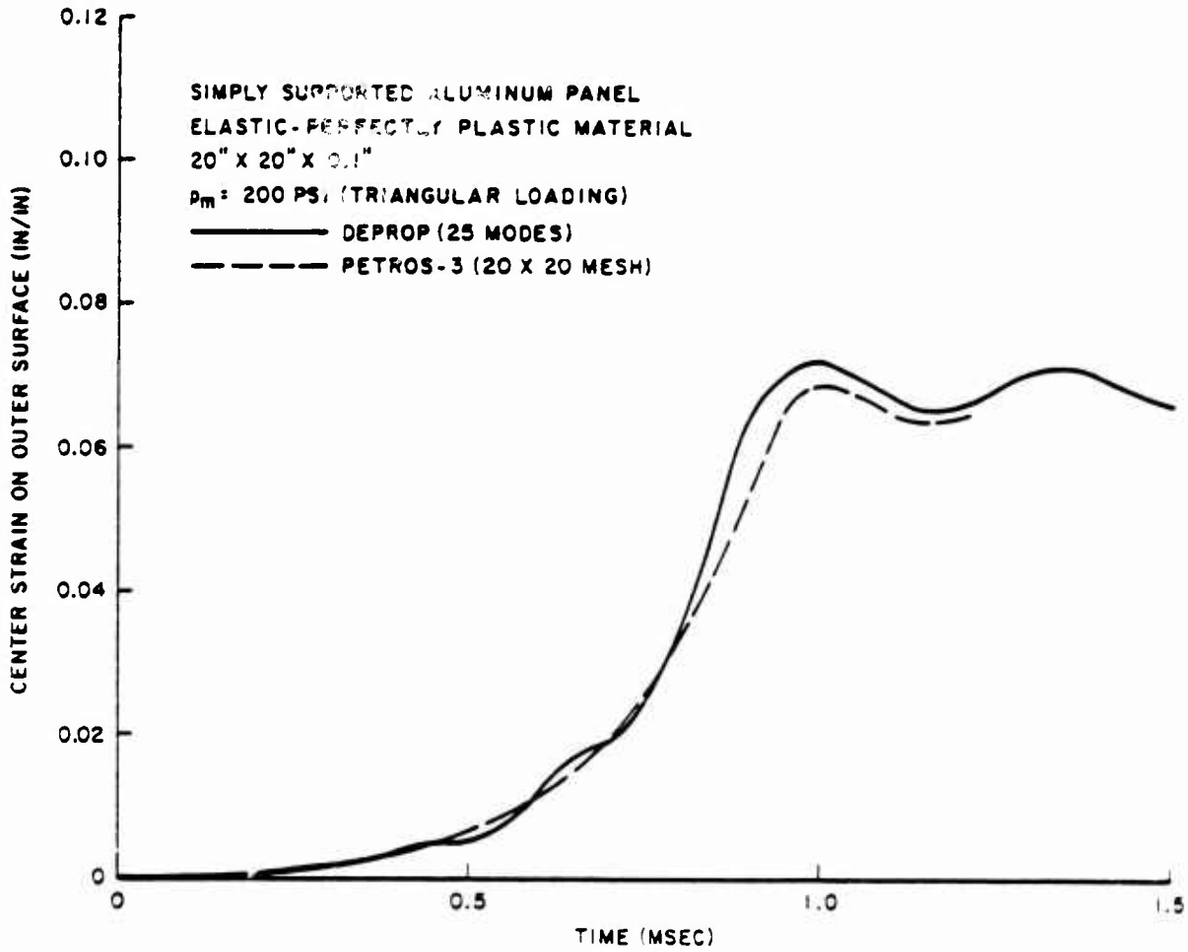

Figure 49. Comparison of DEPROP and PETROS-3 Outer Strain Response for Simply Supported Panel with Elastic-Perfectly Plastic Material

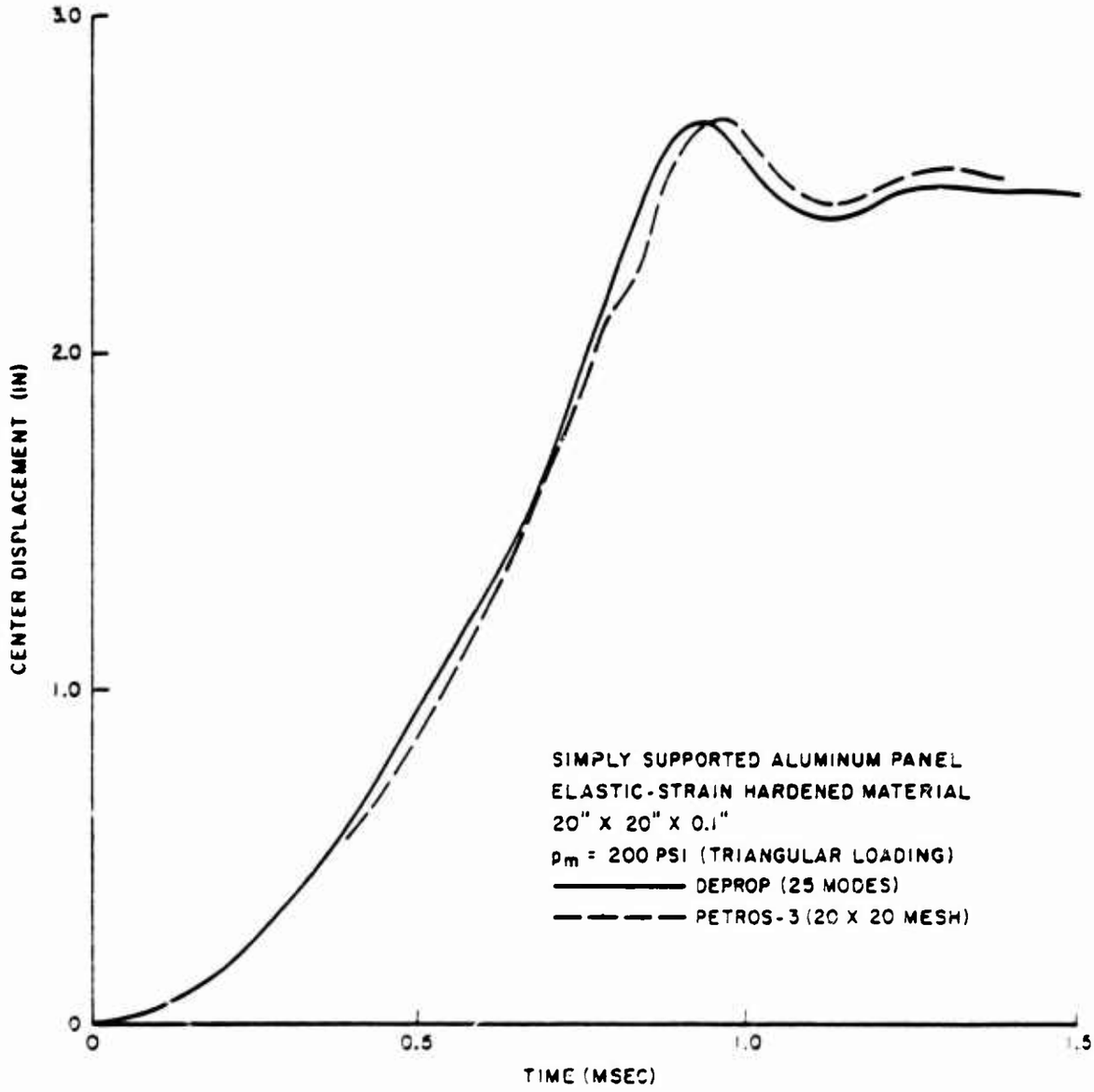

Figure 50. Comparison of DEPROP and PETROS-3 Displacement Response for Simply Supported Panel with Elastic-Strain Hardened Material

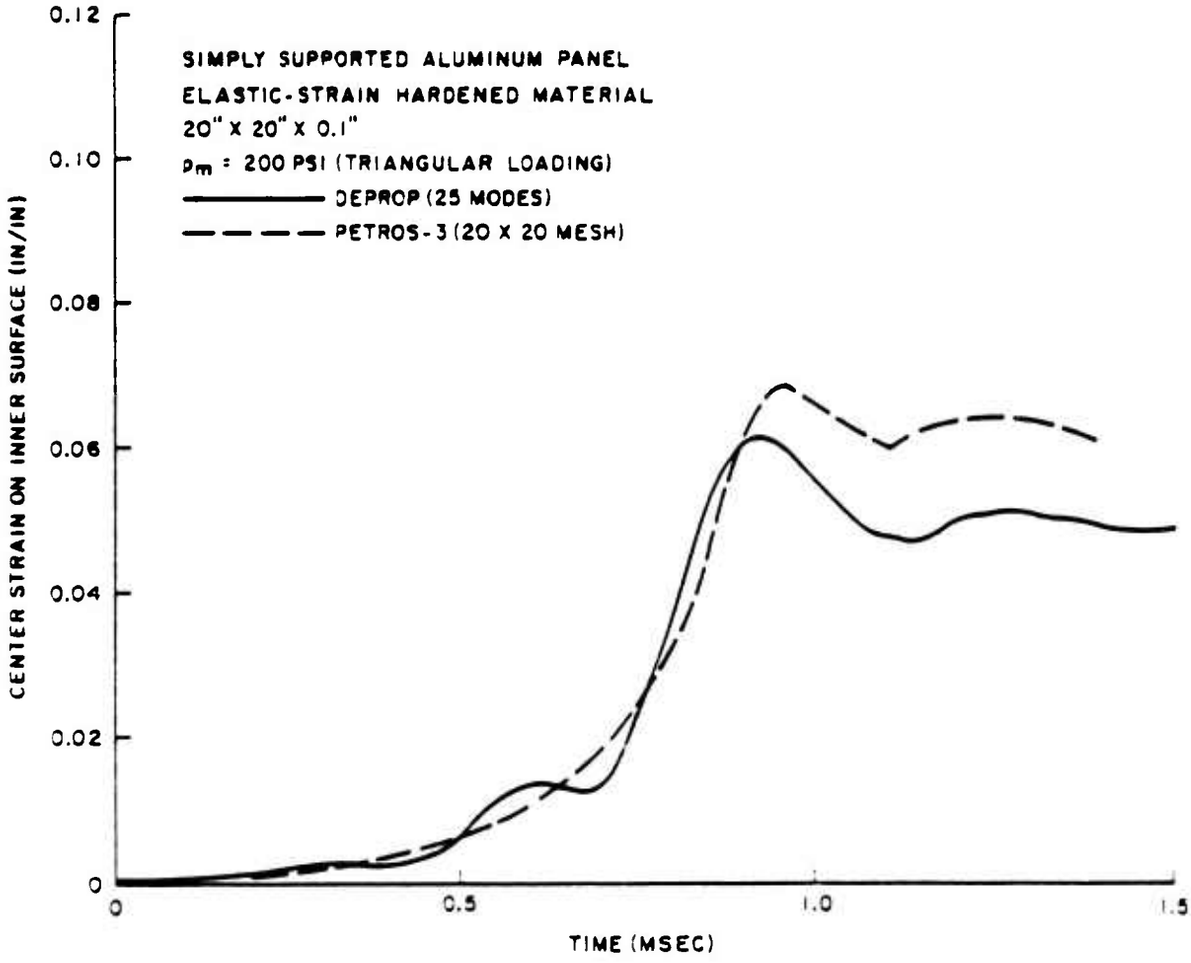

Figure 51. Comparison of DEPROP and PETROS-3 Inner Strain Response for Simply Supported Panel with Elastic-Strain Hardened Material

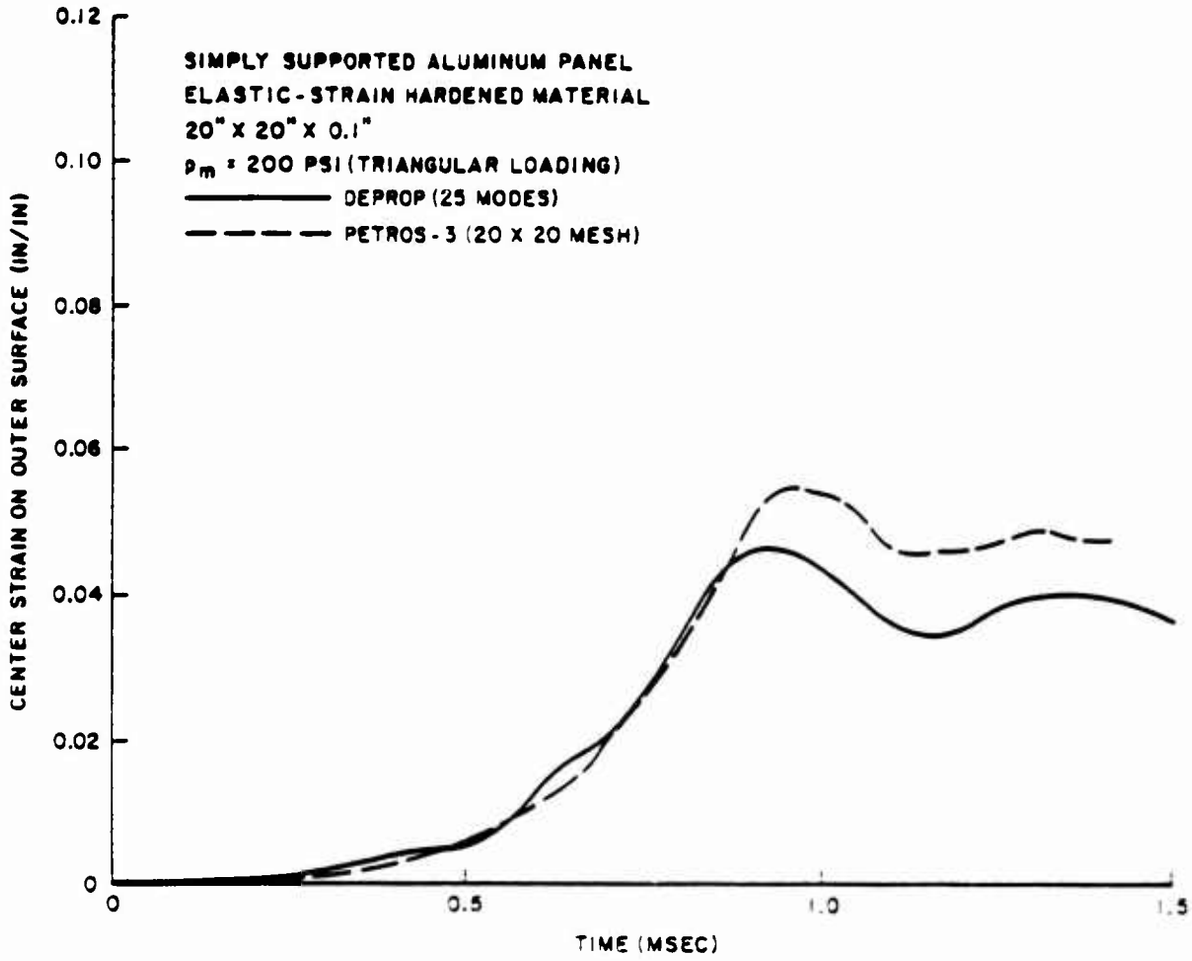

Figure 52. Comparison of DEPROP and PETROS-3 Outer Strain Response for Simply Supported Panel with Elastic-Strain Hardened Material

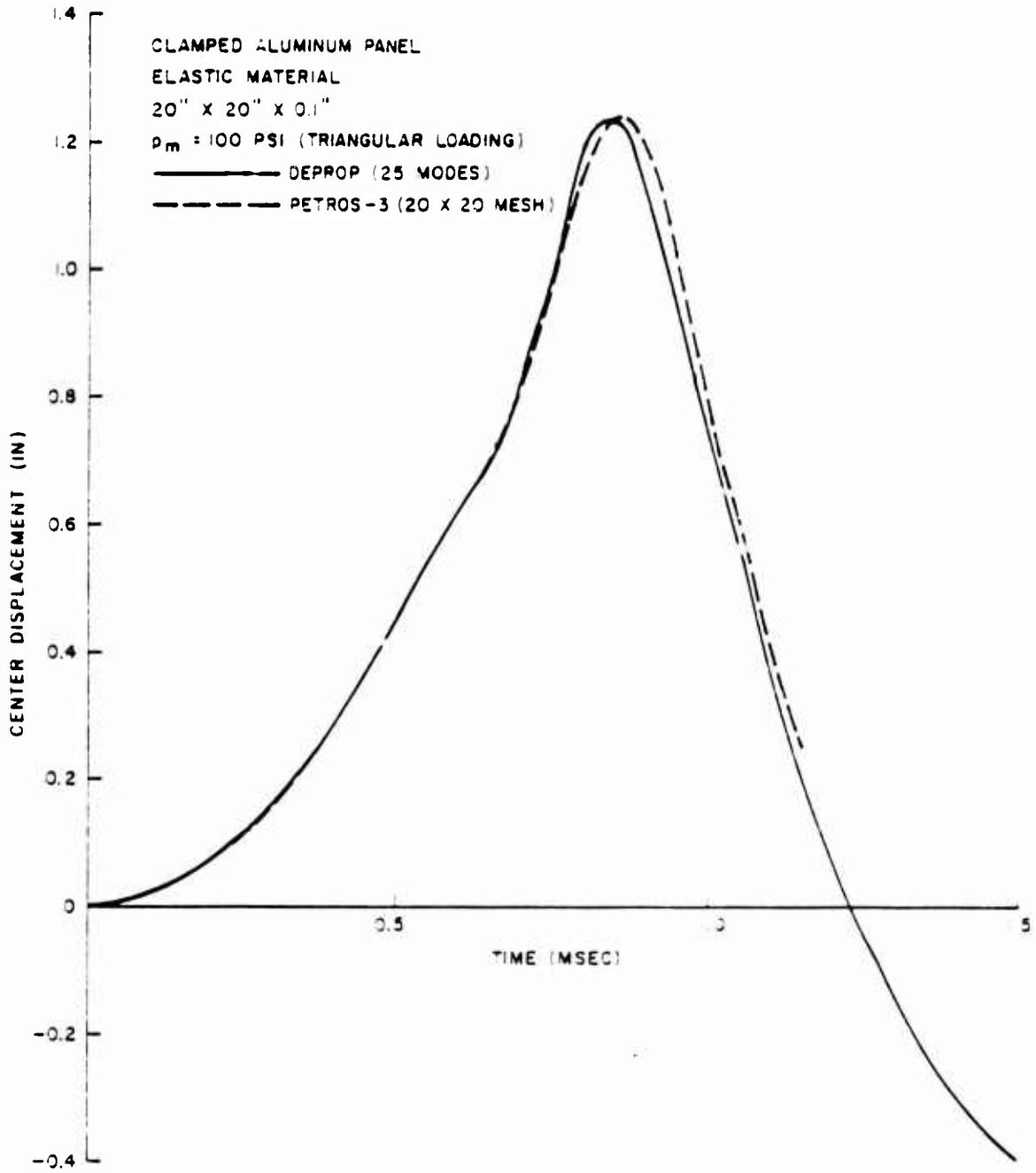

Figure 53. Comparison of DEPROP and PETROS-3 Displacement Response for a Clamped Elastic Panel

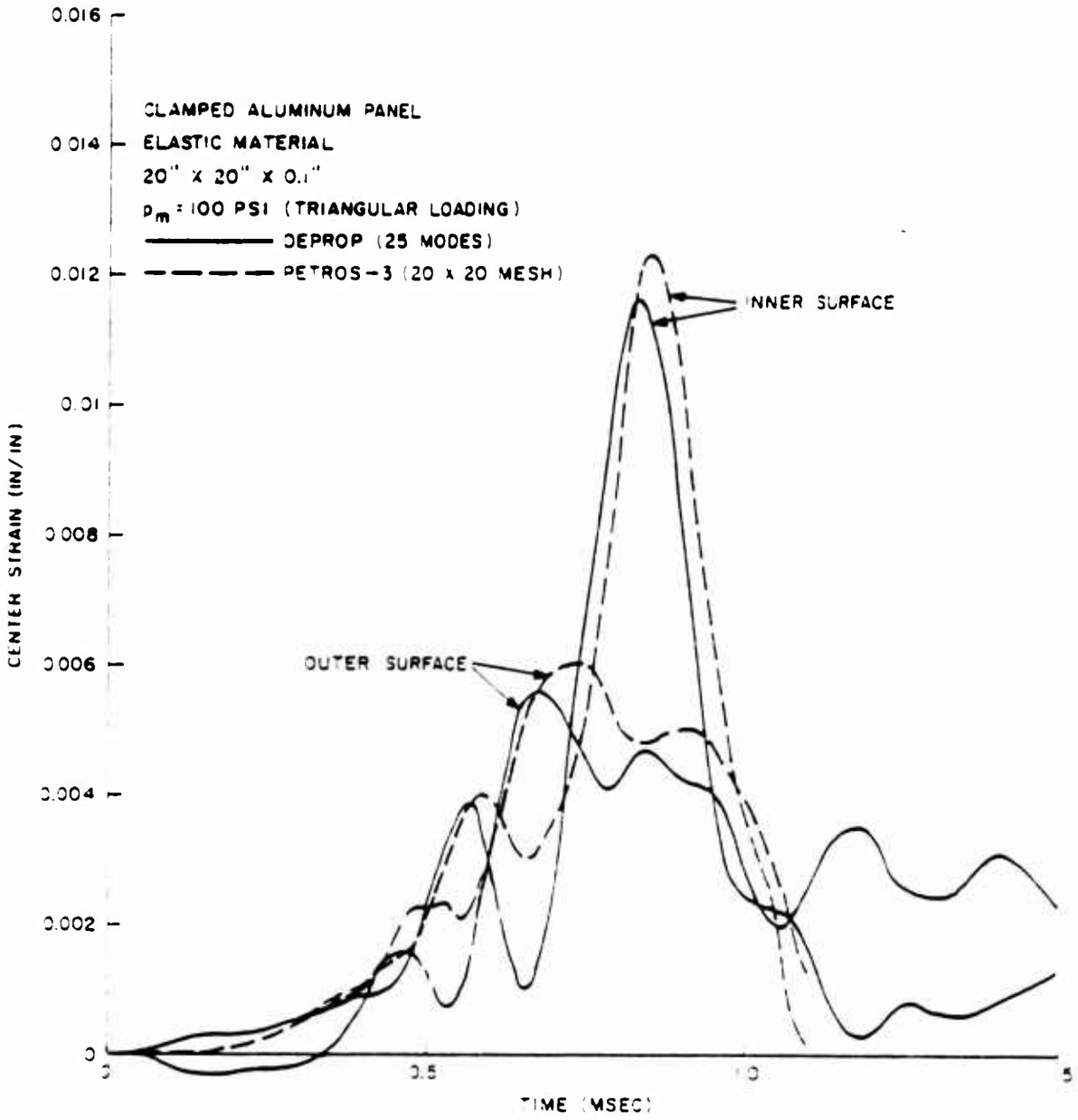

Figure 54. Comparison of DEPROP and PETROS-3 Strain Response for a Clamped Elastic Panel

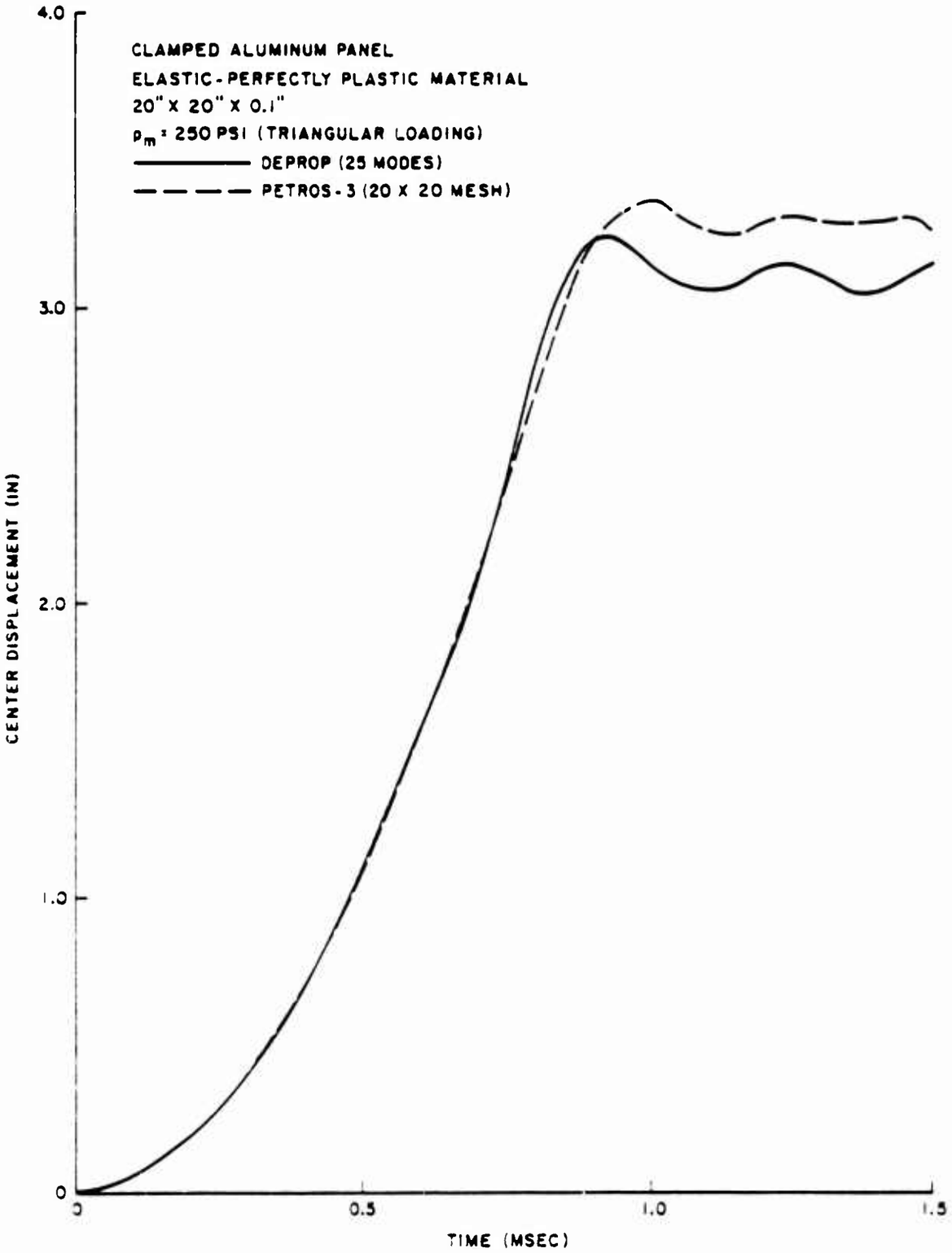

Figure 55. Comparison of DEPROP and PETROS-3 Displacement Response for a Clamped Panel with Elastic-Perfectly Plastic Material

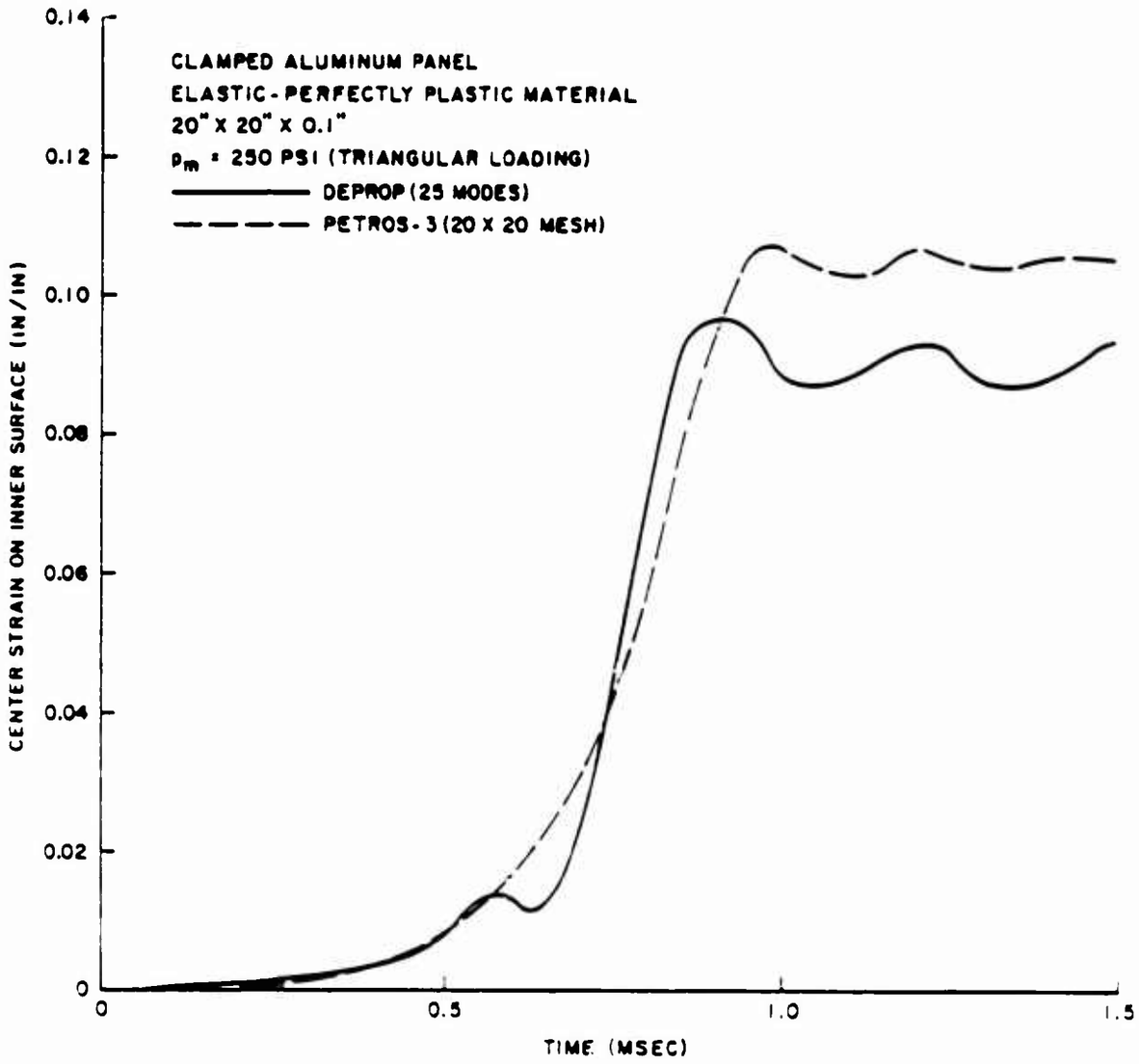

Figure 5o. Comparison of DEPROP and PETROS-3 Inner Strain Response for a Clamped Panel with Elastic-Perfectly Plastic Material

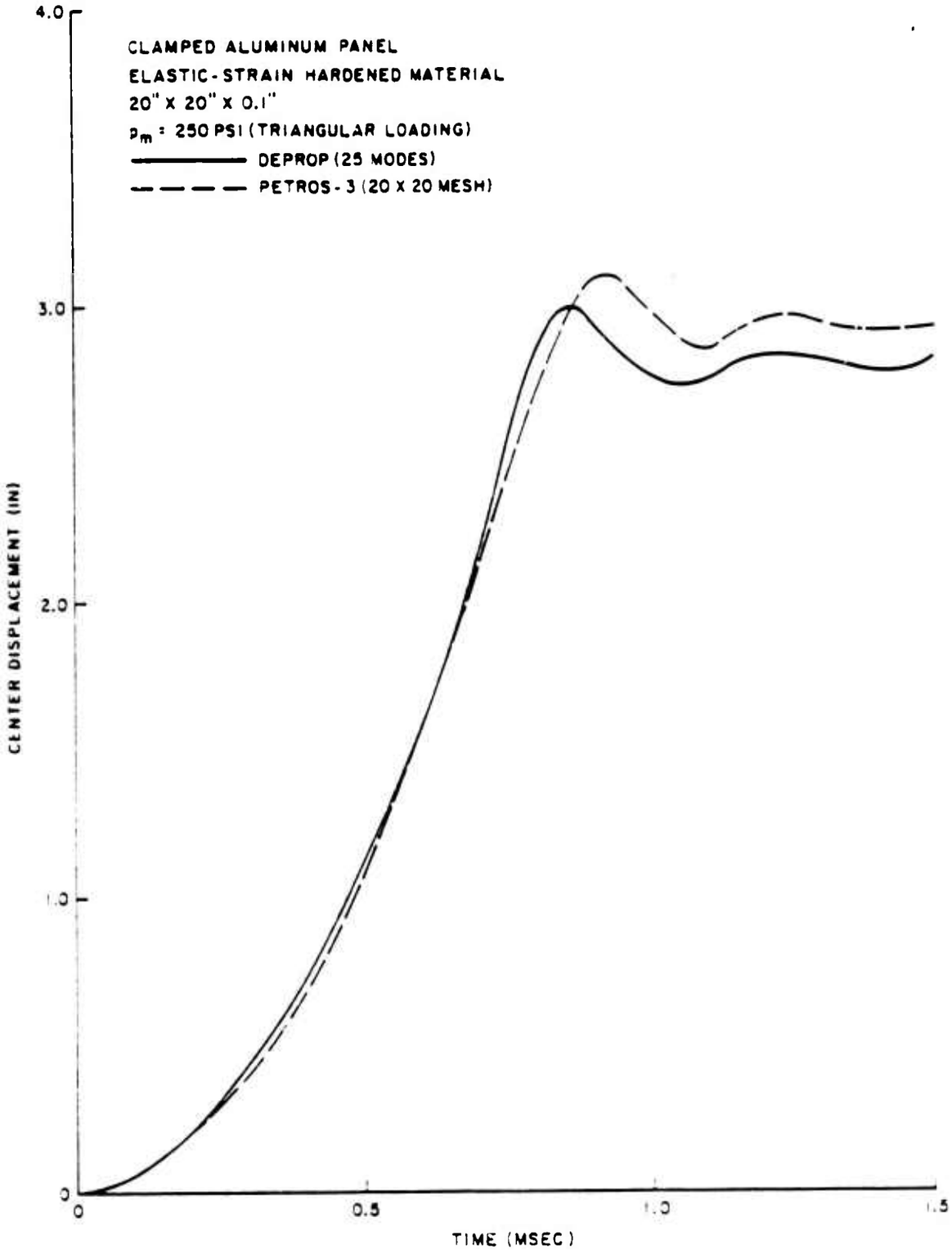

Figure 57. Comparison of DEPROP and PETROS-3 Displacement Response for a Clamped Panel with Elastic-Strain Hardened Material

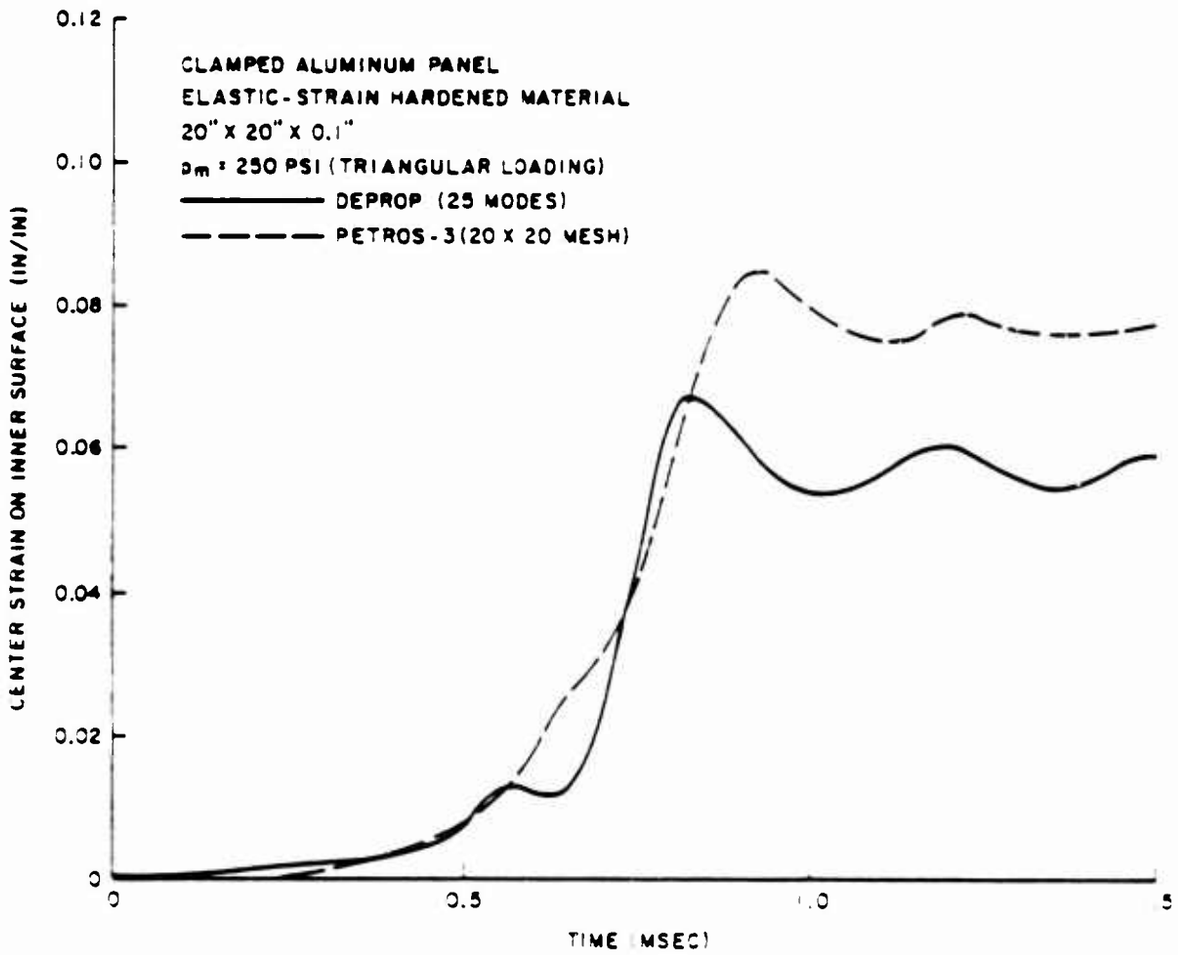

Figure 58. Comparison of DEPROP and PETROS-3 Inner Strain Response for a Clamped Panel with Elastic-Strain Hardened Material

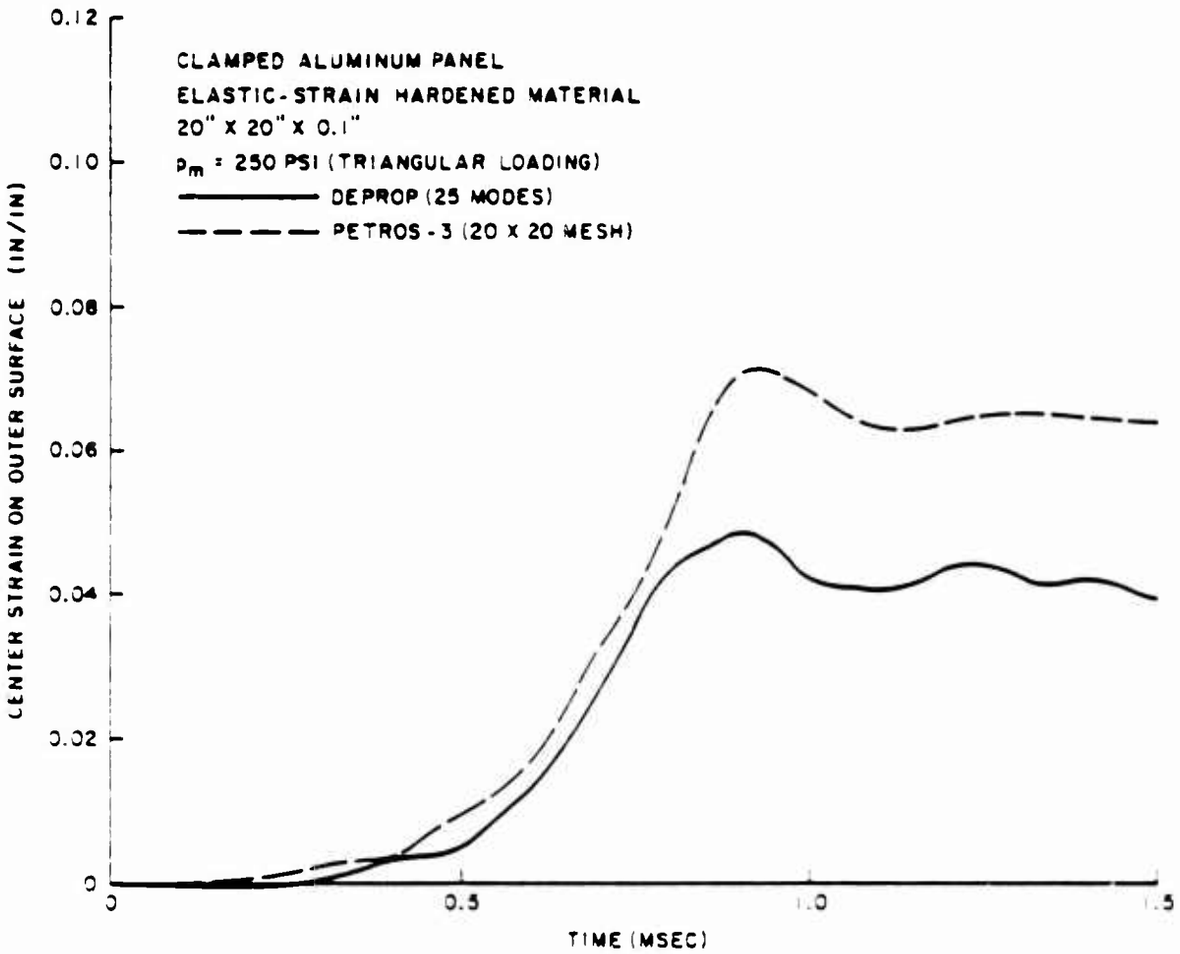

Figure 59. Comparison of DEPROP and PETROS-3 Outer Strain Response for a Clamped Panel with Elastic-Strain Hardened Material

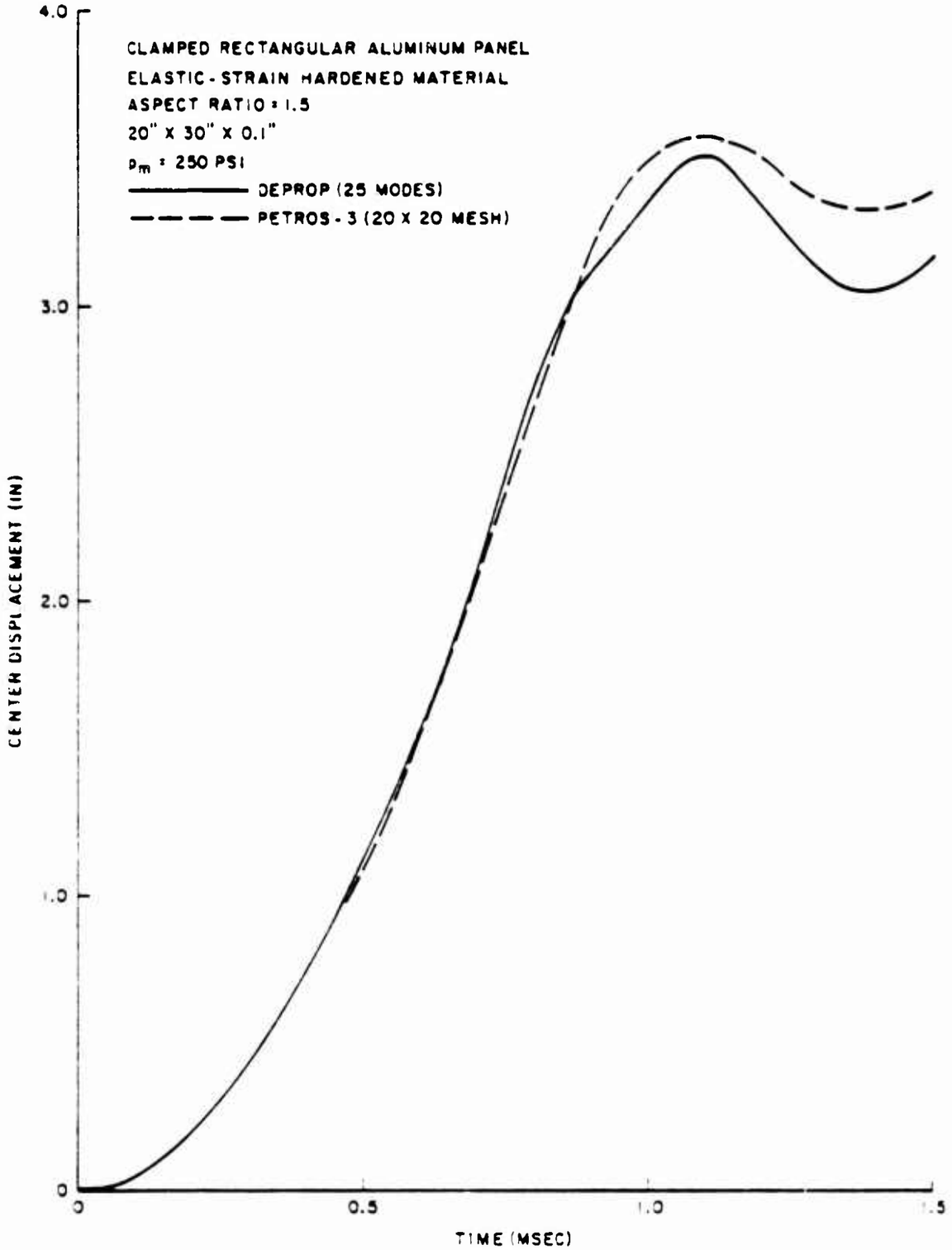

Figure 50. Comparison of DEPROP and PETROS-3 Displacement Response for a Clamped Rectangular Panel

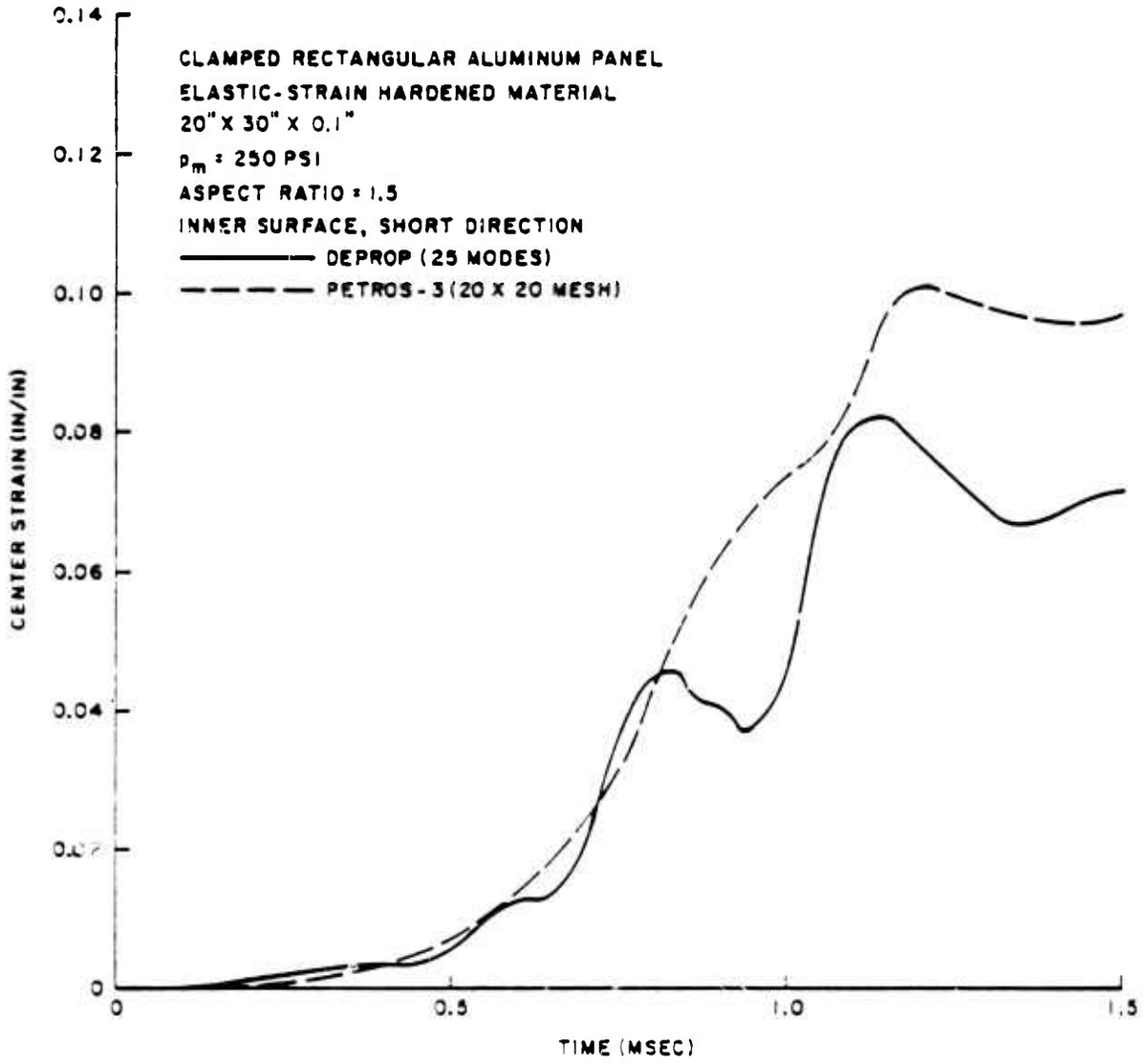

Figure 51. Comparison of DEPROP and PETROS-3 Strain Response for a Clamped Rectangular Panel

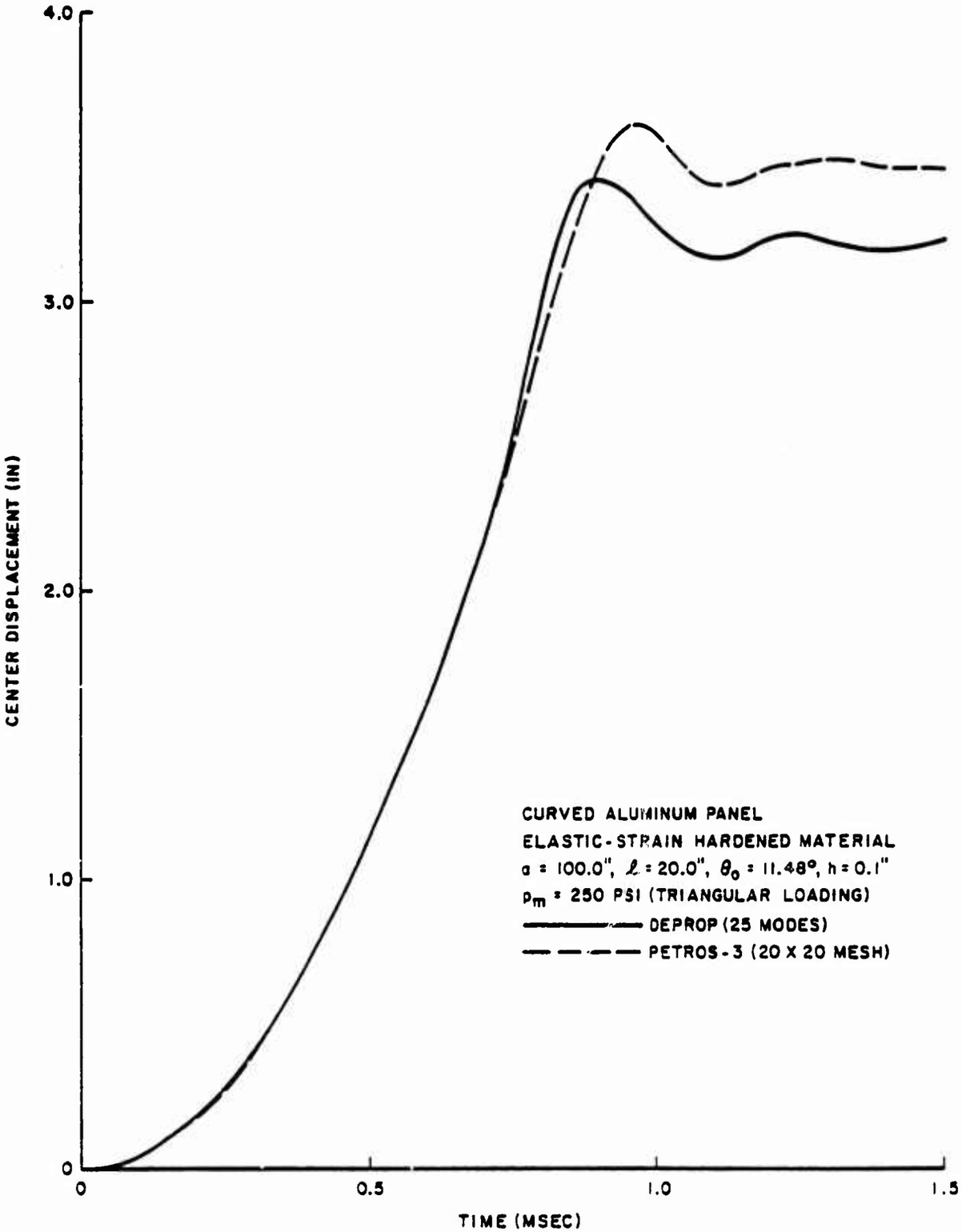

Figure 62. Comparison of DEDROP and PETROS-3 Displacement Response for a Clamped Curved Panel

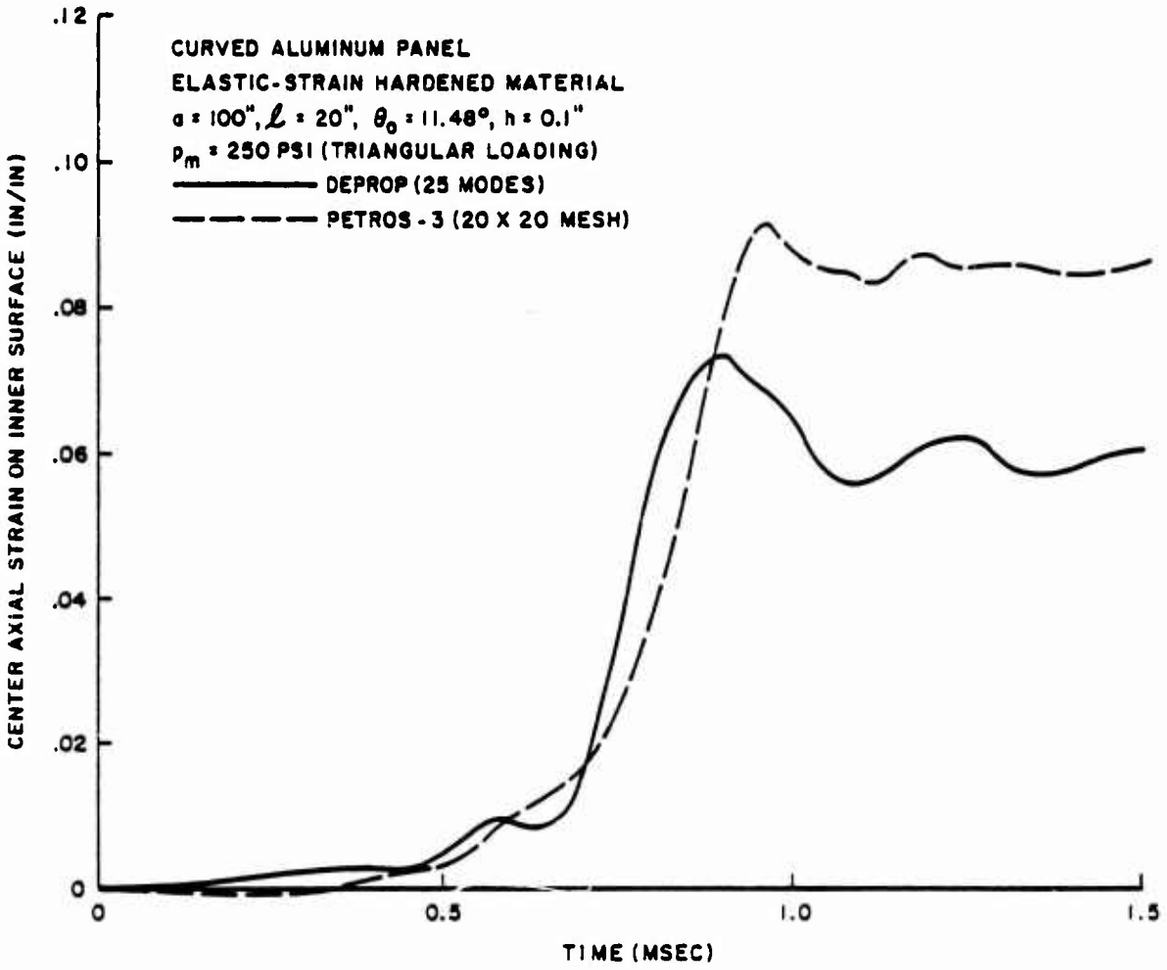

Figure 63. Comparison of DEPROP and PETROS-3 Axial Strain Response for a Clamped Curved Panel.

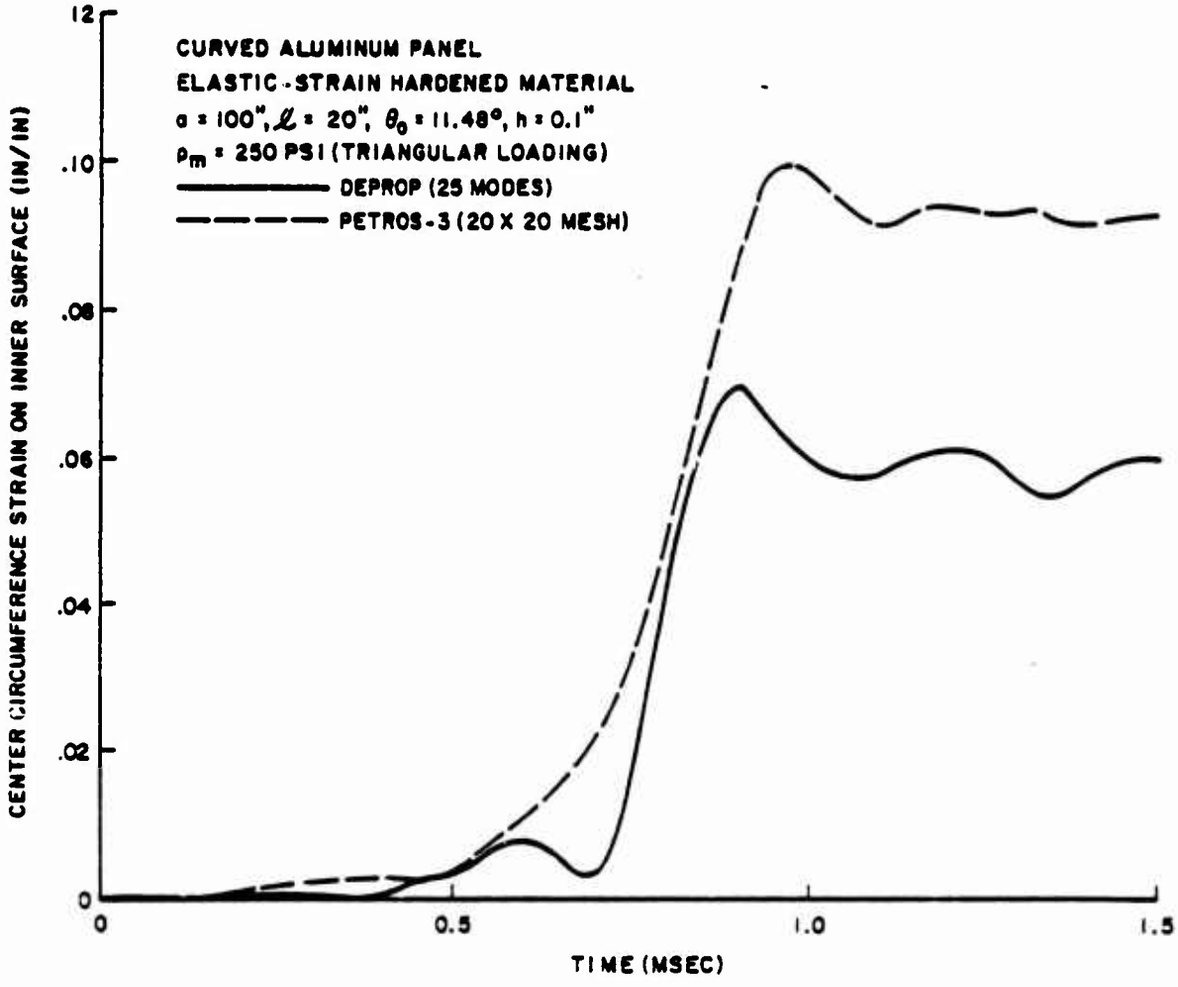

Figure 64. Comparison of DEPROP and PETROS-3 Circumferential Strain Response for a Clamped Curved Panel

and strain response in the simply supported and perfectly plastic plate (figures 47-49); but as the clamped edges, strain hardening or curved geometry are introduced, the differences in strain magnitude increase, generally varying between about 5 and 25%.

3. The general behavior of the DEPROP and PETROS-3 response solutions is the same throughout the panels, the primary differences are characterized by larger peak magnitudes and times of peak response being predicted by PETROS-3 for both displacement and strain responses. The largest differences seem to be associated with the clamped boundary conditions. Near the end of this investigation, PETROS-3.5 (ref. 46) became available. PETROS-3.5 is a revised version of PETROS-3 that has improved the finite-difference representation near the boundaries and the numerical scheme used in the incremental plasticity model. The elastic-plastic solution for the square clamped panel was obtained using PETROS-3.5 and compared with the PETROS-3 results. It was found that differences in the central displacement and strain responses were less than 2% between the PETROS-3 and 3.5 solutions for the selected panel.

4. At early times during the response, the DEPROP center strain response exhibits some oscillations not produced in the PETROS-3 strain response. In the PETROS-3 solution at early times, the central position of the plate remains absolutely flat, exhibiting just membrane strains in this region of the plates. However, based on the modal-type solution in DEPROP, this central portion of the

plate is only nearly flat and exhibits bending strains as well as membrane strains in this region which account for the oscillations in the strain plots at early times.

5. It was found that the convergence of the strain response in the PETROS-3 calculation is much more sensitive to increases in time increment and mesh size than the DEPROP calculation is to increases in time increment and decreases in the number of modes used.

6. Because of the larger strain gradient near the clamped edges of the severely deformed panels, it is felt that neither DEPROP nor PETROS-3 accurately predicts the strains at a clamped edge with the modes and finite-difference mesh, respectively, used herein. To assess the degree of accuracy of analytical predictions, experimental strain data are needed near the clamped edges or selected panels loaded with a well defined pressure time history.

7. Although neither code's solution parameters, such as modes and mesh size, should be considered as optimal for the computation of converged center strains, it was found that PETROS-3 required a smaller time increment than DEPROP for a nearly convergent center strain solution. For these panels using the aforementioned solution parameters, DEPROP solutions used about half the central processor computer time used by PETROS-3 solutions.

SECTION V
DAMAGE CRITERIA

The computer program contains the option of selecting two levels of damage to the structural elements being analyzed. One level corresponds to no permanent damage and the other level corresponds to catastrophic damage. However, the analyst must interpret the effect that the damaged panel or structural element has on the performance or mission of the aircraft. The analyst also has the option of specifying the probability that the damage level selected will be exceeded. For example, the analyst might specify the no-damage level and a probability of 5 percent that the no-damage level will be exceeded; that is, that damage will occur. The method of establishing the probability that a specific level of damage will be exceeded will now be described.

Designate the structural response parameter (stress or strain) by R and the value of R at which the specified damage level occurs by R_d. The preblast value of the parameter will be designated by R_o and the maximum value calculated by the program with respect to time by R_p. The value of R_p will be defined such that the probability of exceeding R_d will be the specified value, m. This is accomplished by estimating the accuracy of the prediction and then assuming that the probability density distribution of the response is normal. The assumption of a normal distribution is based upon the central-limit theorem, which states that the sum of independent variates from the same or different distributions is normally distributed in the limit and that this limit is approached very rapidly (see ref. 47). The large number of variables which influence the response of the structure justifies the assumption of a normal distribution.

Assuming that the analysis is unbiased, R_p is the mean of the normal distribution illustrated in figure 65. The shaded area represents the probability that the specified damage level R_d will be exceeded by m percent. It is assumed that the inaccuracy in R_p can be defined by a factor X, such that three standard deviations in response will be equal to XR_p; that is,

$$3\sigma = XR_p \tag{138}$$

The choice of three standard deviations is arbitrary. The problem of defining X so that it corresponds to the number of standard deviations chosen will be treated later.

The number of standard deviations, n, associated with the probability, m, can be determined from normal probability distribution tables. For example, if m is 5 percent, the associated value of n is 1.645. Assembling all of the above assumptions and observations, the value of R_p sought, which we will denote by $\bar{R}_p$, can be written as

$$\bar{R}_p = R_d - n\sigma \tag{139}$$

or, introducing equation 138 with the response, R_p, replaced by the desired response, $\bar{R}_p$,

$$\bar{R}_p = R_d - n \frac{X}{3} \bar{R}_p \tag{140}$$

Solving equation 140 for $\bar{R}_p$,

$$\bar{R}_p = \frac{R_d}{1 + \xi} \tag{141}$$

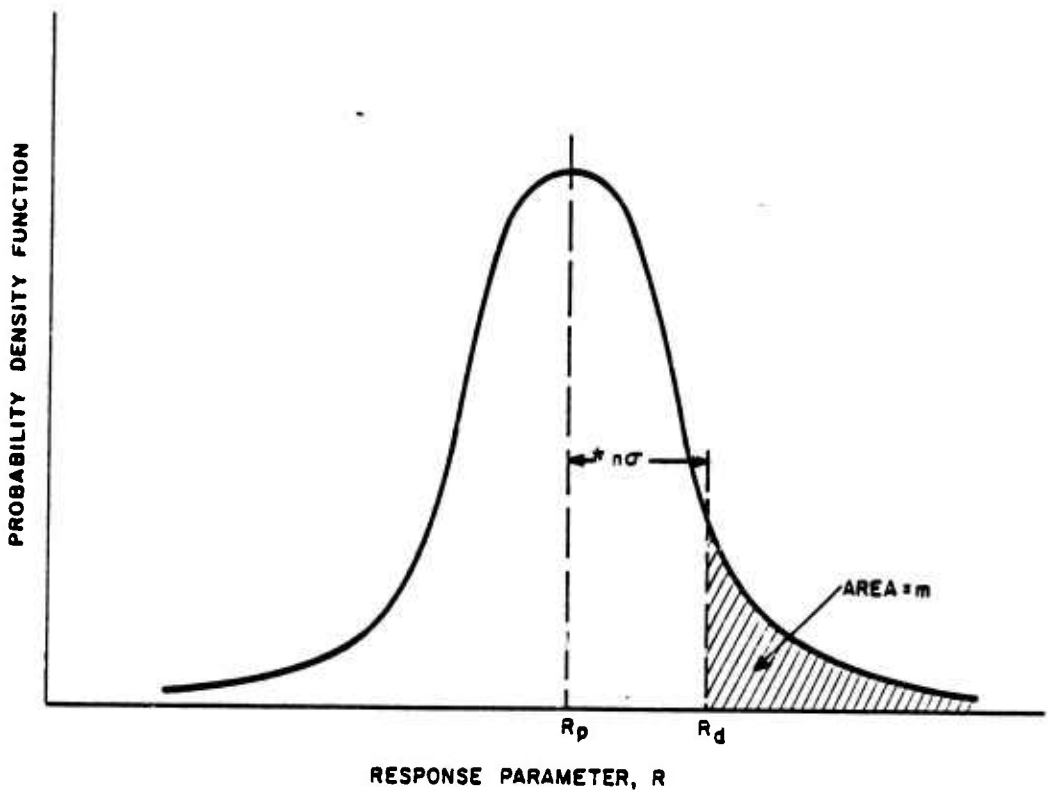

*Provided that $R_p = \bar{R}_p$

Figure 65 - Normal Probability Density Distribution of Response Parameter, R

where

$$\xi \equiv \frac{nX}{3} \tag{142}$$

The remaining problem in the implementation of the above equations is the determination of the structural response, R_d, associated with the level of damage specified, and the determination of the inaccuracy factor, X.

5.1 DETERMINATION OF DAMAGE PARAMETER, R_d

The program contains the option of selecting two damage levels, no-damage and catastrophic damage. The no-damage response level is interpreted as that level of structural response which represents the threshold of damage. The severe or catastrophic level of damage is interpreted as that level of response at which the material ruptures or fractures.

When the damage level and the percent probability that the level will be exceeded are specified, the program can be used to determine the range at which the desired response will occur with the desired probability. The process is iterative; a trial range is specified, and the response is determined and compared to a criterion. The range is adjusted within the program and the process is repeated until the ratio of maximum stress (R_p) to the critical stress ($\bar{R}_p$) converges to unity.

For no-damage response, the program uses the largest value of the ratio of maximum stress (R_p) to the critical stress ($\bar{R}_p$). In order to permit an orderly iteration process, values of the ratio ($R_p/\bar{R}_p$) greater than unity must be allowed. In addition, the critical stress may be greater than the yield stress, depending upon the selected value of probability, m. Actually, the material yields and, presumably, the structure follows a different branch of the stress-strain curve; hence, an artificial means must be incorporated within the program to permit

higher stresses than the yield stress along the elastic curve. This is accomplished by disregarding yielding and using the extended elastic stress-strain curve for the no-damage condition. This artifice permits a continuous variation of the response with range, which is necessary in order to achieve a systematic iteration process.

The process is similar for catastrophic damage. For plastic materials or for buckling analyses, the process is identical, except that larger stresses are considered critical. Otherwise, the elastic-plastic stress-strain curve must be made to accommodate strains exceeding the fracture level. In DEPROP, the stress-strain curve is extended beyond ultimate strain with the same strain hardening slope, while in DEPROB a perfectly plastic extension of the stress-strain curve is assumed. Both of these artificial extensions permit the calculation of response strains beyond the ultimate strain and therefore allows a smooth iteration process for all selected values of probability, m.

The type of structure being analyzed determines the level of stress or deformation associated with the threshold of damage or catastrophic damage. Both levels of damage are discussed for single-layered and multi-layered honeycomb panels and for stiffeners, frames, radomes, and ribs.

5.1.1 Single-Layered Panels

The DEPROP program is used to determine the stresses and strains induced in single-layered panels by steady-state and transient pressure loads. These stress and strain quantities are related to conditions in the material that can produce permanent deformations or rupture of a panel. Yielding of the material is taken as the limiting condition for threshold of permanent damage for metal panels. Since the panel deformations are biaxial, the yield stress is compared with the equivalent stress $\bar{\sigma}$ associated with the Mises-Hencky yield criterion (equation 109). This yield criterion states that plastic flow will occur when the equivalent stress $\bar{\sigma}$ reaches a value equal to the uniaxial

yield stress. For plastic or reinforced plastic materials which are assumed to be loaded elastically to an ultimate stress or strain and therefore attain a fracture condition without actually yielding, 70 percent of the tensile ultimate stress and 100 percent of the compressive ultimate stress are taken as the critical stresses which define the limiting condition for threshold of permanent damage. It should be noted that curved panels could undergo elastic buckling prior to material yielding, but this phenomenon is not considered critical since after the load is removed the panel returns to its original undeformed condition.

For catastrophic damage of single-layered metal panels, large inelastic deformations are produced during the response that lead to rupture of the material. An approximate rupture criterion is established which compares the uniaxial rupture fracture strain of the material with the effective strain $\bar{\varepsilon}$ (equation 112) using checks to insure that a tensile strain condition is present. For catastrophic damage of plastic and reinforced plastic panels, the criterion is based on the ultimate tensile stress of the material and is compared with the principal tensile stresses in the panel. For brittle materials, it is assumed that fracture occurs at the ultimate tensile stress.

5.1.2 Honeycomb Panels

The multilayer panel option of the DEPROP program is used to determine elastic stresses and strains induced in honeycomb panels due to pressure loads. The honeycomb panel is a three-layered panel with either isotropic or orthotropic material properties.

The yield stress in the face sheet is used as one criterion or limiting condition for metal face sheets when establishing the threshold of permanent damage for honeycomb panels. For reinforced plastic face sheets, 70 percent of tensile ultimate stress and 100 percent of compressive ultimate stress are used for the threshold of permanent damage. Other criteria for honeycomb panels are often required

since the panels can experience local instabilities such as intracell buckling or face sheet wrinkling. The intracell buckling occurs mainly for honeycomb panels with thin face sheets, and face sheet wrinkling occurs mainly for low-density cores and weak bonding systems. If these instabilities are severe enough to result in permanent deformations in the panel, they are acceptable as a limiting condition for threshold of permanent damage. Formulas are given in reference 48 which relate intracell buckling or wrinkling to the geometric and material properties of the honeycomb panel as follows. For intracell buckling,

$$\sigma_{cr} = 3E_f \left(\frac{f}{d}\right)^2 \tag{143}$$

where

σ_{cr} = critical stress in the face sheet, psi

f = face sheet thickness, inches

d = core cell size, inches

E_f = elastic modulus of the face sheet, psi

For wrinkling,

$$\sigma_{cr} = 0.5 \ (G_c E_c E_f)^{1/3} \tag{144}$$

where

σ_{cr} = critical stress in the face sheet, psi

G_c = core shear modulus, psi

E_c = core modulus of elasticity parallel to the core depth, psi

E_f = modulus of elasticity of the face sheet, psi

As indicated earlier, the elastic-plastic option of DEPROP is limited to single-layered isotropic panels. Consequently, in determining catastrophic damage of honeycomb metal panels, an "equivalent" single-layered panel is developed in subsection 4.2.8 to represent the deformation response of the original honeycomb in the elastic and inelastic ranges. Catastrophic damage for a honeycomb metal panel is based on the rupture strain of the face sheet material.

5.1.3 Stiffeners and Frames

The DEPROB routine can be used to calculate the response of stiffeners and frames combined with local effective skin due to a pressure loading. The dynamic response includes deflections and accelerations of the structural element plus stress throughout the cross section, particularly stress in the outer fibers of the cross section. The stresses of the outer fibers apply to either the flange plus the effective skin attached to the flange or to the outstanding leg of the element. In general, either can be loaded in tension or compression. To determine the threshold of permanent damage, the stresses in the outer fibers are compared to the yield stress for tensile or compressive loads. The magnitude of the moment at the fixed ends of a uniform beam carrying a uniform static load is twice that of the moment at the center of the beam. Consequently, the threshold of permanent damage will be achieved primarily by buckling of the outstanding leg at the end of the beam for this case, rather than yielding in tension or compression at any point along the beam. Crippling stress formulas are available for local buckling of outstanding legs of different shaped stringer or frame elements. The crippling stress formula used in the program is identical to that used in reference 49, page C1.2-36:

$$f_{cc} = KE\left(\frac{t_f}{w}\right)^2 \qquad (145)$$

where

f_{cc} - crippling stress for the outstanding leg, psi

K - buckling coefficient equal to 1.25 if the outstanding leg has only one corner, and equal to 3.62 if the outstanding leg has two corners

E - modulus of elasticity, psi

t_f - thickness of the outstanding leg, inches

w - width of the outstanding leg, inches

For nonuniform beam elements, t_f and w at the center of the beam are used as representative values.

Local buckling or crippling is a minor type of failure compared with reaching ultimate strain or rupture of some portion of the cross section. Consequently, catastrophic damage for stiffeners and frames is based on tensile rupture strain in the outer fibers.

And for clamped beam elements subjected to catastrophic damage, DEPROB computes a very localized ideal edge strain which can far exceed usual handbook rupture strain levels prior to actual rupture. Therefore, a strain equal to one-third that computed at the edge is compared with rupture strain levels for catastrophic damage.

5.1.4 Radomes and Other Shells

Radomes on various aircraft have different shapes. Some radomes are best analyzed by the DEPROP program where a curved panel representation is reasonable. Other radomes, such as the nose and tail radomes of the B1, are conical or near-cylindrical shells. For these shapes, a two-dimensional ring representation is reasonable and the DEPROB program should be used. Since reinforced plastic material which fractures at ultimate strain is used in radomes, 70 percent of tensile ultimate stress and 100 percent compressive ultimate stress are used for the threshold of permanent damage, and ultimate tensile strain is used for catastrophic damage.

DEPROB can also be used to analyze a metal shell in an approximate way when modeled as a free ring. In this case the threshold of damage criterion is based on tensile and compressive yield stresses, compared to stresses in the outer fibers. Catastrophic damage is based on tensile strain in the outer fibers exceeding rupture strain.

5.1.5 Rib Webs and Stiffeners

Failure in vertical metal rib elements is assumed to occur in a buckling mode. Modeled as an axially loaded beam with fixed ends (except that motion is permitted in the axial direction), threshold of permanent damage and catastrophic damage are both related to the occurrence of column buckling. It should be noted that as a material begins to yield, it quickly loses its resistance to buckling. Although the two events are clearly separate phenomena, experience indicates that if for increasing levels of load the beam has not buckled by the time it begins to yield, it will with very little additional load.

Catastrophic damage, then, is defined as the point at which the tensile strain in the outer fibers exceeds the tensile ultimate strain, which will usually closely follow the attainment of tensile yield strains. Threshold of permanent damage is defined as a maximum tensile or compressive strain equal to 70% of yield strain.

For situations in which the rib collapses, the numerical procedures employed may not be able to keep up with the process. In such cases, the program assigns a negative number to the maximum response and proceeds to select a larger range.

5.1.6 Damage Criteria Summary

In summary, damage criteria for panels, stiffeners, frames, radomes, and ribs are given in table 13 for threshold of permanent damage, TPD, and catastrophic damage, CD. In general, all spatial locations on the structural elements are checked in the timewise solution in order to accumulate the maximum response parameters. While DEPROB checks the parameters every time step, DEPROP checks only every tenth step-a procedure which conserves computer time in the slower running DEPROP without significant loss of accuracy.

TABLE 13

CRITERIA FOR THRESHOLD OF PERMANENT DAMAGE (TPD)
AND CATASTROPHIC DAMAGE (CD)

Program - DEPROP

Structural Element - Panels

Spatial Locations Considered - All spatial integration points

Types of Panels:

1. Single-layered metal

   TPD - Compare tensile or compressive yield stress with Mises-Hencky equivalent stress at inner and outer surfaces.

   CD - Compare rupture strain with effective tensile strain at inner and outer surfaces.

2. Single-layered plastics

   TPD - Compare 70 percent of tensile and 100 percent of compressive ultimate stresses with principal tensile and compressive stresses, respectively, at the inner and outer surfaces.

   CD - Compare tensile ultimate stress with principal tensile stresses at inner and outer surfaces.

3. Honeycomb metal

   TPD - Compare tensile yield stress with Mises-Hencky equivalent stresses at centers of face sheets; compare the compressive yield stress with Mises-Hencky equivalent stress at centers of face sheets; and compare the lowest of intracell buckling stress and face sheet wrinkling stress with maximum principal compressive stresses at centers of face sheets.

TABLE 13 (Continued)

CD - Compare face sheet rupture strain with effective tensile strains at points on equivalent single-layered cross section which correspond to the center of the face sheets of original cross section.

4. Honeycomb reinforced plastics

TPD - Compare 70 percent of tensile ultimate stress with principal tensile stresses at centers of face sheets; and compare the lowest of 100 percent compressive ultimate stress, intracell buckling stress, and face sheet wrinkling stress with maximum compressive stresses at centers of face sheets.

CD - Compare ultimate tensile stress with principal tensile stresses at centers of face sheets.

5. Multilayered plastics

TPD - Compare 70 percent of tensile and 100 percent of compressive ultimate stresses with principal tensile and compressive stresses, respectively, at inner and outer surfaces of each layer.

CD - Compare ultimate tensile stress with principal tensile stresses at inner and outer surfaces of each layer.

Program - DEPROB

Structural Element - Stiffeners and Frames (beam elements)

Spatial Locations Considered - All bars of beam

TPD - More critical of (a) comparison of largest tensile and compressive stresses on inner and outer fibers with tensile and compressive yield stresses, respectively; (b) comparison of largest compressive stress on outstanding leg with the crippling stress.

CD - Compare rupture strain with largest tensile strains on inner and outer fibers.

TABLE 13 (Concluded)

Structural Element - Shells (Free Ring)

Spatial Locations Considered - All Bars of Ring

Types of shells:

1. Reinforced Plastic Radomes

   TPD - Compare 70 percent of tensile and 100 percent of compressive ultimate strasses with tensile and compressive stresses, respectively, at inner and outer fibers.

   CD - Compare ultimate tensile strain with largest tensile strains on inner and outer fibers.

2. Metal

   TPD - Compare tensile and compressive yield stresses with tensile and compressive stresses, respectively, in the inner and outer fibers of each layer.

   CD - Compare rupture strain with largest tensile strains on inner and outer fibers.

Structural Element - Ribs (End Loaded, Clamped Beam Element)

Spatial Locations Considered - All Bars of Beam

TPD - Compare 70 percent of tensile and compressive yield stress with largest tensile and compressive stresses, respectively, in inner and outer fibers.

CD - Compare rupture strain with largest tensile strains on inner and outer fibers.

5.2 DETERMINATION OF INACCURACY FACTOR, X

In order to establish the probability of threshold or catastrophic damage occurring, the inaccuracy factor, X, in equation (142) must be defined. Note that the determination of X is highly subjective and is not subject to verification by analysis. Only by comparing a large group of experimentally produced responses to pressure loads from nuclear blasts under varying conditions with corresponding calculated responses could X be determined objectively.

Assuming that the environmental conditions are known exactly, the largest inaccuracies are assumed to exist in the modeling of the structure as discrete elements. Values of fractional inaccuracy, X, have been selected for the various conditions considered and related to accuracy factors which are given in table 14. These values are very subjective and represent the best estimates the authors can make based on their experience in the present and related problems. If the accuracy factor is 2, the actual response is considered to be within a factor of 2 of the predicted response. This results in different values of X (and hence standard deviations) for responses greater than $\bar{R}_p(X^+)$ and less than $\bar{R}_p(X^-)$ (figure 65). These values of X are related to ACC by

$$X^+ = ACC - 1 \tag{146}$$

$$X^- = 1 - \frac{1}{ACC} \tag{147}$$

In terms of probability, if the probability, m, < 0.5, X^+ is used in the program to determine ξ; if $m > 0.5$, X^- is used. The accuracy factor is considered to be more meaningful than a single value of X. For example, if X were taken as one, there would be an implication that the likelihood of zero response would correspond to the likelihood of twice the predicted response. Such an implication can be rejected on purely intuitive grounds; hence, the accuracy factor, which avoids this difficulty, seems to be more logical.

TABLE 14

ACCURACY FACTORS FOR CRITICAL RESPONSES, ACC

Structural Elements	Threshold of Permanent Damage	Catastrophic Damage
Single-Layered Metal Panels	1.3	1.8
Single-Layered Plastic Panels	1.3	1.5
Honeycomb Metal Panels	1.5	2.0
Honeycomb Plastic Panels	1.5	1.7
Multilayered Plastic Panels	1.4	1.6
Stiffeners	1.3	1.7
Frames	1.5	1.8
Radomes and Other Free Rings		
Metal	1.6	1.8
Plastic	1.6	1.8
Ribs	2.0	2.0